Extended semi-analytical model of bipolar hybrid stepper motor

by

Newman Wu

to obtain the degree of Master of Science in Electrical Power Engineering
at the Delft University of Technology,
to be defended publicly on Monday August 24, 2020 at 10:00 AM.

Student number:	4795628
Project duration:	November 19, 2019 - August 19, 2020
Thesis committee:	Prof. dr. ir P. Bauer
	Dr. J. Dong
	Dr. D.J.P. Lahaye
Company Supervisor:	Dr. T. van Beek

PRODRIVE TECHNOLOGIES

TU Delft
Delft University of Technology

Acknowledgements

Throughout the writing of this thesis, I have received many supports and assistance.

I would first like to thank my university supervisor, Dr. J. Dong, whose expertise was invaluable. He convincingly guided and encouraged me to be professional and do the right things even though the road is tough.

I would also like to thank my company supervisor, Dr. T. van Beek. You provided me with the tools I needed to choose the right direction in formulating the research topic and methodology further.

In addition, I would like to thank my parents and my brother, Kenny, for emotional supports. You kept me going on and this work would not have been possible without your inputs. Finally, there are my friends, Nived, Medha, Murielle, Judy, Annie, and Kelly, who were of great support during COVID-19.

Contents

Summary

The aim of this graduation thesis *Extended semi-analytical model of bipolar hybrid stepper motor* is to present a bipolar stepper motor semi-analytical model and compare its simulated motor dynamics. Stepper motor modeling has been successfully used to simulate motor performance and dynamics, yet, each modeling method holds advantages and disadvantages toward one another. In this thesis, the analytical modeling method is implemented for its faster simulation time. A semi-analytical model is constructed with motor non-linear entities on top of the motor analytical equations.

This thesis first examines and validates a finite element analysis model to extract such non-linear entities into lookup tables. A generalized electrical model and a flux-based model are constructed separately based on the analytical equation and lookup table. In a second stage, the motor dynamics from these models are compared and adapted to the semi-analytical model motor dynamics through non-linear parameters. Two methods to obtain the non-linear parameters, with and without motor measurements, are applied. Finally, Various motors with different parameters are simulated with the semi-analytical model. Comparison, accuracy, and limitations of the semi-analytical model is discussed. At the end of the thesis, conclusions are drawn from the simulated dynamics that a semi-analytical model can indeed be implemented to better simulate the motor dynamics; however, because of the estimation and measurements needed for the non-linear parameters, the semi-analytical model holds several limitations that made it less robust than the model with pure analytical equations.

Chapter 1

Introduction

1.1 Background and Motivation

With the increasing amount of automation in the manufacturing sector, manufacturers are developing machinery capable of high-accuracy repeating motion. Such a feature plays an essential part in the fast-growing field of robotics, computer numerical control (CNC), and automated manufacturing [1]. Yet, while high accuracy is crucial, the increasing cost usually comes alongside the extra equipment, such as encoders, required for position tracking. To reduce machinery cost without negatively affecting much of its accuracy, factors such as control method and motor selection are essential toward a more viable machinery option.

Applications such as CNC milling machines and robotic arms often require repeatable accurate positioning and speed control when deployed to recurring tasks [1]. An important aspect to achieve accurate repeating motion lies in the fundamental working of a motor. Since most motors run intuitively in a continuous rotary motion, servo closed-loop control systems are usually implemented with these motors to achieve a fast and accurate stop at a rotary position [2]. Some of the continuous motion motors used are:

- Brushless DC motor (BLDC);
- Brushed DC motor;
- Synchronous AC motor (PMSM);
- Synchronous AC reluctance motor;
- Asynchronous AC Induction motor.

The synchronous AC motor is referred to as the permanent magnet synchronous motor (PMSM) since AC motor with a coil wounded rotor is seldom used in a servo setup [3]. In mid-sized CNC machines and robotic arms, PMSM and BLDC motors are often implemented due to their more suitable motion profile and motor advantages [3, 4]:

- High torque with the presence of the magnet;
- Wide speed range;
- Lower inertia due to presence of the magnet;
- Low maintenance with no commutators.

With these motion profiles and advantages, PMSM and BLDC are often used in applications that require higher torque and higher speed ranges. Yet, in other applications such as PCB component placement, or laser CNC, where torque is considerably less, BLDC and PMSM are often not the best fits for such applications. Additionally, positioning and operating BLDC and PMSM motors come with a higher price because of the motor magnet and more complex torque speed control method; not to mention the equipment, such as encoder, required to control motors accurately in closed-loop [5].

A specific motor type, the stepper motor, has gained increasing popularity in the automatized world. Applications such as low load CNC machines, PCB component placement machines, and 3D printing have quickly adapted to it [6]. The unique property of the stepper motor enables the repeatable positioning of these applications. The stepper motor is a step-wise increase synchronous motor. With the ability to directly translate the switched excitation pulses to incremental rotor positions, stepper motors are widely applied to applications where precise position control is required [7]. Pulse sequences created by a micro-controller is connected to the phase inputs of the motor. Relative phase flux is formed to create the rotational speed and torque. Steps are stopped at relative positions by pausing the pulses [8]. The flux is created by both the coils and either the magnet on the permanent magnet stepper motor or reluctance on the variable reluctance stepper motor.

It is possible to run stepper motors in both open and closed-loop control. Open-loop control enables a simple implementation without extra components such as the encoder. This is possible from the direct translation of pulse to step on a stepper motor [7]. However, with such a simple setup, the connected load has to be strictly limited to the maximum load torque [8]. Closed-loop control enables a more accurate and robust motion by enabling a feedback control from an encoder [7]. However, with more components required, it also more expensive to implement a closed-loop stepper motor system.

Unlike BLDC and PMSM, stepper motor enables a direct open-loop control without feedback, which reduces the cost because of the fewer components required for position feedback control [4]. However, because of the open-loop control, stepper motors also carry some shortcomings. The disadvantages can be summarized as follows [4,9]:

- Larger heat production with high power consumed at low speed;

- Oscillation caused by the discrete rotor motion;

- Pull-in/ out torque dynamics caused by the motor inertia and resonance;

- Often requires prior knowledge in the application such as working environment and load rating.

In this thesis, modeling analysis is presented for generic bipolar hybrid stepper motors in open-loop control. This allows dynamic performance characteristics to be taken into account in the design of motion platforms, such as small-scaled CNC machines, without requiring closed-loop position control under load. Since the stepper motor requires fast acceleration and deceleration, accurate motor dynamics have to be known for the application. Pull-in/ out dynamics and step responses have to be taken into account. Open-loop models need to be investigated to more accurately represent the dynamic performance of a stepper motor system.

1.2 Problem Statement and Scope of Thesis

Different motor modeling methods had been developed to predict the stepper motor performance. These modeling methods are depicted by their iterative, discrete, or continuous solving processes. Each consists of simulation advantages and disadvantages.

The analytical modeling method builds on electrical circuit phenomenons and fundamental energy conservation. The phenomenons are simplified analytically to equate motor electrical input to the mechanical output with the losses calculated in between [10]. Such a modeling method consists of assumptions that simplify the electrical equations. These assumptions are given by idealizing the physical electric and magnetic motor circuit. Details such as higher harmonics and magnetic saturation are not included [8]. Furthermore, the output mechanical parameters are to be calculated by the energy and co-energy produced by the electric circuit [8]. The analytical modeling method is used to obtain the motor dynamics from manufacturer parameters [10]. The advantage of such a modeling method is that, while the analytical equations are based on derivatives and integration of the Ohm's law and Lenz's law, without the need of physical motor dimensions, it can be solved the fastest. With the model computation time directly proportional to the discrete sampling rate, computation time can be greatly reduced from lowering the sampling rate.

The magnetic equivalent circuit (MEC) modeling method, on the other hand, analyzes the motor with magnetic equivalent circuits. By solving the magnetic equivalent circuit, or reluctance network, such a modeling method intuitively includes the magnetic phenomenons for the physical material and structure of the model. The MEC represents the motor dynamics by properly representing the magnetic field

curves within the structure, which is often linearized in the analytical modeling method [11]. With the magnetic equations dependent on the physical motor material dimensions, the MEC solves magnetic equations directly without non-linear material and iteratively with non-linear material. This is because [12]. Trapezoidal reluctance blocks are deployed to represent a motor with each reluctance block representing one fundamental reluctance circuit at a certain position and material of the motor. Combining the blocks, a network of the to-be-solved magnetic circuit is built [13]. By solving the reluctance network, the motor dynamics can be obtained. This method can represent the non-linear magnetic phenomenons more accurately [14]. However, with the iterative nature to solve a MEC, the number of reluctance blocks to be solved will affect the computation time. Nonetheless, the 3D equivalent magnetic circuit network method (3D EMCNM) proposed in [12] would require a numerical solver to deploy the reluctance block 3D model.

The finite element analysis (FEA) modeling method is built on the numerical partial differential equations of magnetism. The motor force are obtained with the Maxwell stress tensor. With the help of computer computation, it solves the Maxwell equations iteratively in a motor 3D structure. The magnetic dynamic is calculated by applying partial differential equations on discretized meshed space dimensions [15]. Different yet similar to both the analytical modeling method and MEC, the FEA solves the Maxwell equations that are also derived in the general electric model. However, it solves the equations that are deployed in all the small mesh elements in a 3D motor model. Theoretically, the higher number of mesh elements the finer the motor spaces are discretized, which means more details of the motor can be obtained [16]. Yet, a higher number of mesh elements also means a higher number of equations to be iterate through and solve, consequently, longer computation time. Therefore, more than often, FEA requires fine-tuning between the number of mesh elements and model accuracy [16].

The analytical modeling method is often used to represent the dynamics of a stepper motor because of its equation simplicity [10]. Nonetheless, such a modeling method predicts motor performance through linearized analytical equations [10]. To obtain a model with higher precision, the numerical FEA modeling is often a better choice because of its inclusiveness on magnetic phenomenons. However, with a much longer time for each simulation caused by the amount of mesh implemented, the FEA modeling is more than often not optimal. Furthermore, without the physical motor geometries, FEA and MEC modeling methods are often not possible to be implemented correctly.

A more detailed generic semi-analytical model built on the analytical modeling method that includes motor non-linear entities is, therefore, needed. Such a method holds the speed benefit in analytical modeling and includes non-linear entities from the motor. Such a generic semi-analytical model built should be analyzed and validated.

1.3 Research Methodology

The semi-analytical model that builds on the analytical modeling method and includes the motor non-linear entities is proposed. FEA modeling method is applied to assist the understanding of magnetic flux phenomenons. To obtain the semi-analytical model and include non-linear entities from the stepper motor, the possible non-linear parameters are estimated and optimized by comparing the generalized electrical model and flux-based model shown below. The motor mechanical block proposed in the model will be decoupled in this phase to both increase the simulation time and avoid the mechanical oscillations. Nonetheless, two methods to obtain the non-linear parameters with and without physical motor measurements are implemented. The significance of motor measurements will be determined. The three models, including the semi-analytical model, are built on the analytical modeling method with varying degrees of complexity.

- Generalized electrical model:
  The generalized electrical model uses analytical equations that idealized the model to not include non-linear entities [8]. With the datasheet parameters, the generalized electrical model is used to obtain the motor dynamics. Moreover, this generalized electrical model will be the basis of the semi-analytical model.

- Flux-based model:
  The flux-based model consists of a simple motor electrical circuit. However, different from the generalized electrical model, the flux-based model does not linearize the equations. Instead, the magnetic flux linkage is directly obtained from a lookup table (LUT) extracted from the FEA

model. Such a model represents the full dynamic of the stepper motor with physical non-linear entities such as saturation. The flux-based model is to be compared to the generalized electrical model.

The FEA output data are used as LUTs for the flux-based model. The motor structure, geometry, and materials are determined and measured with a caliper, obtained through flux curve fitting, and chosen from manufacturing standards. The FEA model is built with reference to motor geometry and materials. Such an FEA representation of the physical motor will allow data to be extracted without using physical instruments. Since measurements such as flux density require high tolerance instrumentation, the FEA model will reduce the amount of complexity in the lab setup requirement. Nonetheless, dynamic entities such as magnetic flux can be extracted directly from the FEA model.

- Semi-analytical model:
  The semi-analytical model is built based on the generalized electrical model with additional non-linear parameters. These non-linear parameters are determined.

With the non-linear parameters determined, motor curves simulated from the fully connected semi-analytical model with a mechanical block are then validated with the manufacturer given curves. Various two-phase bipolar hybrid stepper motors under different motor parameters will be simulated with the semi-analytical model.

A test bench is then designed for motor dynamic measurements. Tests are proposed on the test bench to extract motor dynamics. The LCR meter and oscilloscope are used to measure the motor datasheet parameters. The measured parameters serve as the basis for the motor non-linear parameter selection. In this thesis, the pull-in/out torque curve and motor parameters are validated among manufacturing datasheet and MATLAB/Simulink models. The tests in test bench are designed to obtain such parameters.

1.4   Thesis Structure

The thesis consists of eight chapters. Chapter 1 points out the problem statement and research goals of this thesis. Chapter 2 brings a brief history and working principle of stepper motors. Different types of stepper motors will be illustrated. Moreover, since the control method can affect motor performance significantly, common control methods are discussed [7]. Chapter 3 is the analysis of the 2D and 3D FEA model. Chapter 4 represents analytical motor equations that are used in motor modeling. Linearized entities will be established. Chapter 5 shows the three models that are constructed in Matlab/Simulink. The working principle and model details are demonstrated. Chapter 6 focuses on the experimental validation and verification of motor dynamics from a physical motor. A test bench is designed on paper to illustrate. Certain motor parameters from the manufacturer are measured. Chapter 7 represents the model results of the thesis. Non-linear parameters are chosen for two methods with and without measurements. Furthermore, three motors with different parameters are further tested. Lastly, Chapter 8 concludes the results of the thesis and suggests possible further studies.

Chapter 2

Introduction to stepper motors

The advantages in precision and torque prove stepper motor a good fit for modern control applications that require high precision and direct control [2]. It is the history and developments from the electromagnetic principles, combining with modern control methods, that created the stepper motor. In this chapter, the history, development, working, and control principle of stepper motors are discussed in detail.

2.1 History

2.1.1 Early stepper motors

Mechanically stepping in angle has always been an interest for motor developments [17]. The first known stepper motor was developed for the British Navy in the 1930s. It was used as a remote position indicator for the torpedo and gun shaft rotations [17]. The three-phase bidirectional variable-reluctance stepper motor shown in Fig. 2.1 was implemented [8]. The rotary switch in Fig. 2.1(a) was used to control the excitation current. One revolution of the handle creates pulses that translate to a mechanical angle of 90°.
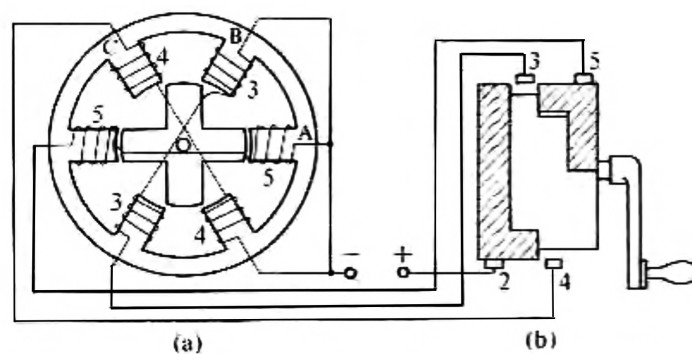
Figure 2.1: Stepper motor used for British Navy [8].

Such a system was also adopted in the US Navy later during World War II. However, such a motor requires to be operated under many precocious conditions. The drive was effective under slow constant-speed application. Moreover, to avoid missing steps, high torque to inertia ratio is required. Because of the prerequisite conditions operating the stepper motor, closed-loop continuous servo motors were still the predominance for stepping applications [17].

Nonetheless, several methods were addressed to improve stepper motor performance at the time. Since the stepper motor used for the British Navy in the 1930s had a low resolution stopping angle of only 90°, a quarter of a circle, methods such as increasing the salient poles are proposed. Shown in Fig. 2.2, the method proposed by C. L. Walker consists of multiple salient teeth in the rotor and grouped small teeth in the stator [8]. The stator teeth are perfectly aligned with the rotor salient teeth. With such

an arrangement, the rotor has a step angle of 3.75°, much smaller than 90°. This kind of setup is also known as the multi-stack variable-reluctance stepper motor nowadays [8].
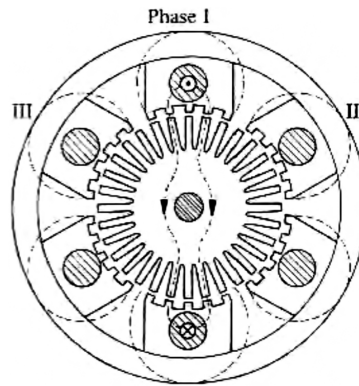
Figure 2.2: Stepper motor with 32 salient teeth [8].

As seen in Fig. 2.2, the magnetic flux flows in the radial direction from the motor shaft axis. To increase the torque production, a sandwich-structured axial machine is also patented by C. B. Chicken and J. H. Thain in 1920. The stepper motor in Fig. 2.3 shows how the sandwiched rotor can create the largest torque from a rotor unit volume [8].
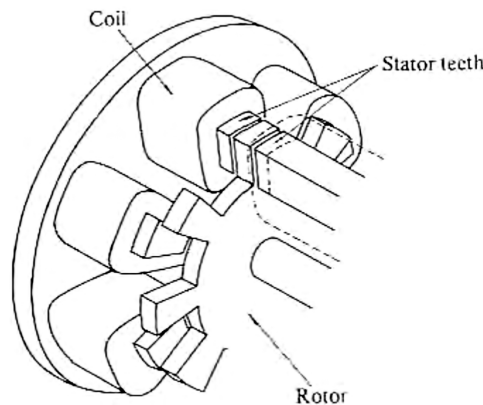
Figure 2.3: Stepper motor with sandwich structure [8].

2.1.2 Digital Control age of stepper motors

In the 1960s, with help from the digital control advancement, variable-reluctance stepper motors can be controlled with fast on-off signals [8]. Such a control scheme increases the use of stepper motors over the closed-loop continuous servo motors. Moreover, the multi-stack variable-reluctance stepper motor was implemented. Shown in Fig. 2.4, the stepper motor consists of three stacks A, B, and C. Each stack has an individual set of stator coils for the corresponding rotor. Increasing in stack count was proven to be an effective method to increase the motor torque [7].
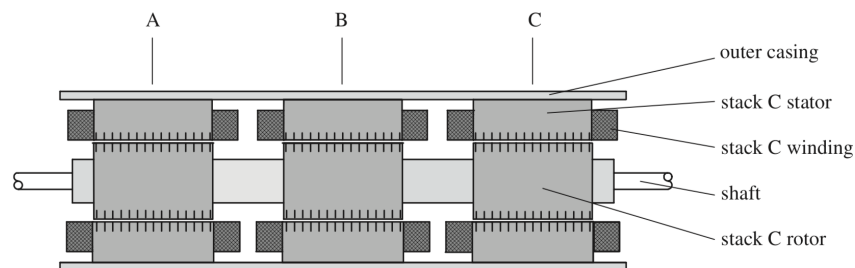
Figure 2.4: Stepper motor with three stacks [7].

6

Moreover, in addition to the digital control and multi-stacked method, several new improvements were brought out during the 1960s [18]. In the 1950s and 1960s, higher magnetic field alloys were developed [19]. The use of permanent magnet gained increasing popularity and became an essential part of stepper motor development [18].

As permanent magnet became the primary type that was used in the 1960s, the stepper motor was slowly dominated by three common types of [20]. First is the variable-reluctance stepper motor that had already been developed since the 1920s. Based on the working principle of magnetic reluctance, the magnetic torque is created through the reluctance of the rotor. The second most dominant type is the Permanent Magnet (PM) stepper motor shown in Fig. 2.5. It gained popularity because of the high torque possible from the magnet [8]. The magnet north and south pole are both in the rotor radial direction similar to that of a synchronous motor. Different types of PM stepper motors such as the salient magnet rotor were also developed. The third most dominant stepper motor is the hybrid stepper motor. Shown in Fig. 2.6. The hybrid stepper motor combined the principles of permanent magnet in the PM stepper motor and reluctance in the variable-reluctance stepper motor. Yet, different from the permanent magnet, the magnet is positioned in the axial shaft direction between the rotor stacks. Such geometry benefits from gaining the flux both axially shown in Fig. 2.6(a) and radially shown in 2.6(b).
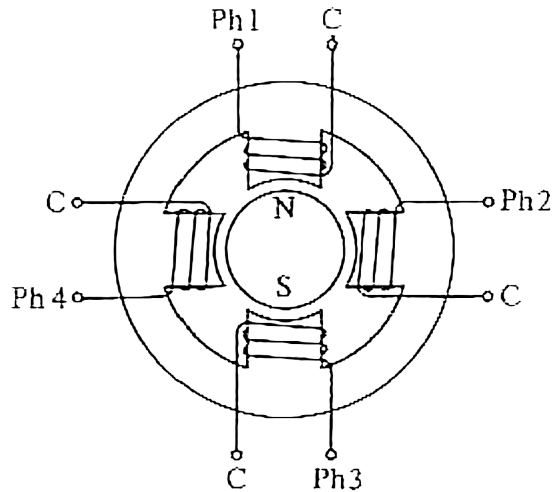

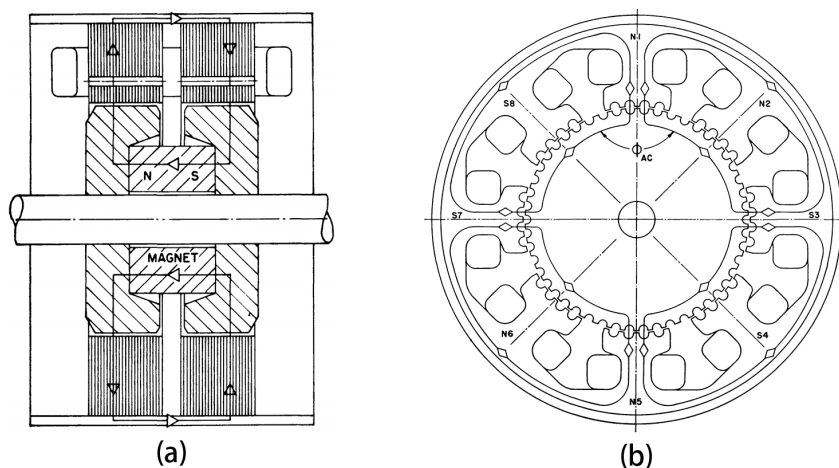Figure 2.5: Permanent magnet stepper motor [8].

Figure 2.6: Hybrid stepper motor (a) axial view (b) cross-sectional view [18].

2.1.3   Microprocessor advantages to modern stepper motors

While hybrid stepper and PM stepper motor gains higher torque from their magnet and has a relative linear torque versus torque characteristic, their manufacturing cost is often high. Because of that, Variable Reluctance (VR) stepper motor mainstreamed in the 1970s for its low cost and moderate speed characteristics [21]. These VR stepper motors were used mainly for electronic printers and business machines [8].

To run the stepper motor and obtain the stepper motor characteristics, not only is the mechanical setup essential, but it is also important to run the motor under the correct control sequence and method. Since the 1960s, switching control has already been discussed and developed [18]. However, it is not until the 1970s and 1980s when much faster control is possible due to microprocessor improvements [8]. That is when the hybrid stepper motor started to gain its popularity due to more effective manufacturing, lower control costs, and most of all, smaller step angles. Such advantages have boosted the design and varieties of hybrid stepper motor until today [7].

2.2   Stepper motor basic characteristics

The hybrid motor is a combination of both VR and PM stepper motor. The variable reluctance creates teeth saliency that guides the magnet flux toward the correct stator path. As a combination of both types of stepper motors, the basic principle of a stepper motor can be illustrated with the three-phase VR stepper motor shown in Fig. 2.7. The three-phase VR stepper motor consists of four teeth non-magnetic rotor and six stator teeth. The rotor and stator cores are usually built with a laminated silicon steel structure. With silicon steel's high permeability, magnetic flux can pass through both the rotor and stator easily. In Fig. 2.7 , the rotor and stator have same teeth widths. A small air gap, typically between 0.02 mm to 0.2 mm, allows flux to flow with minimal magnetic reluctance [20]. Such a change in magnetic reluctance gives a preferred rotor rest position when the flux is supplied, hence, giving this type of motor the name variable reluctance stepper motor.
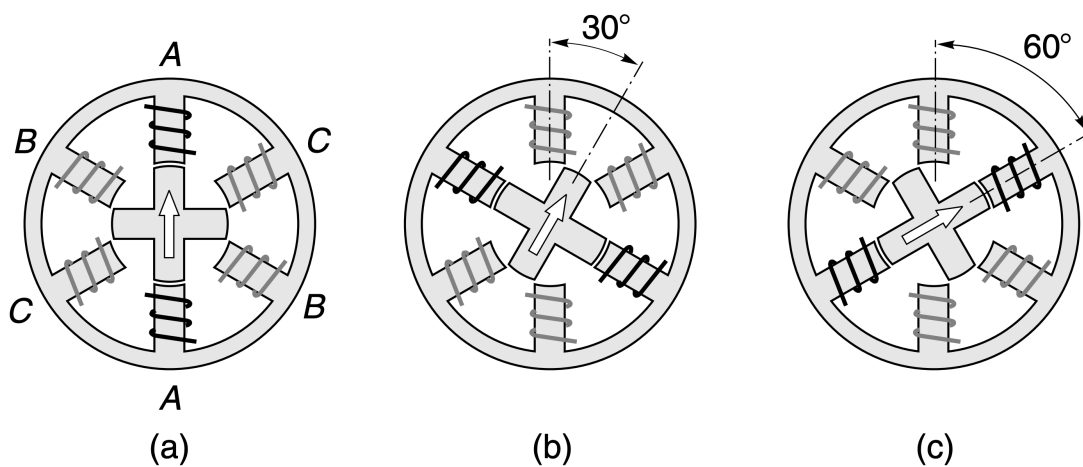
Figure 2.7: Stepping motion of variable reluctance stepper motor [20].

With three phases A, B, and C, the coils are winded in series between opposite pairs of stator poles. With such a connection, two opposite magnetic poles are generated on the stator poles, thus creating a strong flux linkage through the rotor core. By supplying a direct current through switches to such coils and controlling the switches with ON and OFF excitation, the respective magnetic flux is created in the stator poles. In Fig. 2.7, dark lined coils represents a turned ON state. With phase A turned ON in Fig. 2.7 (a), the rotor is automatically positioned to align with the phase A coils. Such positioning is an automatic reaction to minimize the magnetic reluctance or magnetic resistance in the motor. In Fig. 2.7 (b), phase A is then switched OFF while phase B switched ON. The rotor then re-positioned and turned 30° clockwise to reduce the magnetic reluctance between the rotor and stator. Similarly, the rotor again turned 30° when phases A and B are deactivated and phase C is activated in Fig. 2.7 (c). While the rotor tries to position itself toward equilibrium to reduce the magnetic reluctance, it also produces a torque that opposes any torque that moves the rotor away from minimal magnetic reluctance position. That

is, if an external torque is given to move the rotor from equilibrium, a counter-torque will be created by the motor to oppose the move.

Such produced circular motion is fully controlled by the one-phase-on sequential operation. Respected rotor teeth are pulled to align with the stator teeth. Since one step is 30° misaligned with the next, stepping is done through the sequential excitation in the stator. Similarly, the PM stepper motor uses the same principle as the VR stepper motor. With a two-phase PM stepper motor shown in Fig. 2.8, the rotors are replaced with permanent magnets either with or without reluctance. Without reluctance, the magnet provides an extra source of magnetic field that interacts with the magnetic flux.
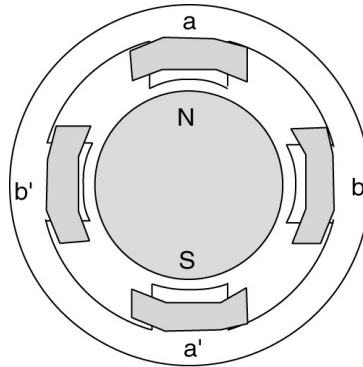
Figure 2.8: Cross-sectional model of permanent magnet stepper motor [22].

2.3 Hybrid stepper motor operation principle

Combining the VR and PM stepper motors, the hybrid stepper motor is created under a similar principle. Hybrid stepper motor gains its torque through the magnetic flux linkage created from the magnet, variable reluctance rotor teeth, and stator coils. A unique setup applied in the hybrid stepper motor is shown in Fig. 2.6 (a). In a hybrid stepper motor, the magnetic flux is produced in both the axial and radial directions. The co-centric circular structure in the rotor consists of two lamination stacks and a center magnet that is magnetized in the axial direction. Such a structure creates the main axial directional magnetic flux path shown in Fig. 2.9 (a).
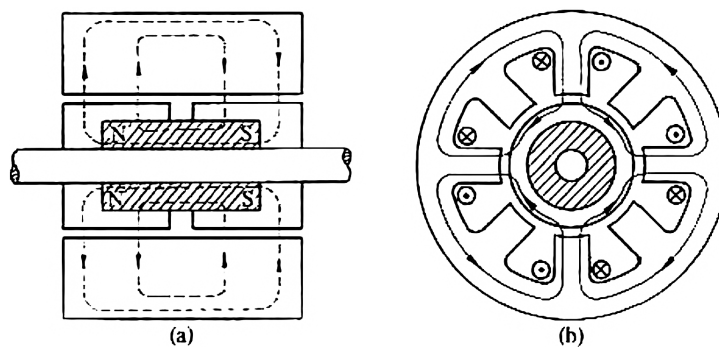
Figure 2.9: Magnetic flux path of hybrid stepper motor model (a) axial directional flux (b)radial directional flux [8].

The multi-teeth per pole structure shown in Fig. 2.10 is also mainly applied in the hybrid stepper motor. The eight stator poles each carries a phase coil that consists of five teeth per pole. Such geometry highly decreases the step angle and increases the number of steps per revolution. The radial magnetic flux path is shown in Fig. 2.9 (b) follows the stator teeth and pole direction. While such structure can be applied in a VR stepper motor, more teeth however highly decrease the reluctance variance and reluctance torque in the VR stepper motor. The small misalignment between the stator and rotor shown in Fig. 2.10, 1.8-degree step size is achieved.
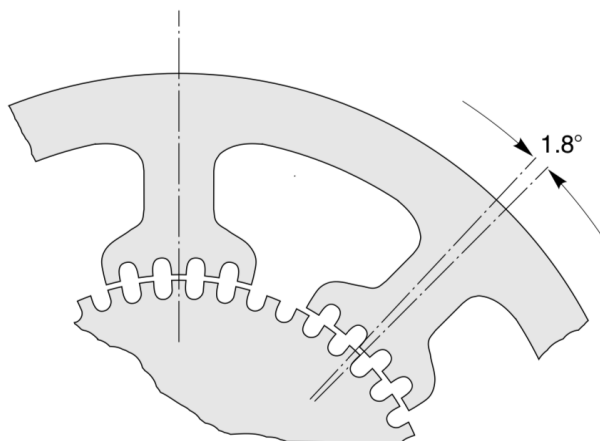
Figure 2.10: 1.8-degree multi-teeth per pole structure [20].

Another important aspect of the geometry of a hybrid stepper motor shown in Fig. 2.11 is that the two rotor lamination stacks are misaligned with each other by half a tooth pitch [8]. Such a misaligned structure ensures the flux lines flow through the stator in both the radial and axial directions correctly to produce the motor torque. With the misalignment, without any excitation in the stator coils, flux flows from the magnet N side in Fig. 2.9 (a) through the rotor lamination stack to the stator and flows back from the stator through the misaligned rotor lamination stack back to the magnet S side. Such a path effectively cancels out the strong periodic alignment torque, or detent torque, that is usually seen in a PM stepper motor. Therefore, the hybrid stepper motor not only benefits from both the axial and radial torque, but it also has a much lower detent torque and a much higher number of steps per revolution.
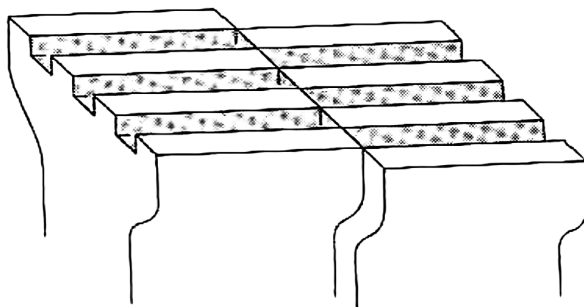
Figure 2.11: Misaligned rotor lamination stacks [8].

2.4   Two-phase motor coil structure

While the stepper motor can be directly controlled by the switching sequence of the driving voltage. Two main coil winding techniques are applied in a two-phase stepper motor. They are the bifilar and unifilar winding structures shown in Fig. 2.12.

Figure 2.12: Motor coil structures (left) bifilar winding (right) unifilar winding [20].

In Fig. 2.12 (left), two coils are winded in parallel to each other. With this method, twice amount of turns is fitted into the area between the stator poles. Such a method operates under a simple topology that current flows in a single direction within the same coil and is often deployed in a unipolar structure stepper motor. Oppositely, the unifilar setup is shown in Fig. 2.12 (right) only hosts one strand of coils per stator slot. Unifilar setup is often deployed in bipolar stepper motors.
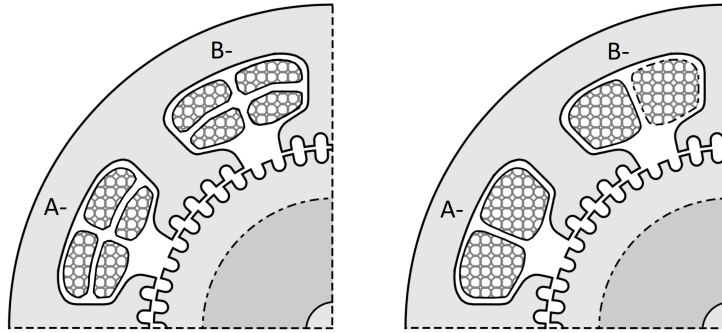
Unipolar stepper motor circuits are often connected as shown in Fig. 2.13 (a) and (b). In the series unipolar connection, the excitation is often connected via half point of the coils and either end of the phase circuit. Such a method has the positive and negative input connected to two of the three connections on one phase. The third connection is usually connected to the ground. The positive and negative excitation is then applied directly such that they are directed toward common ground. With uni-directional current to the ground, control is simplified in this circuit. Similarly, the parallel unipolar circuit has two sets of coils in one phase. Such a method provides a simple one-to-one connection via each phase. In both unipolar structures, series unipolar often needs twice the amount of voltage to excite because of the reference to the ground. The unipolar stepper motors have the advantage to connect to low complexity non-inverting voltage drivers.

Bipolar stepper motor circuits are often connected as shown in Fig. 2.13 (c). As the name suggested, the current flows in both directions per phase coil. Such a method requires a more sophisticated H-bridge driver circuit for the current polarity switch.
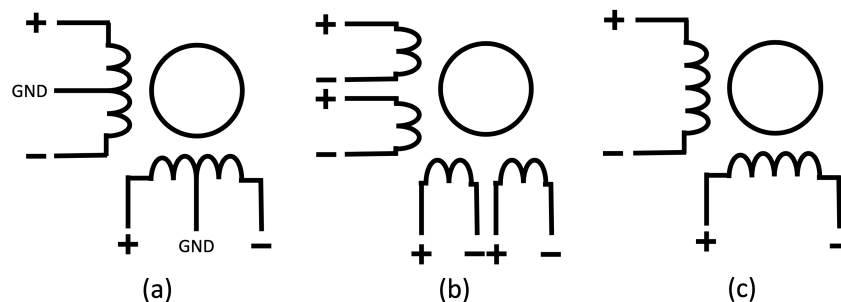
Figure 2.13: Motor coil circuits (a) series unipolar circuit (b) parallel unipolar circuit (c) bipolar circuit.

Both unipolar and bipolar structures are being used in stepper motors nowadays. Both series and parallel unipolar stepper motors have the benefit of simple driver circuits without H-bridge. On the other hand, the bipolar stepper motor has the benefit of higher torque per motor area because of the fully used coil length in the motor.

2.5 Control Methods

Since stepping motion is translated directly from the driver circuit control, the control method of a stepper motor can highly affect the stepper motor performance. Stepper motor control is often controlled in three different methods, that is, the full stepping, half-stepping, and micro-stepping.

2.5.1 Full stepping

Under full stepping, the stepper motor is excited in sequences that turn the rotor shaft one pole phase increment. Typically, two control methods are applied shown in Fig. 2.14, illustrated with a simple two-phase stepper motor. Under single-phase excitation, one phase is excited per increment. With such a control method, the least amount of power is supplied since only one set of coils is excited. Comparatively, the two-phase excitation is done with two coils excited per increment. Such a method creates about twice the amount of torque from both phases. However, this also means twice the amount of power is drawn by the stepper motor.
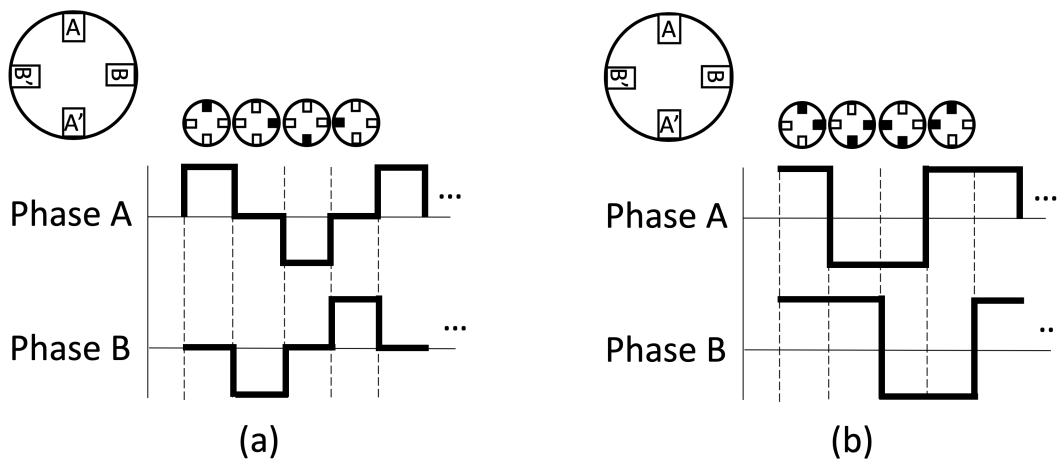
Figure 2.14: Full stepping excitation (a) One-phase excitation (b) Two-phase excitation.

2.5.2 Half stepping

Under half-stepping, the stepper motor is excited with a combination of one-phase and two-phase excitation of the full stepping. Such a method has the advantage of increasing the number of steps by halving each step incremental. Since the power supplied is oscillating between two-phase and one-phase excitation, the power consumed is also in between the one-phase and two-phase full stepping method. Similarly, the torque is oscillating between the one-phase and two-phase full stepping method at about three forth the two-phase excited full stepping method. Although increasing the number of steps is an advantage of such a method, the torque produced is also oscillating. This can be a disadvantage when the torque is required to be stable in certain applications.
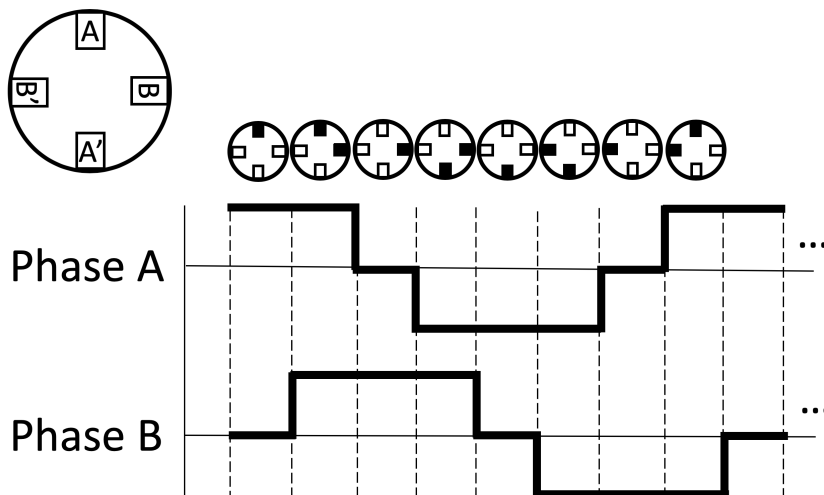
Figure 2.15: Half stepping excitation.

2.5.3 Micro-stepping

Micro-stepping is another method that is often applied in the control of stepper motors. The fundamental of such method is to divide the motor steps into multiple current levels. Most of them in the 32 to 256 levels. Nonetheless, the current levels are controlled to follow a sinusoidal waveform to provide a smooth transition in stepping response. As illustrated in Fig. 2.16, the stepping is done with ten micro-steps. By doing so, the rotor rotation is transitioned smoothly to the next phase angle. Such a method proves to decrease oscillation that can usually be seen in stepper motors because of the rotor inertia. However, because of the higher number of positions, the torque is also reduced from both the full and half-stepping method.
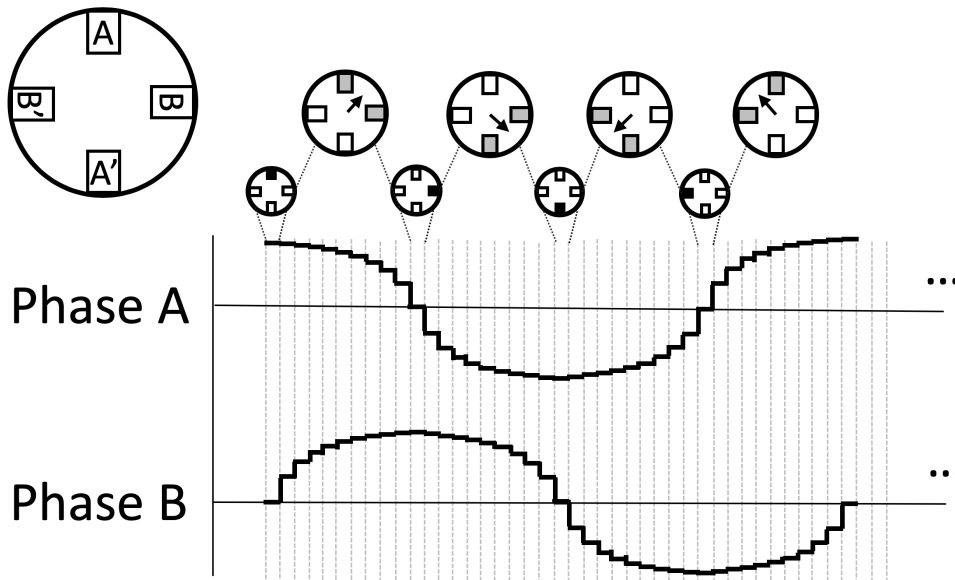
Figure 2.16: Micro-stepping excitation.

2.6 Stepper motor choices

The two-phase bipolar hybrid stepper motor will, therefore, be analyzed in this thesis due to its small step size, relatively high speeds, and high torque to price ratio [9]. With the different parameters provided by the manufacturers, it is also one of the most abundant stepper motors that can be easily obtained. The controlling of stepper motors, such as full-stepping or half-stepping, will be applied based on the methods each motor's datasheet parameters are obtained.

Chapter 3

Electromagnetic Analysis

3.1 Motor Selection

In this research, a NEMA 17 hybrid stepper motor shown in Fig. 3.1 is selected for further investigation. It is chosen because of its easy accessibility and standardized structural dimension. The ST4209L1704 NEMA standard motor used in this thesis refers to the 1.7-inch motor face-plate. The motor is chosen with 0.9 -degree step size and a double-stacked rotor. To increase total torque, a multi-stack rotor is usually cascaded together [8]. As seen in Fig. 3.2, ST4209L1704 has two rotor stacks or four lamination stacks. Two lamination stacks are cascaded with a magnet (shown in red) to form one rotor stack. Similarly, the bipolar motor is selected because of its larger magnetic field compare to a uni-polar setup [8].
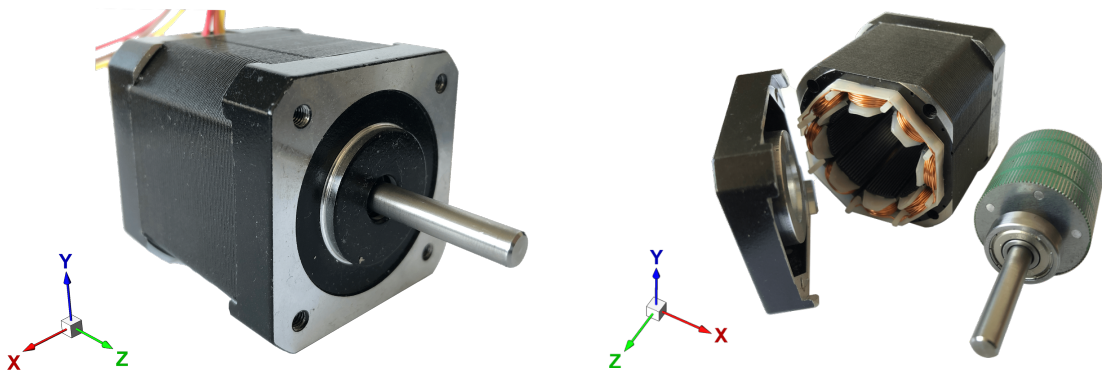
Figure 3.1: ST4209L1704-A NEMA 17 motor.
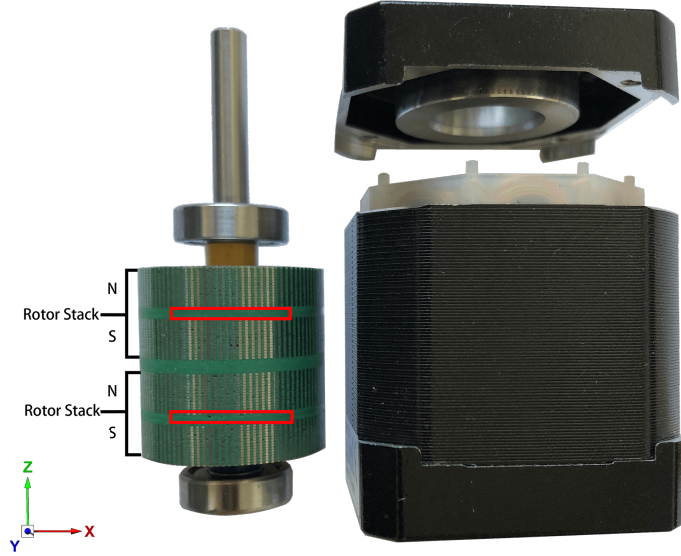
Figure 3.2: ST4209L1704-A NEMA 17 steppermotor.

The motor parameters of ST4209L1704 are given in Table 3.1. Here, specifications are measured under different conditions listed in the motor parameters. The holding torque is measured with two-phase excitation, therefore, the motor parameters represent the vector summation of both phase A and B holding torque from the stepper motor. The back-emf, on the other hand, is measured on a single-phase coil. Such parameters are also applied to the models in the later stage of the research.

Table 3.1: ST4209L1704-A motor parameters.

Symbol	Description	Value	Unit
U_{rated}	Voltage	3	[V]
I_{rated}	Nominal current (phase)	1.68	[A]
R	Resistance (phase)	1.8	[Ω]
L	Inductance (phase)	5	[mH]
τ_h	Holding torque (peak)	0.44	[Nm]
τ_{dm}	Detent torque (peak)	0.0132	[Nm]
Θ	Step angle	0.9	[°]
U_{emf}	Back-emf (300 rpm)	6	[V]
J	Rotor inertia	6.8E-6	[kg-m^2]

3.2 Motor Structure

To precisely model the electromagnetic performance, it is important to gather the physical dimensions and geometries of the stepper motor. The motor is disassembled and measured with different measuring tools. A Mitutoyo 412670 caliper is used for the teeth dimensions on both the rotor and stator. Also, stator winding is uncoiled for the coil thickness and number of turns.

Figure 3.4: Stator of the stepper motor.

Figure 3.3: Rotor of the stepper motor.

Since flux lines circulate through the stator and rotor lamination stacks before returning to the magnets, the pole-teeth width and depth and lamination stack thickness are physically measured. As seen in Fig. 3.3, the rotor has equally spaced teeth. The axial position of the rotor is aligned with the x-axis. With the variables from Table 3.1, the step angle is obtained from

$$\Theta = \frac{360°}{2mN_r},\tag{3.1}$$

where N_r is the number of rotor teeth, and m is the number of poles per phase. The number of rotor teeth is also counted as 100. As seen in Fig. 3.4, the stator also has equally spaced poles with ten teeth on each pole. Since the stator tooth pitch is measured to be smaller than the rotor tooth pitch, according to [23], the number of stator teeth on unequal pitch design stepper motor can be calculated by

$$N_s = N_r + m,\tag{3.2}$$

where the N_s is the number of stator teeth that are calculated to be 102. Since there are eight poles in this motor, only 80 stator teeth are physically constructed with ten teeth on each stator pole. Such setup equates to a 90° electrical angle stator tooth pitch. Nonetheless, we can obtain the equally spaced 3.529° stator teeth angle from a 360°/102 mechanical angle.

The list shown in Table 3.2 are some of the physical dimensions that are measured.

Table 3.2: ST4209L1704-A measured dimensions

Geometry name	Description	Dimension	Unit
TH_LAM	Lamination thickness (rotor/stator)	0.35	[mm]
N_LAM_STACK	Number of lamination per stack	15	[-]
D_ROTOR	Rotor diameter	25.87	[mm]
H_TEETH_ROTOR	Rotor teeth height	0.3	[mm]
W_TEETH_ROTOR	Rotor teeth width	0.38	[mm]
D_STATOR	Stator inner diameter	25.97	[mm]
D_STATOR_OUT	Stator outer diameter	45	[mm]
H_TEETH_STATOR	Stator teeth height	0.4	[mm]
W_TEETH_STATOR	Stator teeth width	0.4	[mm]
L_STATOR_BI	Stator pole back iron height	1.4	[mm]
GAP	Air gap length	0.05	[mm]
D_SHAFT	Shaft diameter	5	[mm]
N_COIL	Number of coils	38	[-]
TH_WIRE	Wire thickness	0.45	[mm]
D_MAGNET_IN	Magnet inner diameter	7	[mm]
D_MAGNET_OUT	Magnet outer diameter	19.94	[mm]
TH_MAGNET	Magnet thickness	1.45	[mm]

One important detail on the 0.9-degree step size motor can be seen in Fig. 3.4. With 10 equally spaced teeth per pole, the poles are shifted to match the equally spaced 102 teeth per circumference in the stator. The A- pole of the 0.9-degree stepper motor is shifted clockwise by half a teeth width. This can only be seen when the teeth counts on the stator are not divisible by four shown in Fig. 3.5(b). The red shows that the stators are not equivalent to the dividing edges. For example, a 1.8-degree step size motor will have equally spaced teeth per pole because 52 stator teeth calculated by Eq. 3.2 is divisible by four shown in Fig. 3.5(a).
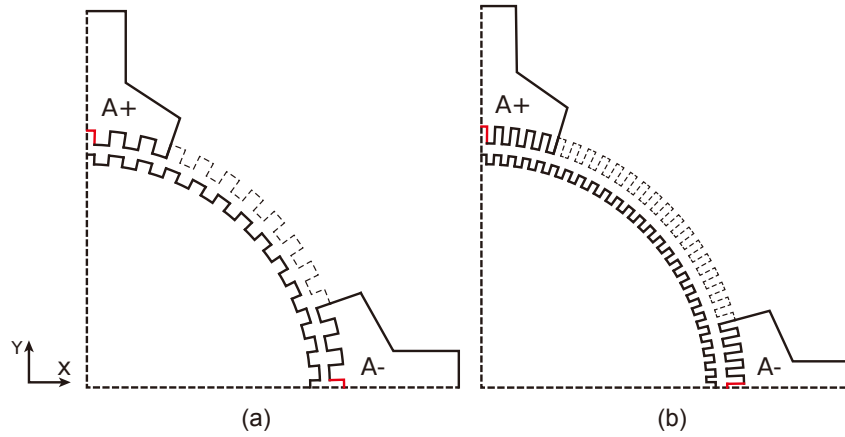

Figure 3.5: Stator and rotor structures (a) 1.8-degree stepper motor (b) 0.9-degree stepper motor.

3.3   Motor Materials

Since stepper motor materials are not given by the manufacturer, motor material properties have to be either curve fit, measured, or estimated. They are steel, copper, and magnet.
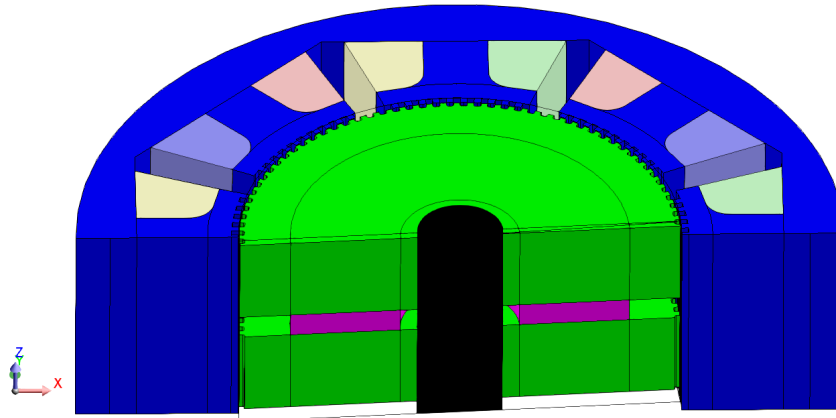

Figure 3.6: 3D model motor materials representation.

Table 3.3: Motor material indications

Color	Material
Blue	Silicon steel stator
Green	Silicon steel rotor
Light pink	Copper coil phase B+
Light purple	Copper coil phase B-
Light yellow	Copper coil phase A+
Light green	Copper coil phase A-
Black	Steel shaft
Magenta	Neodymium magnet

Materials in the stepper motor are shown in Figure 3.6 and Table 3.3. These four main materials are:

- Silicon steel lamination:
  Silicon steel is the possible material that is used for both the stepper motor rotor and stator. Silicon steel is most possibly used because of the increased resistivity from silicon added to the steel. Furthermore, with its high permeability and high saturation property, it helps the high concentration of flux in the stepper motor [24]. Often used in between large rotating machines and high-efficiency power transformers, Cogent M270-35A is chosen to represent the non-oriented silicon steel used in the ST4209L1704 stepper motor [25]. It has a magnetization saturation property of 2 T and relative permeability of 1.6×10^4. Nonetheless, when applying the silicons steel as lamination in the FEA, a stacking factor of 96% is applied [25].

- Copper coils:
  Copper wire is measured with the caliper to have a 0.45 mm diameter. Since insulated copper coils are standardized, we can safely assume the copper wire used here is an enameled magnet wire.

- Non-magnetic steel shaft:
  The steel shaft is often non-magnetic in a motor to minimize disturbing the concentration of flux linkage in the lamination stack. Since the permeability of non-magnetic steel is very close to that of the air, the steel shaft in the ST4209L1704 stepper motor is set to have a permeability of air.

- Neodymium magnet:
  The neodymium magnet represents the maximum flux linkage of the motor under zero excitation. Since the magnet B-H curve can be defined by a simple linear magnet model described by the remanent flux of the magnet, it is important to obtain both the correct remanent flux and relative permeability. Remanent flux is defined as the magnetism left behind a ferromagnetic material after the external magnetic field is removed [26]. In other words, it is the magnetic strength of a magnet.

  Since it is important to obtain a magnet property that near-identical to that of the physical magnet. The neodymium magnet remanent flux and relative permeability are obtained by curve fitting the magnetic strength at point B with multiple distances from the magnet shown in Fig. 3.7. The red dots are shown in Fig. 3.8 represent different heights above the magnet at point B. The magnetic flux density is measured with a Lake Shore F71-LSA25CS gaussmeter to obtain the magnetic flux density at the red dot positions. The x and y position on the magnet is fixed while the z red dot positions are measured from 0.1 to 1 mm with a 0.1 interval.
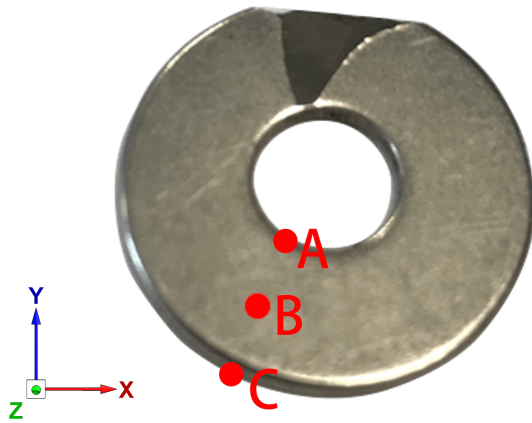
Figure 3.7: Rotor magnet.
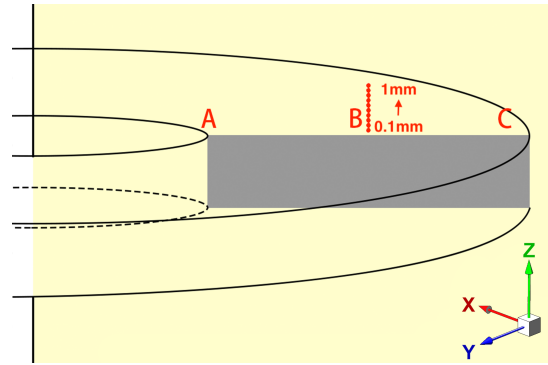
Figure 3.8: Rotor magnet FEA model.

With such physical measurement, a 2D FEA model is constructed as shown in Fig. 3.8 to determine the magnetization correctly. The magnetic field strength is shown in Fig. 3.9.
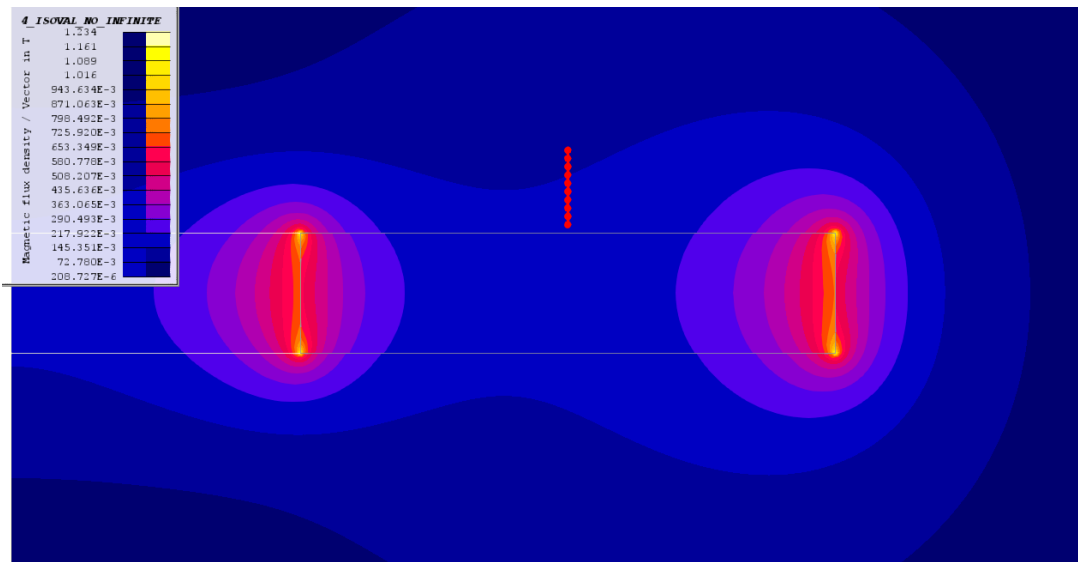
Figure 3.9: Simulated magnet magnetic field strength.

The remanent flux and relative permeability are both selected in the FEA model by curve fitting the measured to the simulated magnetic flux density at different heights. The simulated curve is within 1% of the measured curve shown in Fig. 3.10. Such error can be caused by small shifts in x-y position in location B shown in 3.7. The remanent flux is selected through an iterative approach where a small change of 0.01 T in the magnet remanent flux and 0.01 in permeability is applied each iteration until the curve fits within 1% of the measured curve. An assumption of a linear magnet model is used when 1.37 T for Br and 1.1 for initial relative permeability is selected to best fit the curve.
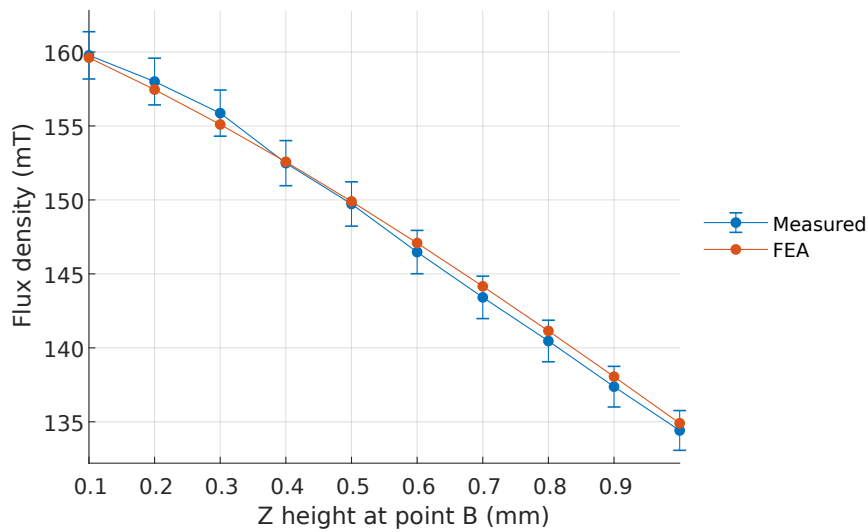
Figure 3.10: Magnetic flux density curves.

3.4   Finite Element Modeling

Physical measurements of motor non-linear entities require precise measuring tools. Measuring non-linear entities such as magnetic flux and detent torque requires high tolerance measuring tools against noise created under an operating motor. These measuring noises often translate to higher harmonic noises and can disturb the measurement outcome. Finite element modeling can provide an insight into the dynamics of a stepper motor without a physical measuring tool. FEA models are constructed with the physical geometry and materials listed in 3.2 and 3.3. With the FEA model constructed, validation of the model is then done by comparing datasheet and manufacturer given parameters to the simulation results. Altair FLUX2D and FLUX3D software are employed as finite element software.

3.5   2D Finite Element Modeling

While a 3D model simulates the whole motor structure, it, however, contains a higher number of meshing elements and subsequently requires a longer computation time. On the other hand, a 2D model reduces the computation by simulating only a plane structure of the motor. A 2D model is proven to be as accurate as a 3D model when radial flux machines such as induction machines are simulated [15]. With the reduction in computation, a 2D model of a stepper motor is first attempted to simulate the detent torque of the stepper motor.

Since the hybrid stepper motor has both axial and radial directional magnetic flux, a method to estimate the 3D axial flux with a 2D radial flux representation is applied [27]. A virtual magnetic field barrier is constructed to limit the magnetic flux toward a single-pole to roughly form the equivalent flux concentration at each tooth's air gap. These concentrated fluxes then produce a detent torque that estimates the actual detent torque.

3.5.1   Geometry and materials

The 2D model is shown in Fig. 3.11, where the yellow edges are the virtual magnetic field barriers. The dimensions in Table 3.2 are applied to the model. The materials used in the model are shown in Table 3.4. Here, the stator teeth are uniformly distributed while the stator poles are shifted to compensate with the equally distributed stator teeth discussed in Section 3.2.
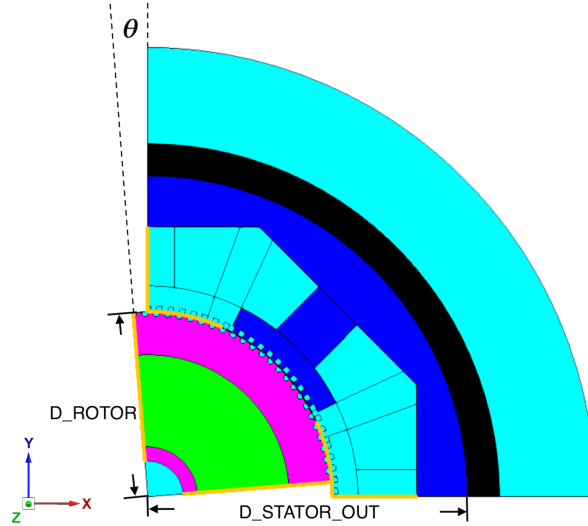
Figure 3.11: Single-phase quater model (Yellow line represents the magnetic barrier).

Table 3.4: 2D model material indications

Color	Material
Turquoise	Air and infinite box
Blue	Silicon steel stator
Magenta	Silicon steel rotor
Black	Air
Green	Neodymium magnet

3.5.2 Model setup

In Fig. 3.11, a single stator pole quarter model is constructed to compensate for the rotor teeth. In such that it is simply not possible to construct a periodic quarter model with all stator poles. This is because the 0.9-degree stepper motor has an unsymmetrical stator pole position shown in Fig. 3.5. Because of that, a single stator pole is represented by setting the other poles to air regions.

An odd periodicity with four repetitions is applied in the model. Odd periodicity has an anti-cyclic boundary condition applied automatically. No symmetry is applied. Also, an infinite box is applied toward the edge of the outer stator. An air region (shown in black) is automatically applied through FLUX infinite box.

Meshing is done by applying an automatic meshing from Flux2D. Dynamic meshing with 0.75 deviation and 0.25 relaxation on both relax-face and relax-line is applied. A positive radial magnetic field orientation is applied to the magnet. Model setup is shown in Table 3.5.

Nonetheless, in Fig. 3.11, the virtual magnetic barriers are also set up according to [27]. The virtual magnetic barriers are set to be a 3-meter air gap in the model. To correctly guide the flux toward the stator pole under a radial magnetic flux direction, such barriers are used to direct the flux toward the motor flux path.

Table 3.5: 2D model setup

Model setup	
Periodicity	Odd (anti-cyclic boundary condition)
Symmetry	N/A
Infinite box	Applied Disc
Magnet orientation	positive radial direction
Meshing	Automatic

3.5.3   Virtual magnetic barrier

The virtual magnetic barrier applied by setting the line regions to one-meter-thick air regions. The simulated flux lines are shown in Fig.3.12.
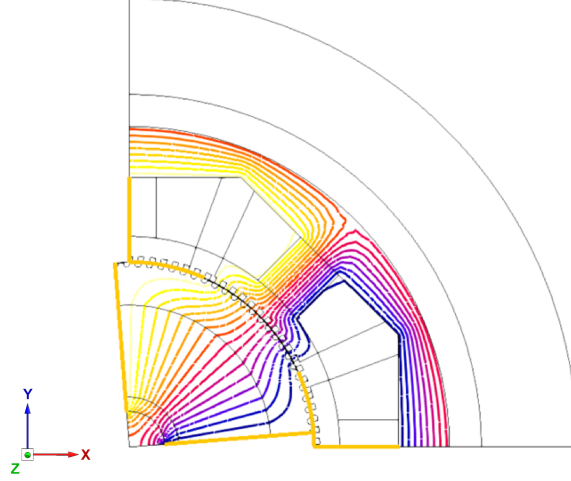
Figure 3.12: Flux lines on 2D quarter model.

Since the magnetic motive force is produced within the air gap, the flux lines in the air gap shown in Fig. 3.12 are essential to find the correct detent torque. The detent torque is measured directly from the FLUX2D software. With the distribution changes on the teeth and air gap, detent torque is obtained by the Maxwell Stress Tensor Method that is implemented directly from FLUX2D. The outcome detent torque with 0°motor spacial angle is shown in Fig. 3.13.
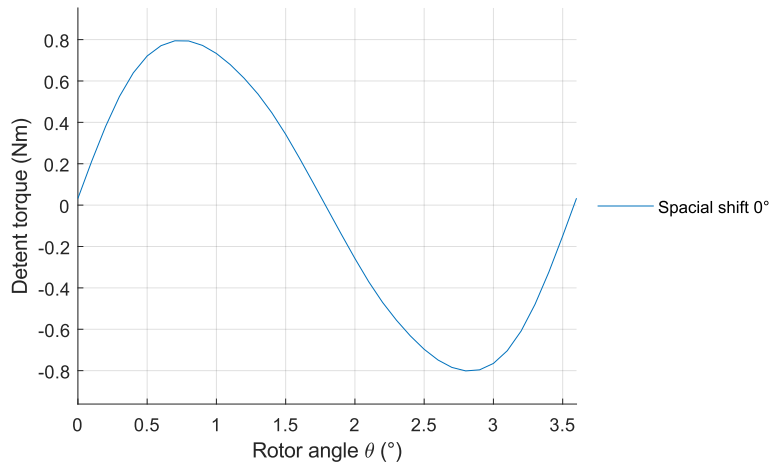
Figure 3.13: Radial detent torque waveform (2D quarter model).

However, the waveform in Fig. 3.13 only represents the detent torque from radial direction flux. The detent torque has to represent both the radial and axial flux. As stated in [27], the axial and radial direction magnetic flux can be calculated by

$$\Phi_{radial} = B_r L \theta_{model} r_1, \tag{3.3}$$

and

$$\Phi_{axial} = B_r S_1, \tag{3.4}$$

where the B_r is the remanent flux of the magnet, L is the thickness of the magnet 1.45 mm, r_1 is the inner radius of the magnet 3.5 mm, θ_{model} is the total angle of the magnet that is modeled to 90°, and S_1 is the area of face surface area of the magnet 136.8 mm^2. Therefore, Fig. 3.13 represents the radial flux that is produced by the magnet. The ratio of the axial and radial flux is calculated through Eq. 3.3 and 3.4 to be 68.448:10.1599. The total flux is then applied to the waveform in Fig. 3.13 by multiplying the ratio

$$\Phi_{total} = \frac{\Phi_{radial} + \Phi_{axial}}{\Phi_{radial}}. \tag{3.5}$$

The waveform is shown as the red line in Fig. 3.14. Since the quarter model only represents one-fourth of the final detent torque, in Fig. 3.14, the detent torque is added up four times with 90° spatial phase shift. The green wave in Fig. 3.14 and Fig. 3.15 is the full detent torque.
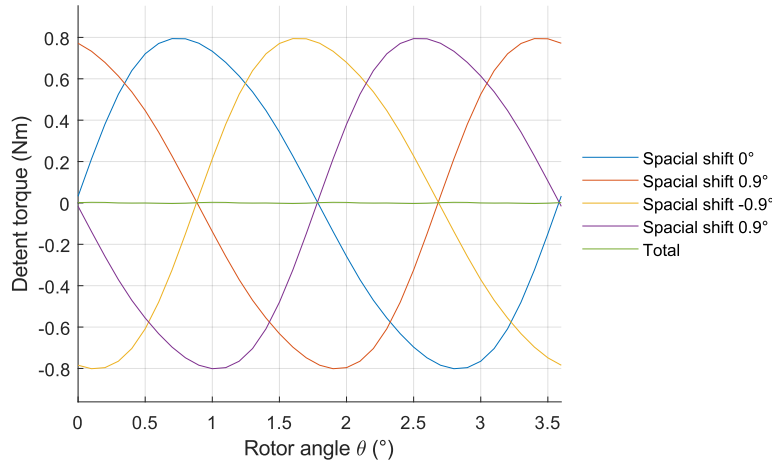
Figure 3.14: Shifted detent torque waveform (2D quarter model).
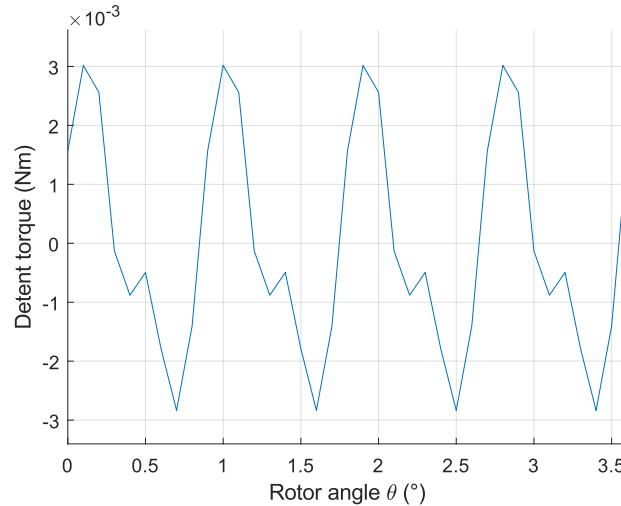
Figure 3.15: Sum detent torque waveform (2D quarter model).

The detent torque in 3.15 shows a clear 4th harmonic domination. However, multiplying the two magnets in the stepper motor, the outcome of only 44% of the datasheet detent torque. The output shows a clear discrepancy with respect to the datasheet. the discrepancy can be caused by the nature of the flux line and angle difference between axial and radial flux. These are just impossible to model with 2D FEA since 2D FEA doesn't have a 3D structure. Additionally, the unequal teeth shift shown in 3.2 is not present in the quarter model. Therefore, the unsymmetrical second harmonic is not present in the outcome of the 2D FEA quarter model.

3.5.4 Fillet structural comparison

Although the model with a virtual barrier only produces 44% of the datasheet detent torque, the structure comparison with different fillet arc lengths can still be applied. Since comparison is done for the outcome of the virtual barrier model, the effect of fillets can still be analyzed. In the geometry of the stepper motor, fillets are present among rotor teeth, stator teeth, and stator structure. Since the fillet arc radius in both the rotor and stator teeth structures are within 0.2 mm, to correctly measure the fillet arc radius requires an accurate fillet gauge that is not available for this thesis.

The effects of these fillets are done through a single-pole 2D FEA model detent torque comparison. It is analyzed with different fillet radius among rotor teeth, stator pole, and stator bridge shown in Fig. 3.16.
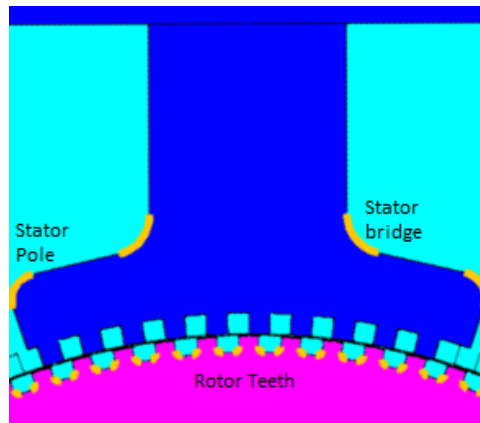
Figure 3.16: Arcs from stepper motor structure.

Different arc radii are applied separately to the three parts. The analysis is done by measuring the effects on the detent torque. The effects of the fillets on detent torque can then be taken into account in both the 2D and 3D FEA modeling. The effects on each of the fillet radius are shown in Fig. 3.17, Fig. 3.18, and Fig. 3.19.
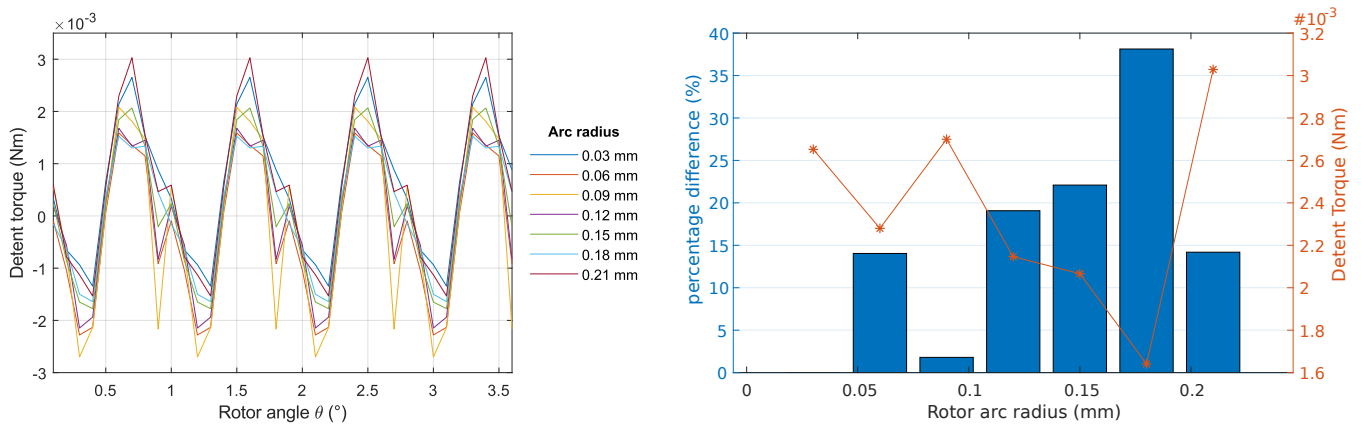
Figure 3.17: Rotor teeth arc radius vs. detent torque.
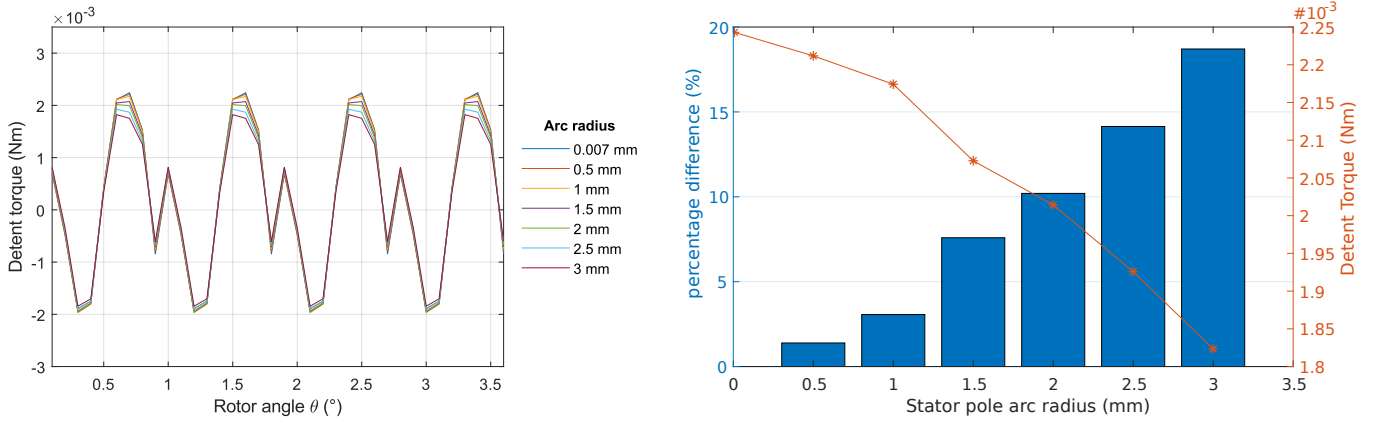
Figure 3.18: Stator pole arc length vs. detent torque.
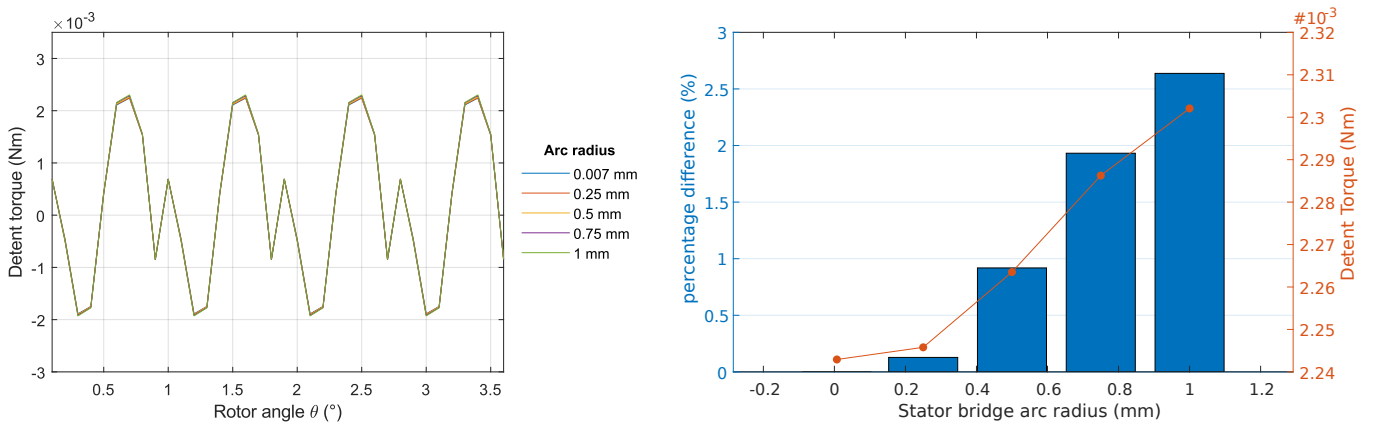
Figure 3.19: Stator bridge arc length vs. detent torque.

In the bar graph of Fig. 3.17, there is a difference in detent torque among different arc radius. With a 0.2 mm rotor teeth arc radius increase, detent torque had a 40% change. In the bar graph of Fig. 3.18, with 3 mm stator pole radius increase, detent torque encountered a 20% change. In the bar graph of Fig. 3.19, with 1 mm stator bridge arc radius increase, detent torque had a 2.5% change. A clear indication of the change in detent torque to change in arc radius can be seen in both the stator pole and rotor teeth geometry. Therefore, the rotor teeth and stator pole arc radii is roughly measured and implemented with the caliper.

3.5.5 Summary

The 2D model is constructed to obtain the detent torque of the stepper motor. Firstly, with the nature of two-dimension modeling, a three-dimensional flux path is not simulated in two dimensions. A magnetic barrier is applied to simulate the axial flux of the motor. However, it is not sufficient enough for an accurate representation. Secondly, the geometry of the fillet arc radii was compared. With a more significant effect on detent torque, stator pole and rotor teeth arc is implemented in the FEA models.

3.6 3D Finite Element Modeling

To fully obtain the dynamics of the stepper motor, a 3D model is then built and analyzed. The 3D model also takes into account the rotor lamination, magnet thickness, and physical copper coil. Nonetheless, the magnetic flux can follow the 3D paths.

3.6.1 Geometry and materials

The geometry and materials follow the motor material representation in Table 3.3. Here, the 3D model is a half model of a single stack rotor (quarter model of a two-stack cascaded rotor) shown in Fig. 3.20. The magnet is positioned in the center of two rotor stacks following the physical motor structure shown in Fig. 3.2. The magnetic flux of the magnet is also set up in the axial Z direction.
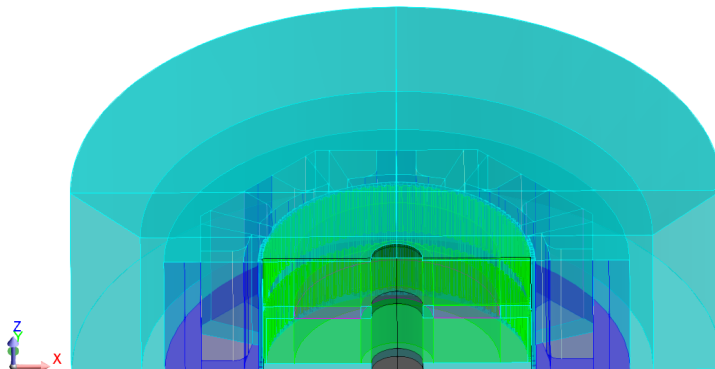
Figure 3.20: 3D model with infinite box.

3.6.2 Model Setup

To fully represent the two-stack cascaded rotor of the stepper motor ST4209L1704, the setup in Table 3.6 is applied. An even periodicity is applied with rotation on the z-axis. A cyclic boundary condition is applied automatically with periodicity. A tangent magnetic field symmetry is applied in the XY plane. Also, a cylindrical infinite box is shown in Fig. 3.20 is applied.

Table 3.6: 3D model setup.

Model setup	
Periodicity	Even (cyclic boundary condition)
Symmetry	Tangent magnetic fields
Infinite box	Applied cylindrical
Non-meshed coils	Applied
Magnet orientation	axial z direction
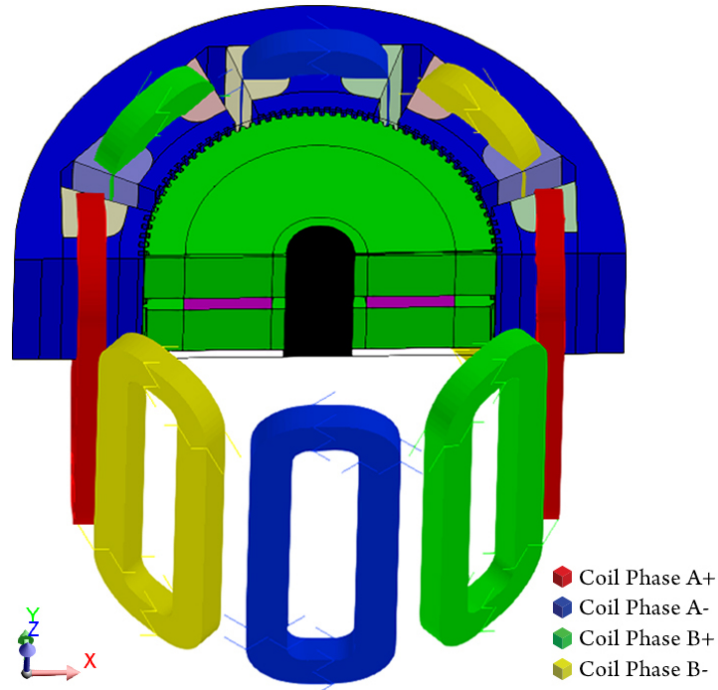
Figure 3.21: 3D model non-meshed coil.

The non-meshed coils are also modeled with respect to the whole motor shown in Fig. 3.21. Here, the red and blue coils are connected in series to represent phase A, and green and yellow are connected to represent phase B. The pink part in between the two lamination stacks is the magnet that is oriented in the axial direction. With the structure comparison in 2D FEA section 3.5.4, the 3D model will also include the stator bridge and rotor teeth fillets.

3.6.3 Meshing

While computation is highly dependent on the number of mesh nodes, the number of mesh nodes has to be optimized for both speed and accuracy. Automatic and manual mesh generation are compared as shown in Table 3.7. The comparison is also shown in Fig. 3.22.

Table 3.7: Mesh Comparison.

Model setup	Automatic	Manual
Air gap mesh node length	0.025 mm	0.075 mm
Number of nodes	1306998	2054602
Volume elements	6785552	10171645
Speed	~ 1Days	~ 2Days
Detent Torque	1.1×10^{-2}Nm	3.75×10^{-3}Nm
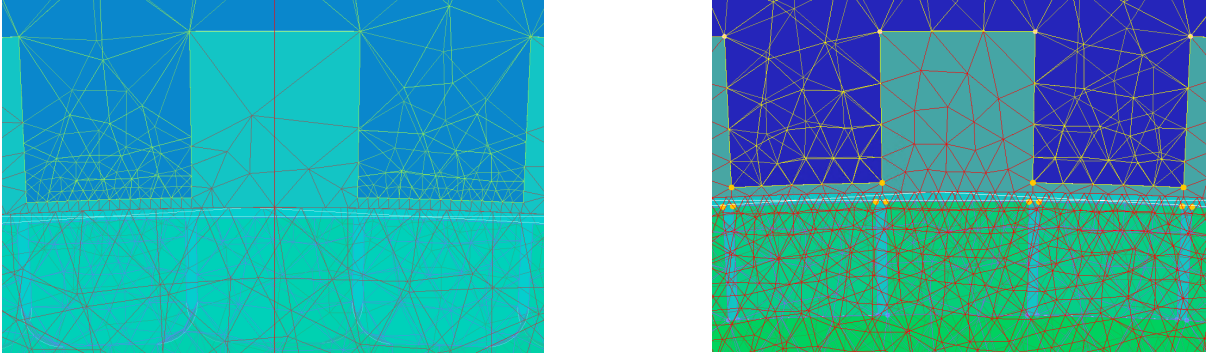
Figure 3.22: Mesh comparison (left) manual (right) automatic.

As seen in Fig. 3.22, the manual mesh air gap node length larger than the 0.05 mm air gap. The automatic mesh air gap node length, on the other hand, is half the air gap length. Comparing the detent torque measured and the datasheet shown in Table 3.1, it is clear that the manual mesh is 28% of the datasheet 0.0132Nm detent torque, while the automatic mesh is about 90% of the detent torque. Comparing the two waveforms from Fig. 3.23, detent torque harmonics are present in the automatic mesh generation. With the higher computation time and lower accuracy, manual mesh generation does not show a clear harmonics distribution. This can be caused by the lack of meshing nodes in the air gap. Fewer nodes in the air gap reduce the number of changes numerically calculated.
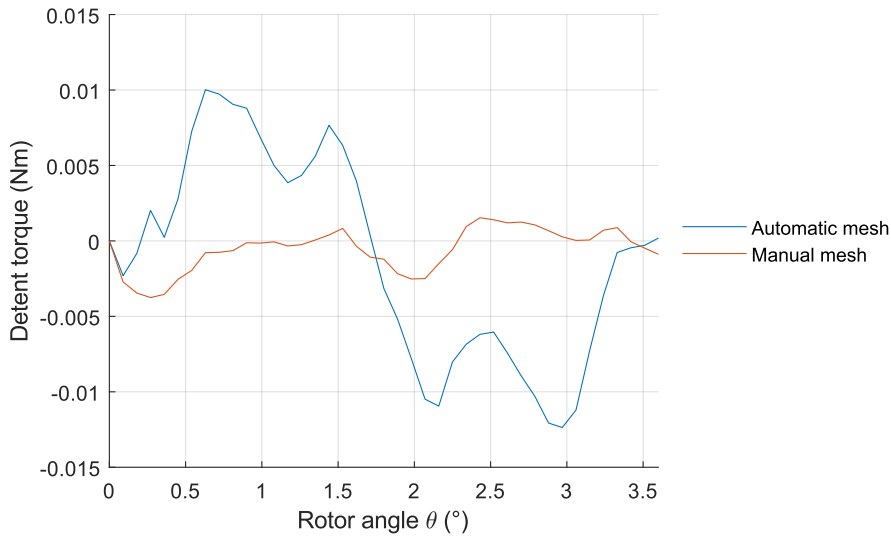
Figure 3.23: Detent torque vs. mesh size comparison.

To increase the manual mesh accuracy, a finer air gap mesh has to be constructed. However, a 0.25 mm node length in the air gap will not run on the current computer hardware provided for this thesis. Therefore, for speed and relative accuracy, the automatic mesh is applied instead.

3.6.4 Results and Validation

Validation of the FEA model is done by comparing the simulation results to the datasheet provided in Table 3.1. The detent torque, holding torque, back-emf and inductance are compared quantitatively. The holding torque-current curve is compared to qualitatively.

Detent Torque

The maximum detent torque of 0.0132Nm is provided by the manufacturer. However, waveform and harmonics are not specified. The torque simulated and estimated are shown in Fig. 3.24.
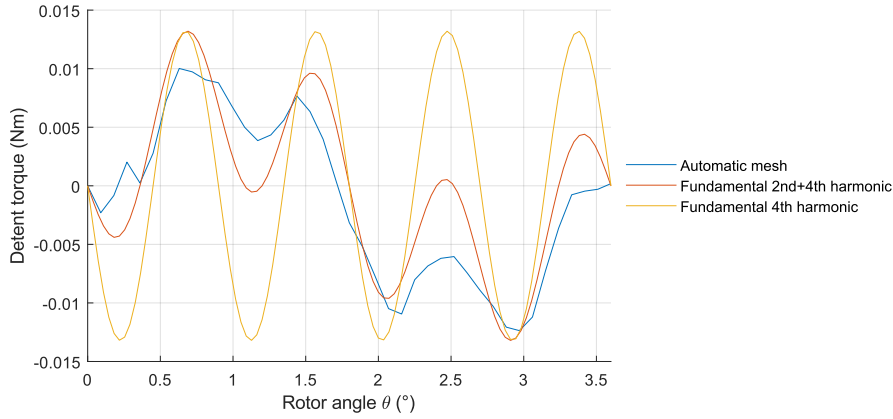
Figure 3.24: Detent Torque comparison.

The FEA maximum detent torque is calculated to be 0.0122Nm, 92% of the datasheet given detent torque. The datasheet detent torque is only 0.03% of the maximum holding torque, while the FEA maximum detent torque is 0.028% of the maximum holding torque. Therefore, the FEA model has a small error of 0.227% from the datasheet detent and holding torque ratio.

Noted in [28], 4th harmonic is dominant in the detent torque of an eight-pole, 1.8-degree stepper motor. Since the ST4209L1704 is also an eight-pole machine with a 0.9-degree step, the fundamental 4th harmonic curve (yellow) shown in Fig. 3.24 represents the original estimate of the detent torque. Yet, the FEA simulation shows a different waveform shown in Fig. 3.24. The FEA detent torque is dominated with 2nd and 4th harmonics with some higher harmonics parts. The higher harmonics and the 0th harmonic can be caused by the meshing inaccuracy since total torque in one electrical round (3.6° mechanical angle) should result in zero torque. The high dominance of 2nd harmonic is caused by the stator pole structure described in Section 3.2 and shown in Fig. 3.25. The unequal stator poles shown with black lines contribute to the 2nd harmonic in the detent torque.
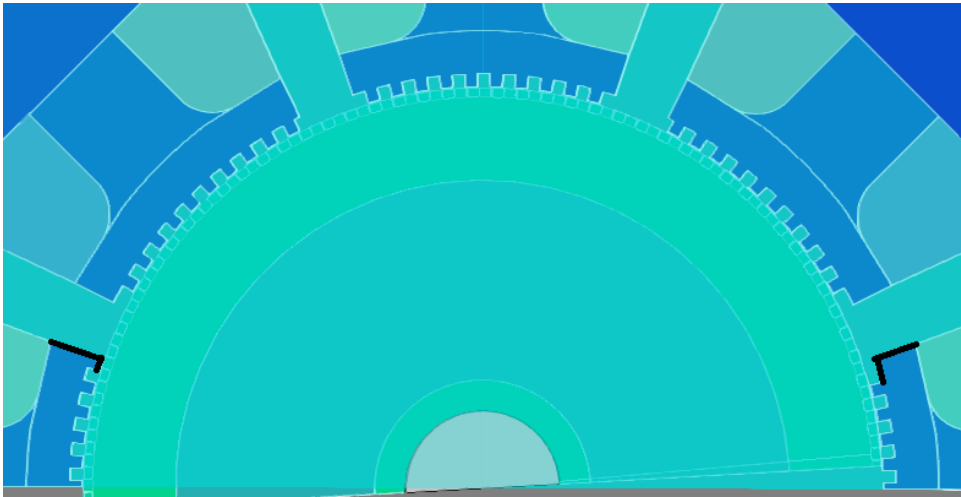
Figure 3.25: asymmetrical stator pole teeth (black lines).

Holding Torque

The FEA holding torque is validated with the datasheet where the peak holding torque is provided. Since the peak holding torque is dependent on the rotor position, the sinusoidal curve is fitted with the datasheet peak here. Holding torque is obtained by exciting the stepper motor under two-phase excited rated current. The outcome waveform is shown in Fig. 3.26.
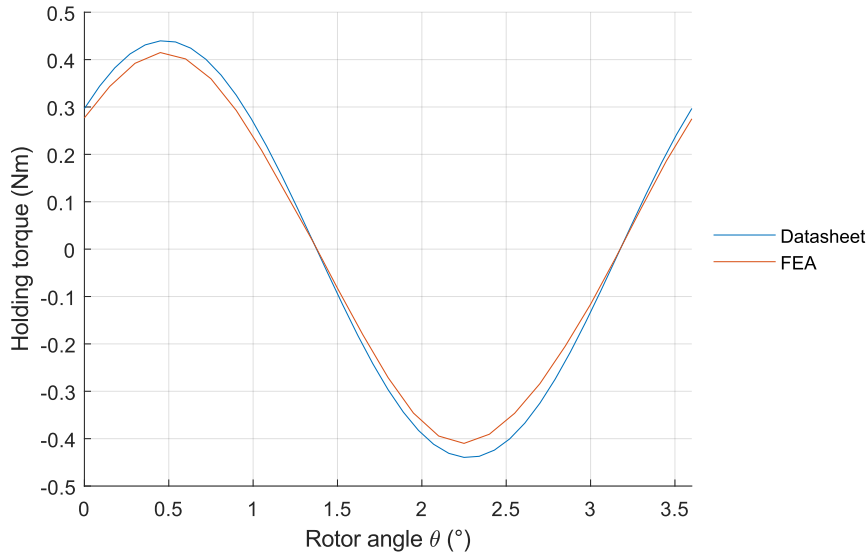
Figure 3.26: Holding torque comparison.

The maximum holding torque is measured to be 0.4032Nm. That is 91.4% of the datasheet maximum holding torque. Since holding torque is a function of current and flux shown in Section 4.3, with the same rated current, lower holding torque translates to a lower effective flux linkage that produces less torque. Lower effective flux can be caused by the lack of meshing elements in the air gap, different lamination silicon steel property, or the actual air gap length present in the model. Another silicon steel, Cogent M140-35S with higher average permeability of 32.71e3 is also applied to verify a possible lower torque caused by the silicon steel material. The comparison of the two materials is shown in Fig. 3.27.
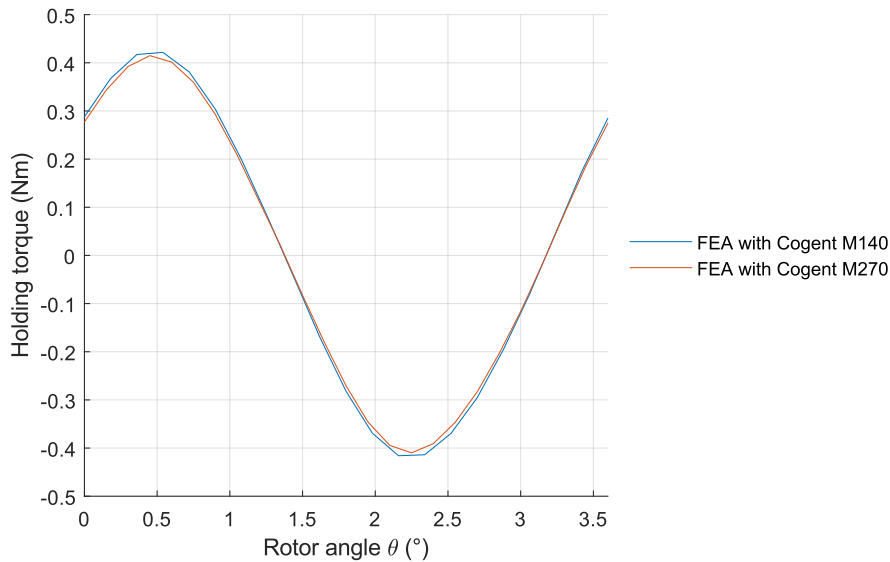
Figure 3.27: Silicon steel holding torque comparison.

As seen in the figure, with 0.0136Nm extra holding torque in the M140 silicon steel, the higher average permeability proves to increase the peak holding torque by 3%. However, because of the higher saturation in the B-H curve in the M140 material, solving time increased by twice the amount of that of M270 silicon steel. Therefore, such change proves that silicon steel can cause a lower torque. Yet, because of the higher solving time, the M270 is still used further. The error is therefore most possibly caused by the air gap length and number of meshing elements. Since the error is within expectation and the computation

power is not enough to calculate a higher number of meshing elements in this thesis, the model holding torque is validated with the datasheet specification.

Holding Torque-Current Curve

Although holding torque versus current curve is not provided in the datasheet, it is a good indicator to understand the flux saturation caused by the B-H in the motor. Since torque is related to the current level applied, it is an important indicator of the material property under certain flux linkages induced by the current. As seen in the figure, when rated 1.68 Amp is applied, the two curves are still considered within the linear region. This indicates that the silicon steel B-H curve applied is within the limit of the motor. Nonetheless, the torque slope linear estimation from 0 to 1.68Amps is 0.17 Nm/Amp whereas the motor parameter from the datasheet is calculated to be 0.185Nm/Amp.
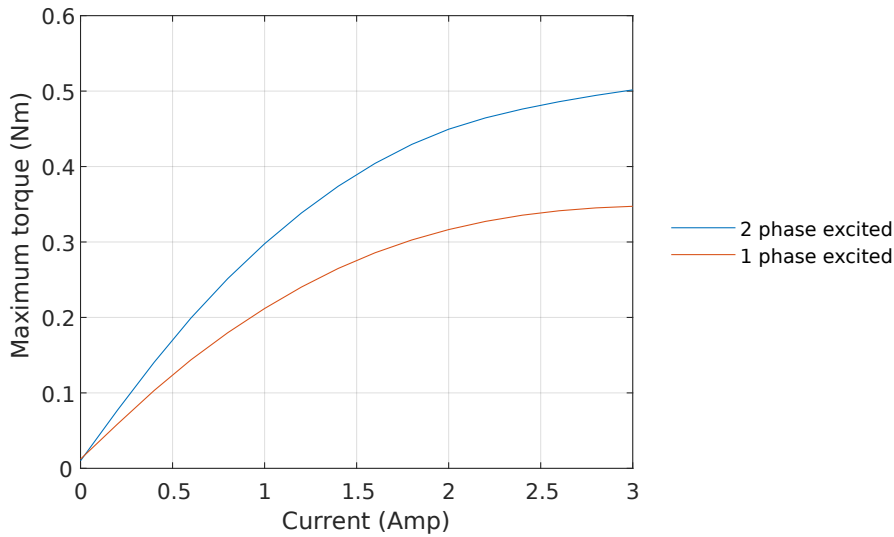
Figure 3.28: Holding torque vs. current curve.

Fig. 3.28 shows a clear view of the initial linear torque current relation that can also be represented as the torque constant.

Back-emf

While back-emf is a function of flux from the magnet, it is also validated with the datasheet under the same condition of no current at 300rpm. A time-varying magnet flux induces a voltage in the coil of the motor. The back-emf curve from the FEA and the sinusoidal back-emf curve built from the datasheet peak value are shown in Fig. 3.29
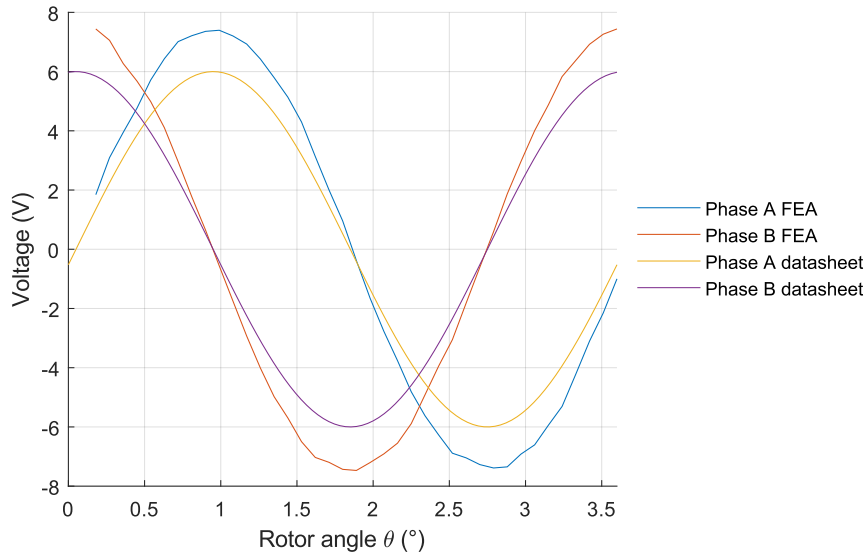
Figure 3.29: Motor back-emf curves.

Shown in Fig. 3.29, the back-emf of both phases have similar waveforms with 90° shift. Since the coils are positioned mechanical angle 90° apart, this fits the physical motor back-emf waveform.

However, the back-emf is only 75% of the datasheet. This is caused by the difference between the FEA model and physical coils. The FEA non-meshed coils have dimensions measured by the estimated area. Therefore, the induced current can be fluctuating. Back-emf is created by the magnetic circuit and only has a direct effect on the electrical circuit. The back-emf is later included in the MATLAB/Simulink model as a sinusoidal waveform.

Inductance

The motor inductance is also numerically solved in the FEA model by dividing the flux by the relative coil currents. Four inductances from the four coils in Fig. 3.21 are measured. since phase A+ and A- are connected in series, phase A inductance is summed up. Same to phase B. The phase inductance is solved by applying rated current to the testing phase and set the other phase current to zero. The measured inductance for both phases is shown in Fig. 3.30. The mean inductance of both phases is calculated to be 7.6mH instead of 5mH given in the motor parameter.
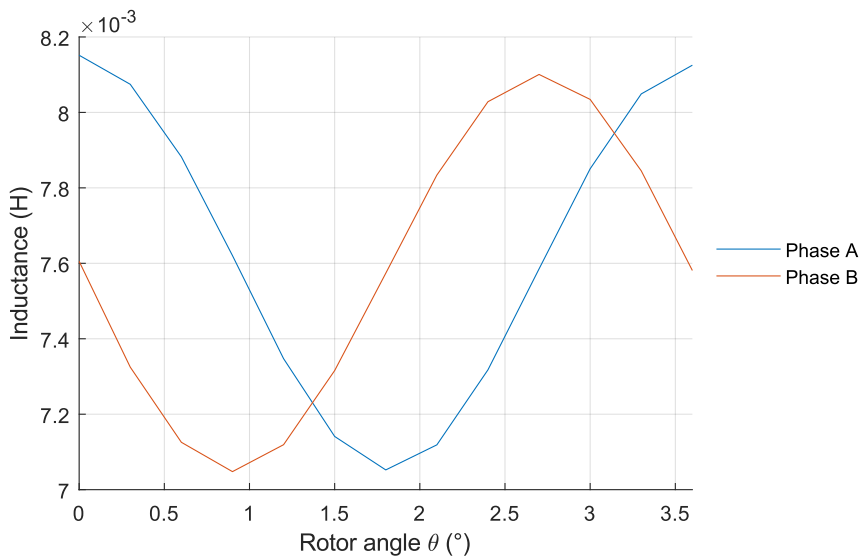
Figure 3.30: FEA model phase inductance.

Inductance can be calculated from the coil area, permeability, number of turns, and air gap length. Since the number of turns is counted from the physical motor, the inductance difference is caused by the coil area, lamination permeability, and air gap length. Different coil areas are tested with maximum and minimum coil area measurements. Yet, such changes dedicated to less inductance change than that of the permeability of silicon steel. By changing the motor lamination material to a higher relative permeability silicon steel M140, the mean inductance became 6.8mH from 7.6mH of the M270 silicon steel. The other cause of the inductance inaccuracy can be caused by the air gap length. Since the air gap is measured by subtracting the rotor maximum diameter from the stator minimum diameter, there is a much higher tolerance from the measurement.

Since the M140 silicon steel has a faster saturation, the simulation time is increased by almost two times. To reduce the air gap, the length of each meshing element has to be reduced. The total amount of meshing element, therefore, has to be increased causing the air gap is still applied with 0.05mm.

3.6.5   Summary

With the four specifications from the datasheet, the torque LUT built from the FEA model has a 91% accuracy considering the tolerances in structure and material. The error in inductance is most likely caused by the lamination material and air gap length from the physical dimension measuring tolerances. Different materials and air gap lengths were tested to better fit the datasheet parameters. Yet, they are not used in the final simulation because of the much higher computation time. The flux LUT is built from the FEA model further.

Chapter 4

Dynamic modeling

To fully represent a physical two-phase bipolar hybrid stepper motor, a semi-analytical model is built with the analytical modeling method on the MATLAB/Simulink environment. The generalized electrical equations are first discussed. Electrical and magnetic phenomenon dependencies are further developed. In this section, the equations are separated into the three main parts of:

- Electrical equations:
  The set of equations that defines the electrical and magnetic phenomenon of a two-phase bipolar hybrid stepper motor. The electrical circuit and magnetic flux linkages are derived from the electrical circuit and the magnetic coupling field between the motor coil and motor core. Non-linear entities are identified. A possible analytical representation for the non-linear entities is implemented in the module.

- Torque equations:
  The set of equations that represents the torque produced by the two-phase bipolar hybrid stepper motor. The energy conservation of the coupling field is applied.

- Mechanical equations:
  The set of mechanical phenomenon representation of the physical motor. The motor physical parameters such as rotor inertia and mechanical friction are implemented. Equations developed by co-energy is presented.

4.1 Electrical equations

The electrical equations are constructed based on the electric circuitry in the motor phases. The simplified electrical equivalent circuit of a hybrid stepper motor is represented with the fundamental winding circuit shown in Fig. 4.1. Such a figure shows the schematic of a basic hybrid stepper motor circuitry that assumes static parameters in coil resistant, coil phase inductance, and induced voltage from the magnet. Here the simplified circuitry equations without dynamic inductance and non-linear entities are first to be discussed.
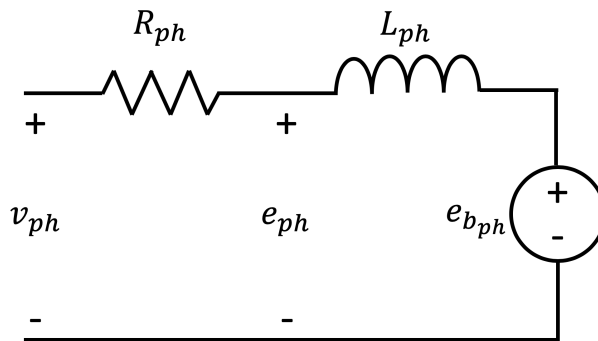
Figure 4.1: Electrical equivalent circuit.

The electric dynamics in the circuitry are mathematically described as

$$v_{ph} = R_{ph}i_{ph} + e_{ph}, \tag{4.1}$$

with v_{ph} being the input phase voltage, R_{ph} the phase resistance, i_{ph} the phase current, and e_{ph} the induced voltage. Since the induced voltage is created by both the inductance and back-emf, the induced voltage can be further expressed by

$$e_{ph} = L_{ph}\frac{di_{ph}}{dt} + e_{b_{ph}}, \tag{4.2}$$

where L_{ph} is the phase inductance and $e_{b_{ph}}$ the phase back-emf. By combining both (4.1) and (4.2), the fundamental electrical equivalent circuit is expressed as

$$v_{ph} = R_{ph}i_{ph} + L_{ph}\frac{di_{ph}}{dt} + e_{b_{ph}}. \tag{4.3}$$

The circuitry represents a single phase of a two-phase motor. A typical two-phase stepper motor with two parallel phase equations includes two parallel circuits. Nonetheless, according to Faraday's law of induction, the induced voltage is dependent on the change in magnetic flux as

$$e_{ph} = \frac{d\psi_{ph}}{dt}, \tag{4.4}$$

where ψ_{ph} is the flux linkage present in the motor. By equating (4.1), (4.2), and (4.4), the fundamental single-phase dynamics are defined as

$$v_{ph} = R_{ph}i_{ph} + \frac{d\psi_{ph}}{dt}, \tag{4.5}$$

where

$$\frac{d\psi_{ph}}{dt} = L_{ph}\frac{di_{ph}}{dt} + e_{b_{ph}}. \tag{4.6}$$

These general equations are used in several articles for stepper motor modeling, among VR, PM, and Hybrid stepper motors [2, 29, 30].

4.1.1 Electrical linearized equations

With the general equations defined, linearization of the parameters is often applied to simplify the equations further [2, 31]. The general equations are simplified from (4.3), where $e_{b_{ph}}$ is the only magnetic flux dependent parameter in the equation that needs to be further simplified. According to (4.4), the magnet induced voltage can also be expressed as

$$e_{b_{ph}} = \frac{d\psi_{mag}}{dt}, \tag{4.7}$$

where ψ_{mag} is the magnetic flux linkage produced by the magnet. The magnetic flux density strength is represented by a two-phase hybrid stepper motor with a 1.8-degree step size in Fig. 4.2. Note the N_r in a 1.8-degree stepper motor is 50.
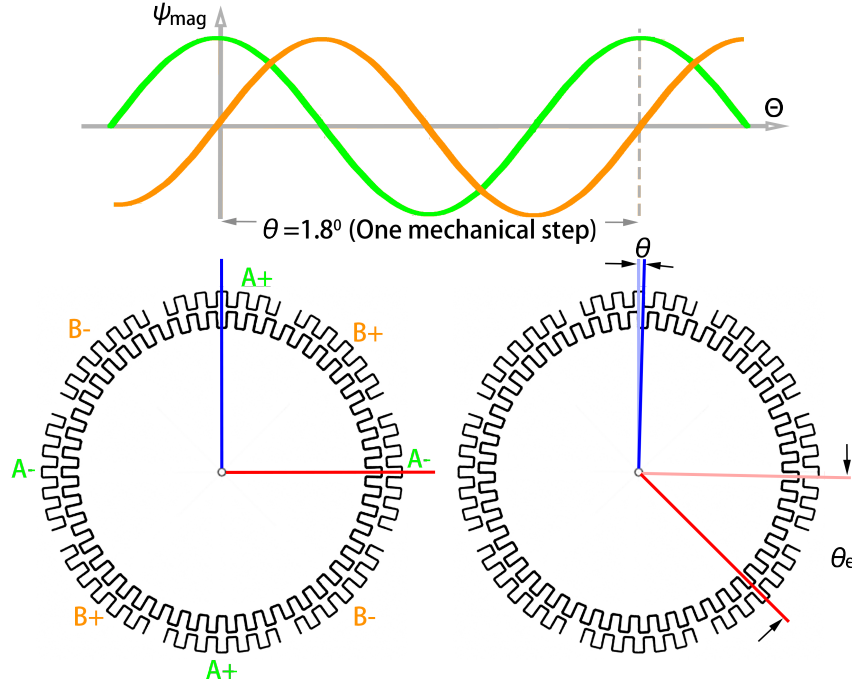
Figure 4.2: Magnet magnetic flux strength position dependency.

The red and blue positions on the motor indicates the rotation position of the stepper motor. Here, the blue rotation represents the mechanical degree θ and red rotation represents the electrical degree θ_e. The relation between an electrical and mechanical degree in a two-phase hybrid stepper motor is also known as

$$\theta_e = N_r \cdot \theta. \tag{4.8}$$

With the rotation, position change also affects the flux path. The flux in Fig. 4.2 can be estimated to follow the sinusoidal wave when flux fluctuates between the smallest and highest total air gap in each phase. Here, the rotor rotates a 90° electrical angle (θ_e), or 1.8° mechanical angle (θ). With such position change, phase A (green) follows a negative cosine wave and has the lowest flux linkage when the rotor is aligned with the A+ stator pole. Similarly, phase B (orange) follows a negative sine wave and has the highest flux linkage when the rotor is aligned with the B+ stator pole. Such sinusoidal wave can then be directly implemented into the induced voltage equation as

$$e_{b_A} = \frac{d}{dt} \psi_{M,mag} \cos(N_r\theta), \tag{4.9}$$

$$e_{b_B} = \frac{d}{dt} \psi_{M,mag} \sin(N_r\theta) = \frac{d}{dt} \psi_{M,mag} \cos(N_r\theta - \frac{\pi}{2}), \tag{4.10}$$

where $\psi_{M,mag}$ is the maximum magnetic flux density provided by the magnet. The equations can be further derived as

$$e_{b_A} = -N_r \psi_{M,mag} \omega \sin(N_r\theta), \tag{4.11}$$

$$e_{b_B} = -N_r \psi_{M,mag} \omega \sin(N_r\theta - \frac{\pi}{2}), \tag{4.12}$$

where ω, angular speed, is the representation of $\frac{d\theta}{dt}$, change in angle with time. Phase A and B induced voltages are being equated to the product of the number of rotor teeth, maximum magnet flux density, motor speed, and angle position. The first three products without the sinusoidal segment indicate that the maximum induced voltage is dependent on the speed of ω, and each rotor teeth commits to a small part of the total induced voltage. The sinusoidal segment represents the change in induced voltage on each wire.

Finally, combining with (4.11) and (4.12), (4.3) can be further simplified with phase A and B as

$$v_A = Ri_A + L\frac{di_A}{dt} - N_r\psi_{M,mag}\omega\sin(N_r\theta), \tag{4.13}$$

$$v_B = Ri_B + L\frac{di_B}{dt} - N_r\psi_{M,mag}\omega\sin(N_r\theta - \frac{\pi}{2}), \tag{4.14}$$

where R_A and R_B are replaced by R, and L_A and L_B replaced by L in an ideal motor. Under ideal motor, coils of both phases can be assumed to be the same because all phases should have the same wire properties and coil turn counts. Nonetheless, the motor is assumed to be perfectly symmetrical without any imperfection. Therefore, static resistance and inductance can be used for both phases.

4.1.2 Electrical non-linear parameter dependencies

However, more than often, motor equation parameters are not fully linear and are dependent on other parameters. To further analyze the electrical dynamics, it is therefore important to locate the non-linear parameter dependencies.

Mutual Inductance

Other than single-phase activate mode on the stepper motor, mutual inductance is also present. This is because of the common stator and rotor lamination the phase coils are positioned in. Mutual inductance is an effect where the current change in one coil induced a voltage to the other coil described by Faraday's Law. Nonetheless, the induced voltage direction in one coil will always oppose to the magnetic field produced by the other coil. Such a phenomenon can be derived directly from Lenz's law. Therefore, the two mutual inductance often degrade the accuracy of the stepper positioning [8]. While mutual inductance is present in a two-phase VR stepper motor between the two phases, mutual inductance in a hybrid stepper motor includes both the interaction between two phases and interaction between phases and the magnet [32]. Therefore, phase inductances L_A and L_B from the two phases can be combined into

$$\begin{bmatrix} L_{AA} & M_{AB} & M_{Am} \\ M_{AB} & L_{BB} & M_{Bm} \\ M_{Am} & M_{Bm} & L_{mm} \end{bmatrix}, \tag{4.15}$$

with L_{AA} being the self-inductance of phase A, M_{AB} the mutual inductance between phases A and B, L_{BB} the self-inductance of phase B, M_{Am} the mutual inductance between phases A and magnet, M_{Bm} the mutual inductance between phases B and magnet, and L_{mm} the self-inductance of the magnet. Since magnet contains remanence residual magnetic flux density, the magnet inductance is defined by the general inductance-flux relation equation

$$L = \frac{\Psi}{i}, \tag{4.16}$$

where Ψ is the flux, which in this case represents the magnet residual magnetic flux density, and i is the current applied, which in this case is the imaginary electric current in the magnet. Since magnet does not consist of electrical current, magnet inductance is therefore also an imaginary parameter that is created to directly relate the flux to a coil parameter. Although magnet inductance is created in (4.15), such implementation will however require the creation of an imaginary magnet current. Because of that, the magnet inductance affecting e_{b_A} and e_{b_B} is decoupled and later discussed under magnet analysis in Subsection 4.1.2. Therefore, 4.15 is reduced to only inductance interaction between coils as

$$\begin{bmatrix} L_{AA} & M_{AB} \\ M_{AB} & L_{BB} \end{bmatrix}. \tag{4.17}$$

The induced voltage expression created by the coils shown in the first term of (4.2) can then be expended for both phases as a matrix equation

$$\begin{bmatrix} e_A \\ e_B \end{bmatrix} = \frac{d}{dt}\left(\begin{bmatrix} L_{AA} & M_{AB} \\ M_{AB} & L_{BB} \end{bmatrix} \cdot \begin{bmatrix} i_A \\ i_B \end{bmatrix}\right) + \begin{bmatrix} e_{b_A} \\ e_{b_B} \end{bmatrix}, \tag{4.18}$$

where the mutual inductance interaction is included in the hybrid stepper motor inductance equation.

Inductance position dependency

An important aspect of a hybrid stepper motor is that it contains both the benefits of permanent magnet and variable reluctance. Flux is created by both the permanent magnet and coil current and passed through the small rotor teeth saliency. Consequently, the rotor teeth saliency creates an entity of changing inductance with the position. Therefore, both the mutual and self-inductance in the motor are dependent on the position angle of the motor. With such dependency, inductance variables in (4.18) can be expressed as

$$
\begin{bmatrix} e_A \\ e_B \end{bmatrix} = \frac{d}{dt} \left(\begin{bmatrix} L_{AA}(\theta) & M_{AB}(\theta) \\ M_{AB}(\theta) & L_{BB}(\theta) \end{bmatrix} \cdot \begin{bmatrix} i_A \\ i_B \end{bmatrix} \right) + \begin{bmatrix} e_{b_A} \\ e_{b_B} \end{bmatrix},
\tag{4.19}
$$

Continuing with mutual inductance in Subsection 4.1.2, the inductance position dependency is analyzed by decoupling the magnet. The inductance of phase A and B, L_A and L_B can be expressed as

$$
L_{AA}(\theta) = L_{A0} + L_{A1}(\theta),
\tag{4.20}
$$

$$
L_{BB}(\theta) = L_{B0} + L_{B1}(\theta),
\tag{4.21}
$$

where L_{A0} and L_{B0} are the base inductance ,and L_{A1} and L_{B1} the position dependent inductance. By combining (4.17), (4.20), and (4.21), the inductance matrix can be further expressed as

$$
\begin{bmatrix} L_A(\theta) \\ L_B(\theta) \end{bmatrix} = \begin{bmatrix} L_{A0} + L_{A1}(\theta) & M(\theta) \\ M(\theta) & L_{B0} + L_{B1}(\theta) \end{bmatrix},
\tag{4.22}
$$

where L_A and L_B are phase inductances. M is further used to represent M_{AB} to simplify the subscript. Both mutual and self-inductance are position-dependent. To produce a universal torque on both phases, number of turns on the coils on both phases are always the same. Therefore, fundamental and none position-dependent inductances, L_{A0} and L_{B0}, are to be the same for both phases in the stepper motor. The equation can be further defined as

$$
\begin{bmatrix} L_A(\theta) \\ L_B(\theta) \end{bmatrix} = L_0 \begin{bmatrix} 1 & 0 \\ 0 & 1 \end{bmatrix} + \begin{bmatrix} L_{A1}(\theta) & M(\theta) \\ M(\theta) & L_{B1}(\theta) \end{bmatrix}.
\tag{4.23}
$$

With the inductance dependency with rotor angle position, relative sinusoidal changes in inductance can also be developed further. To further investigate, the physical design of the hybrid stepper motor in Section 3.1 can be mathematically simplified to a fundamental two-phase stepper motor shown in Fig. 4.3.
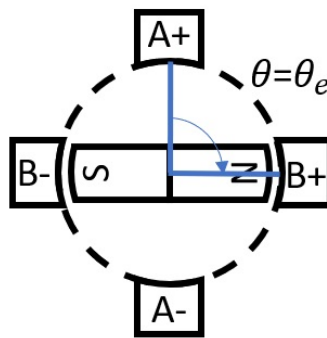
Figure 4.3: 2-phase motor with equal mechanical and electrical angle

Such simplification reduces the complexity by equating the mechanical angle (θ) to the electrical angle (θ_e). Both angles are 90° in this case. The inductance change can be further illustrated in Fig. 4.4.
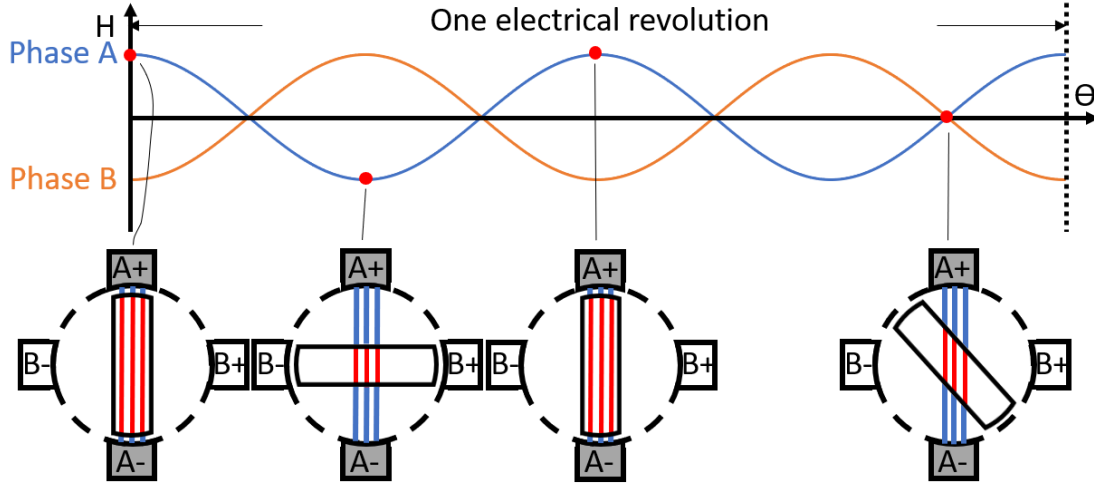
Figure 4.4: Position dependent inductance L_1

Illustrated for the phase A flux linkage, the four rotor positions in an excited motor shown in Fig. 4.4 represent the flux paths and relative air gap changes. Such changes are then translated to the position dependence inductance L_{A1} shown in the waveform. The phase A air gap increases as the rotor rotates from 0° to 90° and 180° to 270°. When phase A stator teeth are aligned with the rotor teeth, the smallest air gap is present. Consequently, the largest air gap is present in such a condition. Such rotation translates to two sinusoidal waves half a revolution apart [5, 33]. The position-dependent inductance for both phases can be sinusoidally expressed as

$$L_{A1}(\theta) = L_1 \cos(2Nr\theta), \tag{4.24}$$
$$L_{B1}(\theta) = -L_1 \cos(2Nr\theta), \tag{4.25}$$

where L_1 is the magnitude of position-dependent phase inductance. While the two phases are identical to each other electrically and both in the geometry and coil turns, both phases have the same maximum inductance magnitude. Such sinusoidal position dependence inductance can be validated with the FEA result shown in Fig. 4.5. The highly fluctuating inductance computed from 0° to 0.5° can be caused by the static FEA calculation incorrect initial condition.
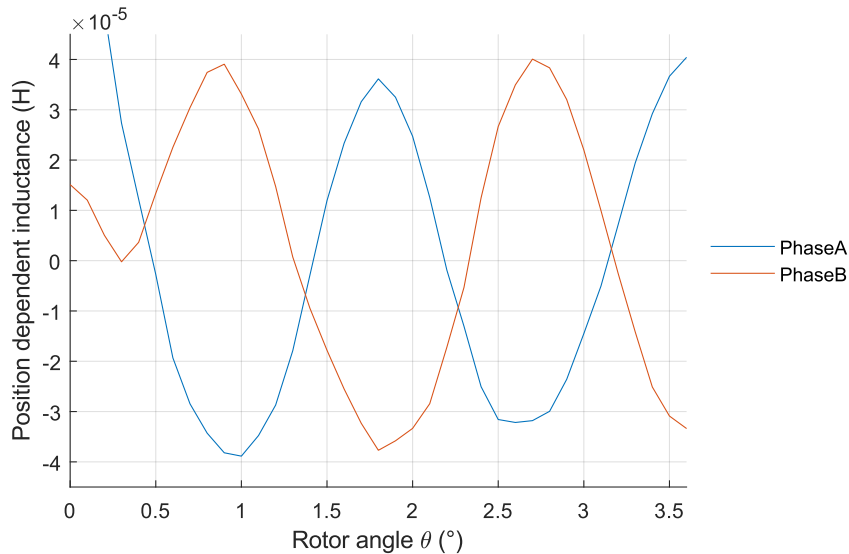
Figure 4.5: Position dependent inductance from FEA computation

Similarly, the mutual inductance position dependency can also be expressed sinusoidally. Since the interaction of two phases is at its maximum when stator teeth are aligned in between two phases, the

sinusoidal waveform for both phases shown in Fig. 4.4 are then shifted by half a step (90° in the case of Fig. 4.4). Such shift results in the position-dependent mutual inductance as

$$M(\theta) = M \sin(2N_r\theta). \tag{4.26}$$

Such position-dependent mutual inductance can also be validated from the FEA model as shown in Fig. 4.6.
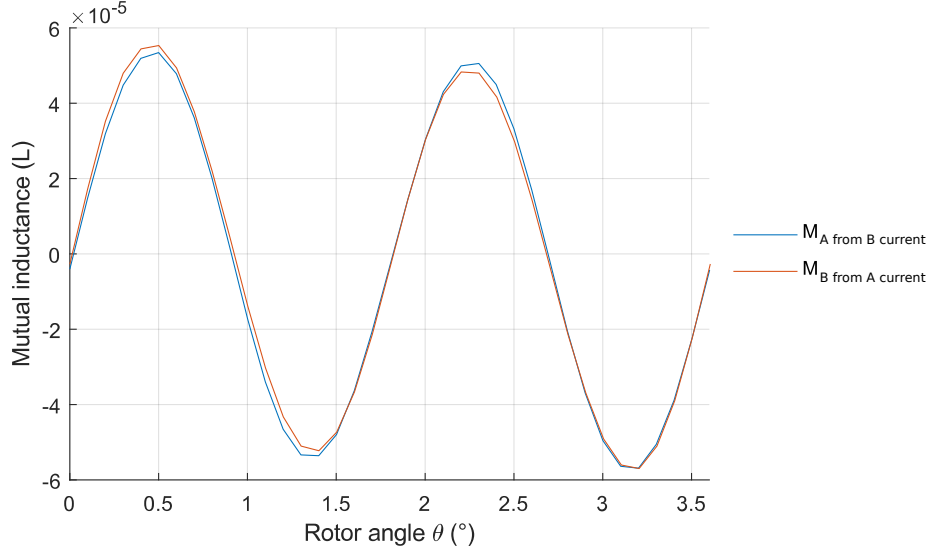
Figure 4.6: Position dependent mutual inductance from FEA computation

By combining (4.23), (4.24), (4.25), and (4.26), the position dependent mutual and self-inductances can be shown as

$$\begin{bmatrix} L_A(\theta) \\ L_B(\theta) \end{bmatrix} = L_0 \begin{bmatrix} 1 & 0 \\ 0 & 1 \end{bmatrix} + \begin{bmatrix} L_1 \cos(2Nr\theta) & M \sin(2N_r\theta) \\ M \sin(2N_r\theta) & -L_1 \cos(2Nr\theta) \end{bmatrix}. \tag{4.27}$$

Magnet position dependency

Since the magnet flux also experiences the position-dependent saliency in the motor, induced voltage equation can be further expressed as

$$\begin{bmatrix} e_A \\ e_B \end{bmatrix} = \frac{d}{dt} \left(\begin{bmatrix} L_{AA}(\theta) & M_{AB}(\theta) \\ M_{AB}(\theta) & L_{BB}(\theta) \end{bmatrix} \cdot \begin{bmatrix} i_A \\ i_B \end{bmatrix} \right) + \begin{bmatrix} e_{b_A}(\theta) \\ e_{b_B}(\theta) \end{bmatrix}, \tag{4.28}$$

Here, the e_{b_A} and e_{b_B} are directly affected by the magnet inductances in (4.15), where the magnet mutual and self-inductance are parts of the inductance matrix. While magnet inductances are periodic functions because of the repeating rotor teeth and stator teeth alignment positions. The mutual and self-inductance of the magnet and both phases can be denoted with fundamental wave equation presented in [32] as

$$M_{Am} = M_{Am0} + \sum_{j=1}^{n} M_{Am1_n} \cos(nN_r\theta), \tag{4.29}$$

$$M_{Bm} = M_{Bm0} + \sum_{j=1}^{n} M_{Bm1_n} \sin(nN_r\theta), \tag{4.30}$$

$$L_{mm} = L_{mm0} + \sum_{j=4}^{n} L_{mm1_n} \cos(nN_r\theta), \tag{4.31}$$

where M_{Am0}, M_{Bm0}, and L_{mm0} are the fundamental constant part of M_{Am}, M_{Bm}, and L_{mm}. The M_{Am1_n}, M_{Bm1_n}, and L_{mm1_n} are the amplitudes of each higher harmonics in M_{Am}, M_{Bm}, and L_{mm}.

Nonetheless, j is the fundamental harmonic term and n is the higher-order harmonic terms. The n terms are used to model the non-sinusoidal harmonics of the mutual inductance [32]. Although the higher harmonic dependencies can be represented with the summing term from (4.29), (4.30), and (4.31), the defining variables in the higher orders are often curve fitted to the measurement from the physical model [33]. These variables are often dependent on physical motor imperfections. Therefore, without taking the higher harmonics of the magnet-coil mutual inductance into account, the parameters and higher terms in a stepper motor model is set to be

$$\begin{cases} M_{Am1_n} = 0, & j \geq 2, \\ M_{Bm1_n} = 0, & j \geq 2, \\ L_{mm1_n} = 0, & j \geq 5, \end{cases} \tag{4.32}$$

such that higher harmonics of mutual inductance are ignored. However, the magnet higher harmonic terms of the magnet self-inductance should not be ignored because of the detent torque production from self-inductance discussed in Subsection 3.6.4. Therefore (4.29), (4.30), and (4.31) can be expressed further as

$$M_{Am} = M_{Am0} + M_{Am1_n} \cos(N_r\theta), \tag{4.33}$$

$$M_{Bm} = M_{Bm0} + M_{Bm1_n} \sin(N_r\theta), \tag{4.34}$$

$$L_{mm} = L_{mm0} + \sum_{j=4}^{n} L_{mm1_n} \cos(nN_r\theta). \tag{4.35}$$

By applying (4.16) and the imaginary magnet current, the magnetic flux of phases A and B can be obtained. The magnet self-inductance equation is ignored here since it creates no electrical circuit significance. The magnet flux equation can then be equated to

$$\psi_{Am} = i_{Am}M_{Am0} + i_{Am}M_{Am1}\cos(N_r\theta)) = \psi_{Am0} + \psi_{Am1}\cos(N_r\theta)), \tag{4.36}$$

$$\psi_{Bm} = i_{Bm}M_{Bm0} + i_{Bm}M_{Bm1}\sin(N_r\theta)) = \psi_{Bm0} + \psi_{Bm1}\sin(N_r\theta)), \tag{4.37}$$

where i_{Am} and i_{Bm} are the imaginary magnet current, ψ_{Am0} and ψ_{Bm0} the constant term of the magnet flux, and ψ_{Am1} and ψ_{Bm1} the changing part of the magnet flux. By comparing (4.9) and (4.10) to (4.36) and (4.37), the change in magnet flux is indeed the same as the linearized equation. The $\psi_{M,mag}$ is indeed the ψ_{Am1} and ψ_{Bm1}. The ψ_{Am0} and ψ_{Bm0} are not taken into account in Subsection 4.1.1 because induced voltage is created only by the change in magnet flux. The e_{b_A} and e_{b_B} in (4.18) can be expressed as

$$\begin{bmatrix} e_{b_A}(\theta) \\ e_{b_B}(\theta) \end{bmatrix} = \frac{d}{dt} \begin{bmatrix} \psi_{Am0} + \psi_{M,mag}\cos(N_r\theta)) \\ \psi_{Bm0} + \psi_{M,mag}\sin(N_r\theta)) \end{bmatrix}. \tag{4.38}$$

Current dependency

Current level dependency is also an effect that can occur in hybrid stepper motors. While flux linkage follows the path in the magnetic circuit, magnet, iron teeth, air gap, and iron cores, a non-linear relationship exists between the current level and flux magnitude. When flux paths through the materials, the permeability and B-H curve of such materials can limit the flux level [33]. Addition to the position dependency, current dependency has to be added to (4.28) as

$$\begin{bmatrix} e_A \\ e_B \end{bmatrix} = \frac{d}{dt} \left(\begin{bmatrix} L_{AA}(\theta,i) & M_{AB}(\theta,i) \\ M_{AB}(\theta,i) & L_{BB}(\theta,i) \end{bmatrix} \cdot \begin{bmatrix} i_A \\ i_B \end{bmatrix} \right) + \begin{bmatrix} e_{b_A}(\theta,i) \\ e_{b_B}(\theta,i) \end{bmatrix}, \tag{4.39}$$

Since both the inductance and magnet flux, which creates the induced voltage, are now current dependent, for each current magnitude, there is an operating point that creates the flux through the reluctance of the motor. The reluctance itself is also now dependent on the current. The best method to implement the current dependency is to create a matrix that directly translates the set-points of current and relative flux outcome. This method is implemented via the FEA simulation and lookup tables.

4.1.3   Semi-analytical electrical equations

With some of the non-linear parameters determined, the fundamental electrical equation (4.2) can be represented in two ways. First, a set of equations that includes the non-linear entities by estimating them mathematically. Such an equation will include parameters that include non-linear properties. By including the mutual inductance, inductance position dependency, and magnetic position dependency, the equation can be combined as

$$
\begin{bmatrix} v_A \\ v_B \end{bmatrix} = \begin{bmatrix} R_A i_A \\ R_B i_B \end{bmatrix} + \frac{d}{d\theta}\left(L_0 \begin{bmatrix} 1 & 0 \\ 0 & 1 \end{bmatrix} + \begin{bmatrix} L_1 \cos(2Nr\theta) & M\sin(2N_r\theta) \\ M\sin(2N_r\theta) & -L_1\cos(2Nr\theta) \end{bmatrix} \right) \omega \cdot \begin{bmatrix} i_A \\ i_B \end{bmatrix}
$$
$$
+ \left(L_0 \begin{bmatrix} 1 & 0 \\ 0 & 1 \end{bmatrix} + \begin{bmatrix} L_1 \cos(2Nr\theta) & M\sin(2N_r\theta) \\ M\sin(2N_r\theta) & -L_1\cos(2Nr\theta) \end{bmatrix} \right) \cdot \frac{d}{dt} \begin{bmatrix} i_A \\ i_B \end{bmatrix}
$$
$$
+ N_r \cdot \omega \cdot \psi_{M,mag} \begin{bmatrix} -\sin(N_r\theta) \\ \cos(N_r\theta) \end{bmatrix}. \tag{4.40}
$$

Another method to take into account the non-linear position and current entities is to directly obtain the flux linkage detail from the motor. Such a method directly inputs the flux at a different position under different current that the motor will experience during operation. This method is often applied with lookup tables (LUT) By coupling such data, the flux becomes a direct non-linear input as

$$
\begin{bmatrix} v_A \\ v_B \end{bmatrix} = \begin{bmatrix} R_A i_A \\ R_B i_B \end{bmatrix} + \frac{d}{dt} \begin{bmatrix} \psi_{LUTA}(i_A, i_B, \theta) \\ \psi_{LUTB}(i_A, i_B, \theta) \end{bmatrix}, \tag{4.41}
$$

where ψ_{LUTA} and ψ_{LUTB} are non-linear entities. The magnetic flux parameter can also be expressed by the current with non-linear dependencies as

$$
\begin{bmatrix} \psi_{LUTA}(i_A, i_B, \theta) \\ \psi_{LUTB}(i_A, i_B, \theta) \end{bmatrix} = \int \left(\begin{bmatrix} v_A \\ v_B \end{bmatrix} - \begin{bmatrix} R_A \cdot i_A(\psi_A, \psi_B, \theta) \\ R_B \cdot i_B(\psi_A, \psi_B, \theta) \end{bmatrix} \right), \tag{4.42}
$$

where currents i_A and i_B are dependent on ψ_A and ψ_B.

4.2   Torque equations

The production of torque by a two-phase hybrid stepper motor can be obtained by energy conservation where the total amount of energy in the system should add up to be zero.

4.2.1   Energy conservation

Treated as a system, two-phase hybrid stepper motor can be applied with energy conservation in all phases. Starting with the fundamental law of energy conservation shown below.

$$
\begin{pmatrix} Electrical \\ energy\ supplied \\ to\ the\ motor \end{pmatrix} = \begin{pmatrix} Mechanical \\ energy\ in\ the \\ moving\ motor \end{pmatrix} + \begin{pmatrix} Magnetic \\ energy\ reserved\ in \\ the\ coupling\ field \end{pmatrix}
$$

The energy conservation can then be described with differential equation as

$$
dW_e = dW_m + dW_f, \tag{4.43}
$$

with dW_e being the electrical energy supplied to the motor, dW_m the mechanical energy in the moving motor, and dW_f the magnetic energy reserved in the coupling field of the electrical system [8, 31].

Representing the electrical energy input in the system, the dW_e can be expressed as

$$
dW_e = (e_A i_A + e_B i_B)dt, \tag{4.44}
$$

where e_A and e_B are the electromotive force induced in phase A and B and i_A and i_B the current of phase A and B [31].

The mechanical energy is related to the torque as

$$
dW_m = (\tau_A + \tau_B)d\theta_m, \tag{4.45}
$$

where τ_A and τ_B are separated torque associated to phase A and B from the total torque [8].

The magnetic energy reserved in the coupled field can be derived from the combination of Faraday's law of induction shown in (4.4) and energy equation shown in (4.44) to form

$$dW_f = i_A d\psi_A + i_B d\psi_B, \tag{4.46}$$

where the total amount of energy stored in the coupling field over rotor angles is

$$W_f = \int_0^{\psi_A} i_A d\psi_A + \int_0^{\psi_A} i_B d\psi_B. \tag{4.47}$$

To find the relation between flux and torque, the motor is first blocked so that the motor is not moving. In such a condition, the change in angle $d\theta_m$ becomes zero. Hence, (4.44), (4.47), and (4.43) merges into

$$dW_e = dW_f = (e_A i_A + e_B i_B)dt = i_A d\psi_A + i_B d\psi_B, \tag{4.48}$$

where the electrical energy supplied is fully reserved in the coupling field. Acknowledging that the maximum energy supplied is equal to the maximum energy stored in the field, the motor is now able to rotate. By allowing the change in angle, (4.43) and (4.45) can be described as

$$i_A d\psi_A + i_B d\psi_B = dW_e = dW_f + (\tau_A + \tau_B)d\theta_m, \tag{4.49}$$

where the electrical energy supplied is represented in a magnetic energy form. By shifting the torque to the left, we obtain

$$(\tau_A + \tau_B) = \frac{i_A d\psi_A}{d\theta_m} + \frac{i_B d\psi_B}{d\theta_m} - \frac{dW_f}{d\theta_m}, \tag{4.50}$$

where

$$\frac{dW_f'}{d\theta_m} = \frac{i_A d\psi_A}{d\theta_m} + \frac{i_B d\psi_B}{d\theta_m} - \frac{dW_f}{d\theta_m}. \tag{4.51}$$

Here, the term W_f' is the co-energy in the motor. Such a term does not have a physical meaning but is used to represent the magnetic torque that is associated with the motor with respect to rotor displacement [8]. The total amount of co-energy can be expressed as

$$W_f' = \int_0^{i_A} \psi_A di_A + \int_0^{i_A} \psi_B di_B, \tag{4.52}$$

where the total co-energy is the integration of magnetic flux with respect to current. The fundamental equation to calculate the torque of a stepper motor then applies to all n phase coils in the motor [8]. Hence, the sum of torque may be written as

$$\tau_{total} = \frac{d}{d\theta_m} \sum_{ph=1}^{n} \int_0^{i_{ph}} \psi(\theta, i_{ph}) di_{ph}, \tag{4.53}$$

where the magnetic flux is also a function of position and current [8]. By inserting the magnetic flux expression derived previously in the fundamental electrical equations and Subsection 4.1.2, the flux linkages of phase A and B can be expressed as

$$\psi_A = L_A(\theta)i_A + \psi_{Am0} + \psi_{M,mag} \cos(N_r\theta), \tag{4.54}$$
$$\psi_B = L_B(\theta)i_B + \psi_{Am0} + \psi_{M,mag} \sin(N_r\theta), \tag{4.55}$$

where the $L_A(\theta)$ and $L_B(\theta)$ are the position-dependent phase inductances, including both mutual and self-dependence inductance. Substituting this into (4.53) we obtain

$$\tau_{total} = \left(\frac{1}{2}i_A^2 \frac{dL_A(\theta)}{d\theta} + \frac{1}{2}i_B^2 \frac{dL_B(\theta)}{d\theta} + i_A i_B \frac{dM(\theta)}{d\theta} \right)$$
$$+ \left(-N_r \psi_{M,mag} i_A \sin(N_r\theta) + N_r \psi_{M,mag} i_B \cos(N_r\theta) \right), \tag{4.56}$$

where the first term relates to the reluctance torque from the hybrid stepper motor and the second term related to the permanent magnet torque. Nonetheless, the reluctance torque is often ignored because of the small saliency in hybrid stepper motors [10]. While the permanent magnet term directly relates the magnet flux to torque, the multiplication factor in the term often refers to as the torque constant (K_t). The motor torque equation is often simplified into

$$\tau_{total} = -K_t i_A \sin(N_r\theta) + K_t i_B \cos(N_r\theta). \tag{4.57}$$

Yet, since hybrid stepper motors do experience a small amount of saturation shown in Subsection 3.6.4, Kt itself is not a linear but saturated curve that is affected by the B-H curve of the materials in the motor.

4.2.2 Detent torque

An additional torque from a hybrid stepper motor is the detent torque, or cogging torque. Since permanent magnet consists of the remanent flux, a detent torque is an inherent property in all PM motors [28]. The magnet will cause the motor to favor certain resting positions. This is caused by both the saliency and material B-H curve [28, 34]. Detent torque is created with relation to the magnet flux, such torque is therefore produced by the self-inductance of the magnet shown in (4.35) [32].

By revisiting (4.56), it is important to know that only the coil inductances were shown in the equation. However, just like the matrix in (4.15), magnet self-inductance also creates a torque, which is the detent torque, which is not dependent on the coil current. By taking the magnet self-inductance into account the detent torque can be expressed as

$$\tau_{detent} = \frac{1}{2} i_{mm}^2 \frac{dL_{mm}(\theta)}{d\theta}, \tag{4.58}$$

where the i_{mm} is the imaginary magnet current. By substituting (4.35) into (4.58), the detent torque yields to

$$\tau_{detent} = -\frac{1}{2} \sum_{j=4}^{n} i_{mm}^2 L_{mm1_n} n N_r \sin(n N_r \theta). \tag{4.59}$$

While it is known that detent torque has a fundamental fourth harmonic, diagonal asymmetry in the motor structure will also induce higher harmonics [28]. Nonetheless, lower harmonics can also be present with half structure asymmetries. Therefore, to obtain the detent torque accurately, the detent torque is often measured via experiments. Yet, to reduce the complexity from the higher harmonics and assume the motor is diagonally symmetrical, many have suggested to directly implement the fourth harmonics [10,31]. Such reduces the equation to

$$\tau_{detent} = -T_{dm} sin(4Nr\theta), \tag{4.60}$$

where T_{dm} is the detent torque amplitude constant that is often given by the manufacturer. However, to obtain more representative detent torque, it is still necessary to obtain the higher harmonics via other methods such as motor physical measurements.

4.3 Mechanical equation

With the torque produced by the electrical system equation of the motor, the electrical system is then coupled to the motor mechanical system that takes into account the physical phenomenons such as the inertia and friction. The rotation motion of a motor is first described by Newton's second law for rotation as

$$T = J\alpha, \tag{4.61}$$

where T is the torque, J the inertia, and α the angular acceleration. While angular speed ω has a more important meaning in a motor, the equation can be further written as

$$T = J\frac{d\omega}{dt}. \tag{4.62}$$

The motor mechanical equation can then be built on it. The torque in (4.62) represents the sum of all torques within the mechanical system. With the torque produced by the motor electrical system opposing to the load torque and friction torque, T is represented by the three torques [9]. They are

$$T_{motor} - T_{load} - T_{friction} = (J_{motor} + J_{load})\frac{d\omega}{dt}, \tag{4.63}$$

where T_{motor} is the motor torque, T_{load} the load torque, $T_{friction}$ is the friction torque. (4.63) essentially means that by overcoming the load torque, the extra motor torque is translated to speed. Nonetheless, since speed is translated by inertia, the coupled load inertia addition to motor inertia has to also be taken into account. Both motor and load inertia is connected via the same mechanical system the motor is driving. In the equation, the friction torque is a combination of viscous and Coulomb friction, where both of them are a function of angular speed [9]. The following is used

$$T_{friction} = D_m \cdot \omega + C_m \cdot sign(\omega). \tag{4.64}$$

where D_m viscous damping constant and C_m the Coulomb friction constant. Together, they define how the friction opposes the rotor movement [9]. Hence, by shifting the equation, the speed of the motor can be calculated by

$$\omega = \frac{1}{J_{motor} + J_{load}} \int (T_{motor} - T_{load} - D_m \cdot \omega - C_m \cdot sign(\omega))dt. \tag{4.65}$$

4.4 Motor dynamic parameters

Motor dynamic parameters often define motor performance and provide information on how a motor works under certain conditions. By defining and obtaining these dynamic performances, motor characteristics can be further identified and validated.

4.4.1 Torque/speed characteristics

To move an external load, a stepper motor needs to produce certain torque to overcome the load torque while rotating. Since the product of speed and torque is directly related to the amount of power the motor is being driven with, it is necessary to obtain such torque-speed characteristics to realize the maximum amount of torque a stepper motor can produce under different speed. A hybrid stepper motor is often defined by the pull-in and pull-out torque-speed curves, where each is defined as

- Pull-in torque-speed curve:
  The maximum torque that the motor can provide from standstill to rated speed. The motor has to successfully speedup from zero rpm to rated rpm.

- Pull-out torque-speed curve:
  The maximum torque that the motor can provide without losing a step. The motor has to successfully maintain the speed while increasing the load torque.

Figure 4.7 shows a typical torque-speed curve.
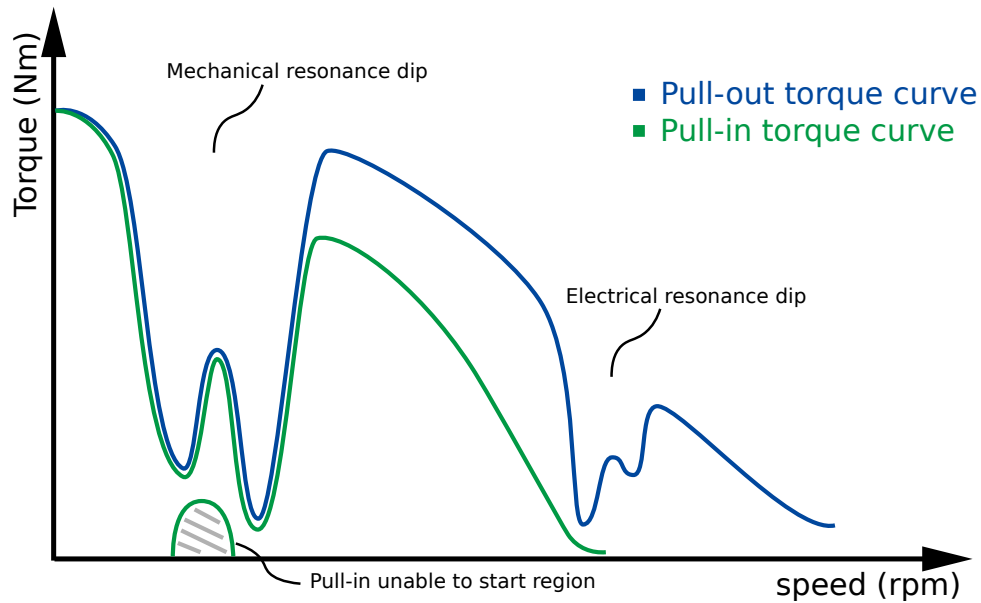
Figure 4.7: Pull-in/out torque-speed curve [8, 9].

The graph shows five distinct working regions [9]:

- Low-speed region (constant-torque region):
  In the low-speed region, both pull-out and pull-in torques are relatively flat. This is because torque is only limited by the input current. While speed is low, the motor can achieve stable torque.

- High-speed region:
  In the high-speed region, both pull-in and pull-out curves are reduced. Such a phenomenon is caused by the increase of induced voltage, or back-emf and lower currents. With higher induced voltage, the current is not able to achieve the rated current. Therefore, the torque produced is also lowered. Another phenomenon is that the pull-in torque has a lower maximum torque than the pull-out torque at a higher speed. This is because stepper motors are often not able to start from standstill in the higher speed caused by the mechanical friction torque.

- Mechanical resonance dip:
  Both pull-in and pull-out torque speed curve often encounter a resonance dip caused by the mechanical resonance. Such resonance can be produced by the mechanical friction, inertia, and stiffness shown in Subsection 4.4.2, and often happens in the lower speed range [9].

- Pull-in unable to start region:
  The pull-in curve will also encounter a region that is not able to start until a load torque is connected. Such a region is the shaded region in the figure. This is caused by the oscillation that naturally exists in the motor from its stiffness. To start at this region, a frictional, or load torque, is often needed to reduce the oscillation.

- Electrical resonance dip:
  The electrical resonance dip is often present in a stepper motor. The cause is often referred possibly to the stepping method and motor RL circuit [9].

Moreover, since the correct amount of damping, both electrically and mechanically, often reduces the resonance dips, an ideal pull-in and pull-out curve without the motor resonance region is shown in Fig. 4.8 [35]. Manufacturers often provide curves shown in Fig. 4.8 to show the fully operating motor dynamics [35]. The pull-out curve from manufacturers is often obtained by accelerating the motor to the desired speed and then increasing the load to the motor until the motor loses steps [35]. To obtain the pull-out curve without resonances, manufacturers regularly couple the motor with dampers to reduce or eliminate the oscillation.
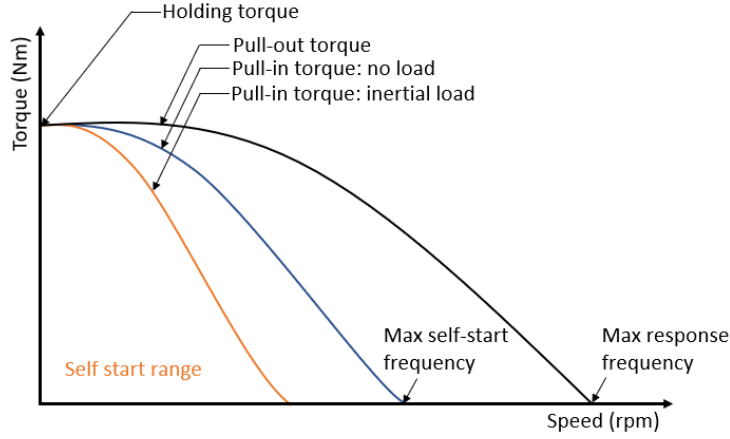
Figure 4.8: Ideal pull-in/out torque-speed curves.

In Fig. 4.8, the pull-in torque can be further separated into no-load and inertial load curves [35]. Such that, with load inertia, higher inertia from the load causes the motor to speed up much slower. Consequently, the motor will reduce its pull-in torque frequencies. Such curves are often not given from the manufacturer because they are highly dependent on the load condition the motor is connected to [35]. Nonetheless, the self-start range is defined as the region where the motor can successfully start and not lose steps. Likewise, the maximum self-start frequency is defined as the maximum frequency for the motor to self start with no load. Also, the maximum response frequency is the maximum frequency the motor can achieve without losing steps while running.

The motor dynamic curves are analyzed based on three regions of constant-torque, decreasing-torque, and high-speed regions in this thesis.

- Constant-torque region:
  The region where the rated current is achieved. Motor maximum torque can be achieved under the speeds in such a region.

- Decreasing-torque region:
  With motor inductance, the current requires time to increase. The current in the decreasing-torque region is not able to achieve the rated current because of the motor inductance. Furthermore, the back-emf increases with speed to further reduce the current level.

- High-speed region:
  Similar to the decreasing-torque region, the current is not able to achieve the rated current. Moreover, the back-emf in such a region became even higher to further reduce possible torque production.

4.4.2   Mechanical resonance and Stiffness

When driven in full-step mode, stepper motors react with step responses. Such response is oscillatory and is dependent on the stiffness of the motor. Stiffness is defined as the torque change due to the angle in the motor. It can be represented by

$$T = C_{stiff}\theta, \tag{4.66}$$

where C_{stiff} is the stiffness constant. Nonetheless, by equating the motor torque equation to the stiffness torque without a load torque, the stiffness can be equate to

$$C_{stiff}\theta = J\frac{d\omega}{dt}, \tag{4.67}$$

where the natural frequency can be obtained with the harmonic equation to be

$$f_{natural} = \frac{1}{2\pi}\sqrt{\frac{C_{stiff}}{J}} \tag{4.68}$$

With such oscillatory step response, there is a natural frequency that can effectively cause step loss in a stepper motor [9].. Therefore, because of the stiffness, it is often that pull-in/out torque-speed curve encounters loss of steps. This is often caused by the oscillatory rotor swinging out of equilibrium [9].

4.5   Controller and Drive

To drive a two-phase hybrid stepper motor in an open loop, a controller has to be able to feed switching pulses to the two phases of the motor. Such pulses are often produced through logic controls that generate fast-changing pulses. Often driver circuits consist of microprocessors or Field Programmable Gate Arrays (FPGAs) [31].

In between the control logic and physical motor lies the bridging circuit that provides the power to the motor. To create a current regulated constant voltage driver, an H-bridge circuit shown in Fig. 4.9 is connected.
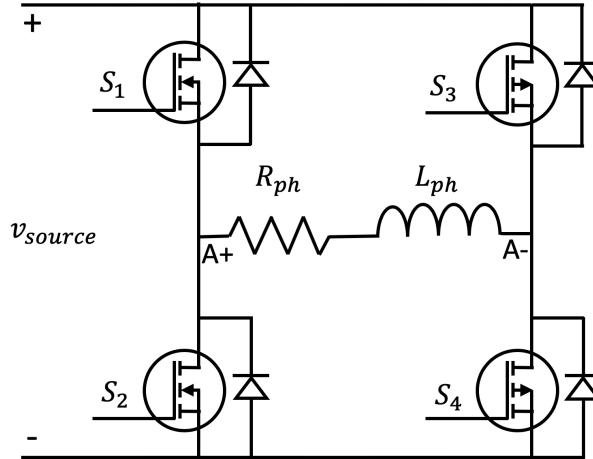
Figure 4.9: Single phase H-bridge circuit.

The v_{source} is the input source voltage. The circuit is a single phase H-bridge circuit that consists of four switches (in this case, four MOSFETs). Single H-bridge circuit can be used for a unipolar driver, similarly, two H-bridge circuits can be used for bipolar setup with each H-bridge connecting to each phases. The controlling of switches is configured to work in pairs, where switch S_1 and S_4 receives the same switching signal and switch S_2 and S_3 the same signal. While S_1 and S_4 are turned on, the current flows in the positive direction. Likewise, while S_2 and S_3 are turned on, the current flows in the negative direction. By obtaining the current level at the motor input, the switch pairs can be turned on and off to maintain that current level. This is done by the logic operation:

$$\begin{cases} v_{ph} = v_{source} & , i_{ph,ref} > 0 \quad \text{and} \quad i_{ph} > i_{ph,ref} - C_{margin} \\ v_{ph} = -v_{source} & , i_{ph,ref} > 0 \quad \text{and} \quad i_{ph} < i_{ph,ref} + C_{margin} \\ v_{ph} = -v_{source} & , i_{ph,ref} < 0 \quad \text{and} \quad i_{ph} > i_{ph,ref} + C_{margin} \\ v_{ph} = v_{source} & , i_{ph,ref} < 0 \quad \text{and} \quad i_{ph} < i_{ph,ref} - C_{margin} \end{cases} \tag{4.69}$$

where i_{ph} is the phase current detected at the switch output, $i_{ph,ref}$ the rated current, and C_{margin} the allowable margin for the current to fluctuate. C_{margin} is set to make sure that the H-bridge circuit is not constantly switching, or chopping [9].

Chapter 5

Simulink Modeling

A full-step current-controlled constant voltage driver, motor electrical module, and motor mechanical module are connected. They represent fully driven hybrid stepper motors.

- Current-controlled constant voltage drive:
  The current-controlled constant voltage driver is built to induce full stepping driver signal pulses. The switching pulses are generated based on the full stepping logic discussed in Section 2.5. Switching signal pulses is produced based on the intended rotation speed, motor rated parameters, and control method of the motor.

- Electrical module:
  The electrical module formulates the electrical and magnetic phenomenon in a physical motor. The physical motor coils are included by the electrical equivalent equation and the magnetic flux linkages are calculated based on the analytical equations in Section 4.1. The non-linear entities such as position dependencies and non-linear torque constant are also included here since the electrical module translates the electrical current to mechanical torque.

- Mechanical module:
  The mechanical module is coupled to take into account the mechanical phenomenon in a physical motor. The motor physical parameters such as rotor inertia and mechanical friction are implemented in this module. The load is coupled in this module by inducing a counter load torque to the electrical module torque output. The mechanical module also translates the access torque to motor speed based on the motor energy conservation shown in Section 4.3.

The driver, electrical module, and mechanical module are then coupled together to represent the full motor running dynamics. Non-linear variables in the stepper motor are implemented and validated. Within the electrical module, three different models are implemented. They are the generalized electrical model, flux-based model, and semi-analytical model.

- Generalized electrical model:
  The generalized electrical model is built with the hybrid stepper motor electrical linearized equations shown in Subsection 4.1.1. Such equations generalized the motor non-linear entities such as saturation and position dependency. While this model is often applied to estimate motor dynamics [10], it is a good indicator of physical motor dynamics under ideal conditions.

- Flux-based model:
  The flux-based model is built from a direct lookup table that is obtained from the FEA simulation. The lookup table (LUT) translates input phase currents to the relative flux linkages in each phase and total mechanical torque. Such a model can directly couple the non-linear entities in the material from the FEA since the entities are embedded directly in the LUT.

- Semi-analytical model:
  The semi-analytical model is built by including non-linear entities in the generalized electrical model. This is done by combining position dependencies and saturation via extra parameters and transforming the ideal motor parameters so that they are function-based parameters. The motor dynamics from the extra non-ideal inputs are to be compared to the motor dynamics obtained from

49

LUT. This verifies possible non-linear parameter ranges. This model is also applied and verified with multiple motors and motor datasheet parameters.

5.1   Current-controlled constant voltage driver

A current-controlled constant-voltage driver is implemented in all three models [10]. Shown in Fig. 4.9, a real-life constant voltage driver consists of two H-bridge circuits. Each H-bridge circuit consists of four MOSFET switches that work in pairs. Controlling signals are connected to the MOSFET switches. The switching signals are often produced with either of the three methods: logic sequencing circuit, microprocessors, and FPGA [8, 21]. Since signal sequencing can be implemented directly through combinations of MATLAB/Simulink toolbox blocks, a driver sequencer is built by coupling lookup tables to translate switching signals from a continuous repeating step increase signal. The driver circuit implemented is shown in Fig. 5.1.
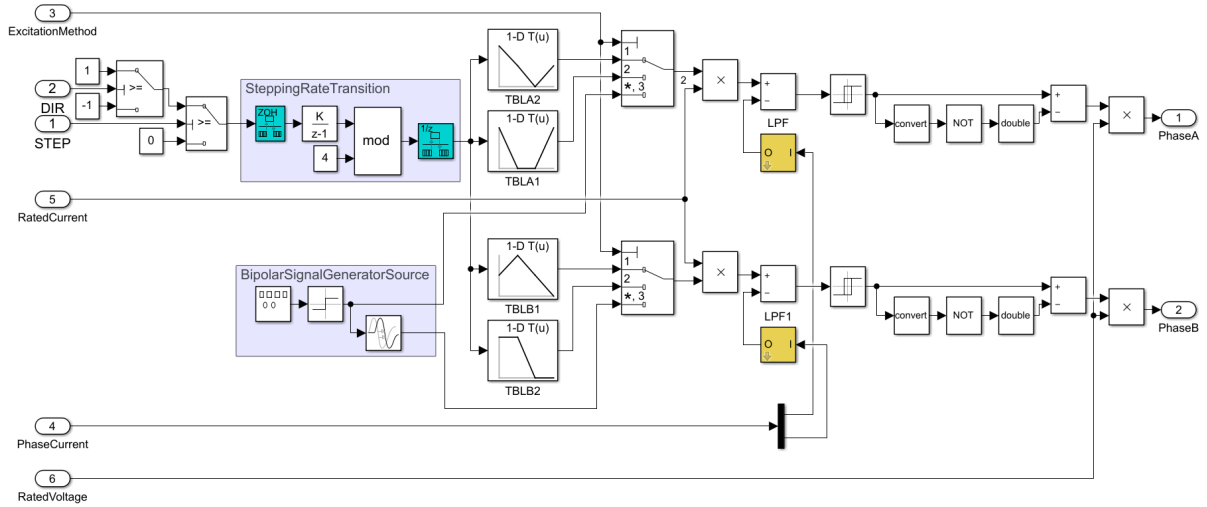
Figure 5.1: Two-phase current-controlled constant voltage driver model.

The inner connections of the full-step motor driver block are shown in Fig. 5.1. Here, three different driver signals are created and selected by the "ExcitationMethod" constant. Three excitation methods are implemented as:

- ExcitationMethod = 1:
  First, DIR and STEP input defines the input direction and ON/OFF of the stepper motor. The stepper motor rotates clockwise When both DIR and STEP are ones, anti-clockwise when the DIR is set to zero and STEP set to one, and stop running when STEP is set to zero. Such controlling signals are then integrated based on both the motor stepping rate and sampling time. The transition rate follows

$$Nstep = \left\lfloor \frac{1}{stepRate \cdot Ts} \right\rfloor, \tag{5.1}$$

  where $Nstep$ is the sampling rate inside the rate transition block (shown in purple), $stepRate$ is the speed of each step in the motor, and T_s is the sampling time of the process.

  With the running rate signal computed, the output of the step rate transition block is then modulated by four for the four distinct stages in a single-phase excitation switching sequence shown in Fig. 2.14 (a). The four states of both phases A and B are then translated via the lookup tables.

- ExcitationMethod = 2:
  Same as the one-phase excitation method, the two-phase excitation method also translates the stepping rate via rate transition block. Instead of a one-phase lookup table, the input four states signal is translated to a two-phase excited sequence shown in 2.14 (b).

- ExcitationMethod = 3:
  Same as the second method, the third excitation mode also produces a two-phase excited signal. Such a method is, however, implemented with different MATLAB/Simulink blocks. Instead of creating a discrete signal from the rate transition block and sequencing lookup table, this method implements a signal generator block. A square wave is then created through a signum function. By shifting the sinusoidal function by 90°, the sequential signals can be created for phases A and B. An important benefit of such a method is that, unlike rate transition block where the first signal is produced depending on the transition rate, the signal generator generates signals from time zero. Such a method ensures that the initial rotor angle position can be fixed.

After the creation of the control signal, the output phase currents are then fed back to be compared with the control signals. The differences of such signals are indicators of the switching in the H-bridge shown in Section 4.5. By doing so, the current is kept within a range of the rated current disregarding the voltage level. In the model shown in Fig. 5.1, instead of sensing the H-bridge output current, the phase currents are fed by the electrical motor module since the H-bridge output current should be equal to the motor current. It is therefore not necessary to implement a real H-bridge block in the driver circuit. The output phase voltages are then the multiplication of Udc, the rated voltage, and on/off logic. Two-phase switching voltage is then connected to the generalized electrical model, flux-based model, and semi-analytical model.

5.2 Electrical Module

The electrical module translates the electrical energy through magnetic energy into mechanical energy. Three models with different building components are built in this section to take into account the non-linear entities in electrical, magnetic, and torque perspectives.

5.2.1 Generalized electrical model

The general electrical model is built based on the electrical linearized equation shown in Subsection 4.1.1 where the input voltage is equal to the sum of voltage consumed through coil resistance calculated by Ohm's Law, the self-induced voltage from the coils, and magnet flux induced voltage in the coils. This model assumes an ideal operation where no loss is present in the transition between different energies. Nonetheless, the torque production is built based on the co-energy equation shown in Section 4.2.

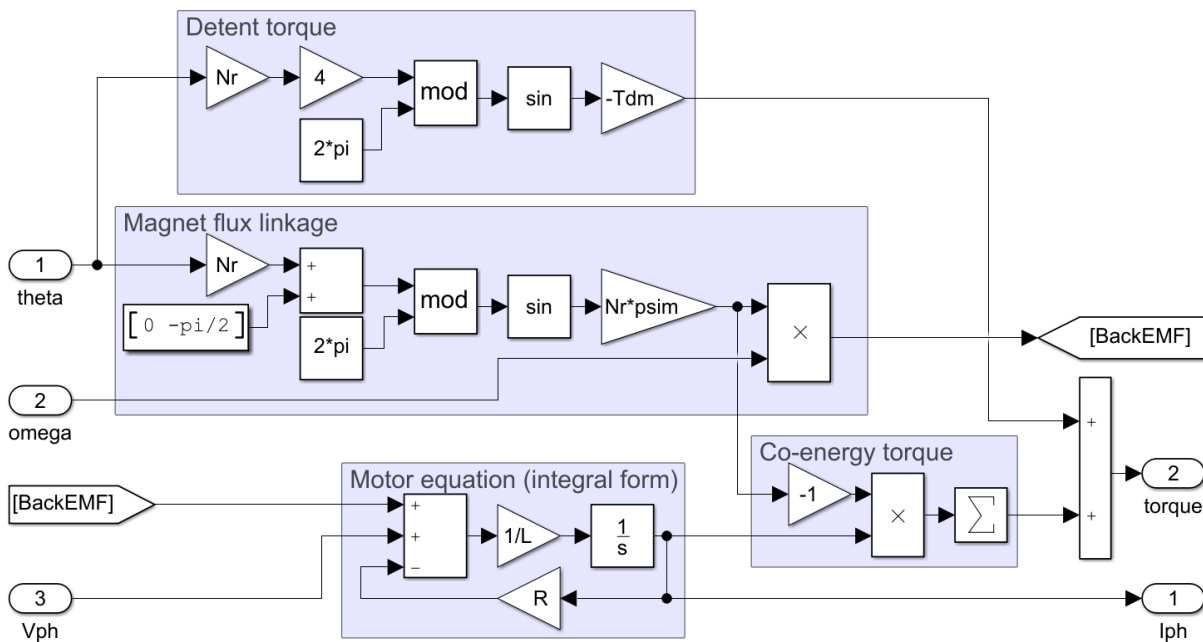The general electrical model is built with the motor analytical equations as shown in Fig. 5.2.

Figure 5.2: Generalized electrical model.

By following the relative equations shown in Chapter 4, the generalized model is combined and inter-connected with four basic blocks:

- Magnet flux linkage:
  The magnet flux linkage equation (4.11) and (4.12) are modeled directly in vector forms.

- Motor equation:
  The motor equation is modeled with the integral form of (4.13) and (4.14), where current is the equated variable to be solved. The initial condition of the integrated current is set based on the simulation dynamics. If simulated from a standstill, the initial condition is set to zero to reflect zero current from the start. If simulated from constant speed, the initial current is set based on the motor inductance, simulation start position, and speed to reflect the current level at that time of rotation.

- Co-energy torque:
  The torque is calculated based on the co-energy defined in the energy conservation equation (4.56) where the change in inductance is ignored based on the ideal assumption in the generalized electrical model. The torque created from the two phases is then added together to form the motor torque.

- Detent torque:
  The detent torque is modeled based on equation (4.60) where only the fundamental 4th harmonic detent torque is modeled. The higher harmonics are ignored in this case by assuming the motor structure to be ideally diagonally symmetrical.

Notice that variables "Vph", "Iph" are vectors of phase A and phase B. Whereas "theta", "omega", and "torque" are scalar variables of the motor.

5.2.2   Flux-based model

Since the generalized electrical model translates the electrical energy through magnetic energy to mechanical energy without considering the losses in translation, the flux-based model focuses more on the magnetic energy losses in the motor structure. To do this, the FEA model is numerically simulated to obtain a numerical output with different current levels and positions. The magnetic flux and torque are therefore a function of current and position.

The 3D FEA model built in Chapter 3 is first numerically computed with simulation configurations shown in Fig. 5.1.

Table 5.1: FEA simulation configurations.

Parameter name	Range	Data point [-]
Rotor position	$0.0° \sim 3.6°$	13
Current phase A	$-1.7A \sim 1.7A$	7
Current phase B	$-1.7A \sim 1.7A$	7

The input current ranges from -1.7A to 1.7A where the rated current of such motor is 1.68A. Higher input currents to the FEA model is to make sure that the peak currents over 1.68A in the MATLAB/Simulink model can also be simulated correctly without extrapolating the out-of-range data points. Thirteen data points are equally distributed from mechanical angle 0° to 3.6°. Here, instead of simulating a fully mechanical revolution 360°, only four mechanical steps are simulated since the rotor position is repeating every mechanical angle of 3.6°. While the rotor is modeled symmetrically, we know that the torque and magnetic flux experienced on the motor lamination is repeating every four steps. Therefore, to reduce the number of data points needed to be numerically solved, four mechanical steps are simulated. Nonetheless, thirteen data points are simulated by dividing the rotor positions to increments of 0.3°. By having the number of data points that are a multiple of four, the first harmonic of motor torque where torque peaks are obtained at the correct 0.9° rotor position.

The FEA simulated output data then consist of six parameters:

- Current phase A (IA),

- Current phase B (IB),

- Rotor position (ANGPOS_ROTOR),

- Flux phase A (FLUXA),

- Flux phase B (FLUXB),

- Motor torque (ELTORQ_ROTOR).

The obtained variable data are then inserted into the flux-based model LUTs. The flux-based electrical module is shown in Fig. 5.3.
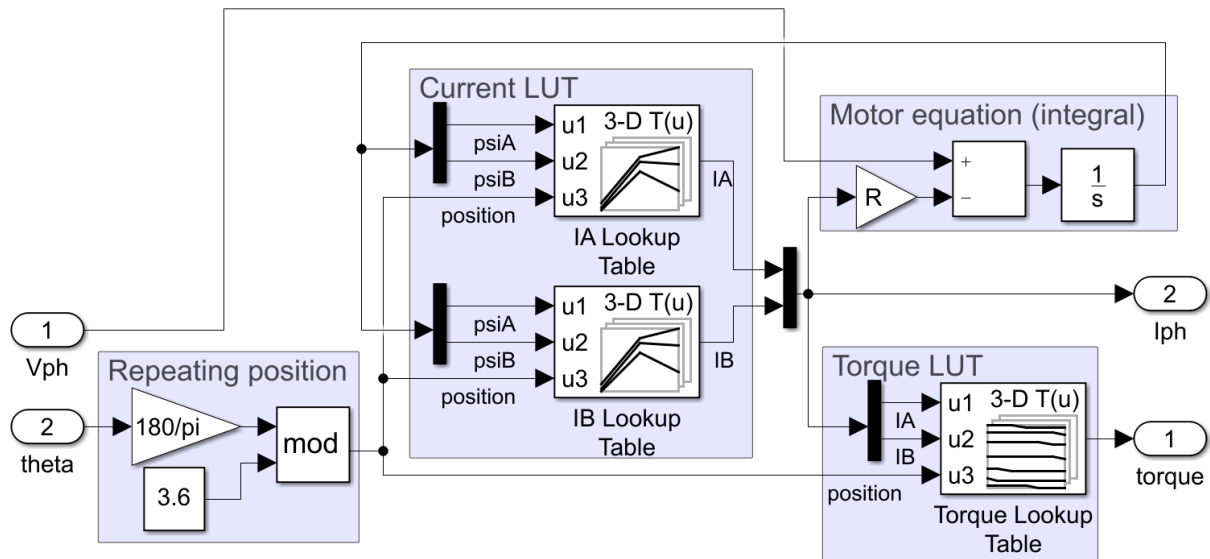
Figure 5.3: Flux-based model.

The flux-based model is modeled directly with the electrical equation based on the flux linkages shown in (4.42). The model is combined with four blocks:

- Repeating position:
  Since the LUTs are obtained with only four mechanical steps (3.6° mechanical angle), the motor rotational angle has to be translated to a repeating motion based on the four mechanical steps. A full revolution (360°) is translated to repeat mechanical angle from 0° to 3.6° 100 times. The repeating position block modulates the real motor position by 3.6 to convert the positions to the LUT positions.

- Current LUT:
  The current LUT block is implemented with two 3D LUTs that output Phase A current and Phase B current by inputting phase A flux, phase B flux, and position shown in (4.42). However, since the fluxes are intuitively a function of current when the FEA model calculates the fluxes by various input currents, the obtained flux intuitively only works for derivative form (4.41). To apply it in (4.42), a reverse LUT illustrated in Fig. 5.4 is needed to make input current a function of phase fluxes.
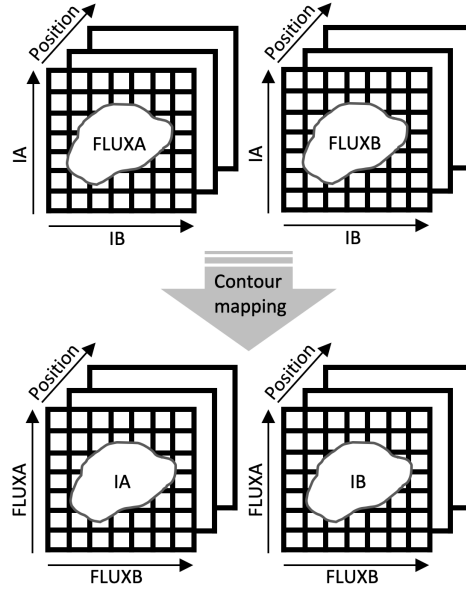
Figure 5.4: Reversed LUT 3D matrix.

A reverse LUT procedure based on contour mapping is applied [36]. First, the original LUTs, $\psi_A(i_A, i_B, \theta)$ and $\psi_B(i_A, i_B, \theta)$, are linearly interpolated in the i_A and i_B dimensions. Then two contour lines are drawn for both ψ_A and ψ_B on the same axes of i_A and i_B, in which i_A is the horizontal axis and i_B the vertical axis. By doing so, the crossing point of (ψ_A, ψ_B) has a corresponding point (i_A, i_B) [36]. For each flux point, the relative current input can then be located. Since this method relocates the 2D matrices, the same procedure is done throughout the position dimensions. By defining a new 2D grid of ψ_A and ψ_B, the corresponding i_A and i_B can then be mapped as Fig. 5.5.
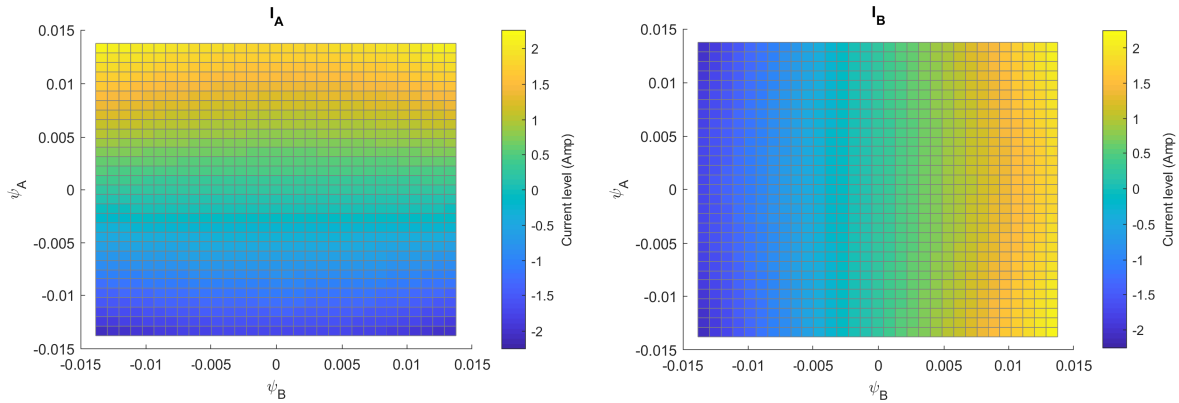
Figure 5.5: Flux lookup tables (left) i_A (right) i_B.

The current LUTs are then inserted into the 3D LUT blocks as shown in Fig. 5.3.

- Torque LUT:
  Similar to current LUT, the torque LUT is also extracted from the FEA model. The torque in this case is directly a function of phase currents. The torque is numerically calculated through the Maxwell stress tensor equation and solved by FEA. The torque LUT is connected to the output of current LUT and outputs the motor mechanical torque. The initial flux linkage from the integration is set to *psim* because, initially, flux linkage is only present from the magnet.

- Motor equation:
  Since the input phase fluxes for the current LUTs are functions of currents, the fluxes have to be

translated from the currents through the motor equation shown in (4.42). Therefore, the currents and resistance products are integrated to obtain the motor fluxes as shown in Fig. 5.3.

With the four blocks, the output torque is obtained through input voltage and motor position.

5.2.3 Semi-analytical model

By applying the flux-based model, motor dynamics can be obtained through the LUT. Since the flux-based model is built on the LUT created by the simulated dynamics of the FEA motor model, an FEA model has to be built. Building an FEA model, both in 2D and 3D, however, requires detailed parameters of the motor geometry and material. Such details are often not accessible to the purchaser. Therefore, to create a model that takes into account some of the non-linear entities, it is a better option to build the model with non-linear dependencies, shown in Subsection 4.1.2, based on the general electrical model.

In the semi-analytical model presented, it takes into account the position dependency, mutual inductance, non-linear torque, and higher harmonics of detent torque. The electrical module of the semi-analytical model is shown in Fig. 5.6.
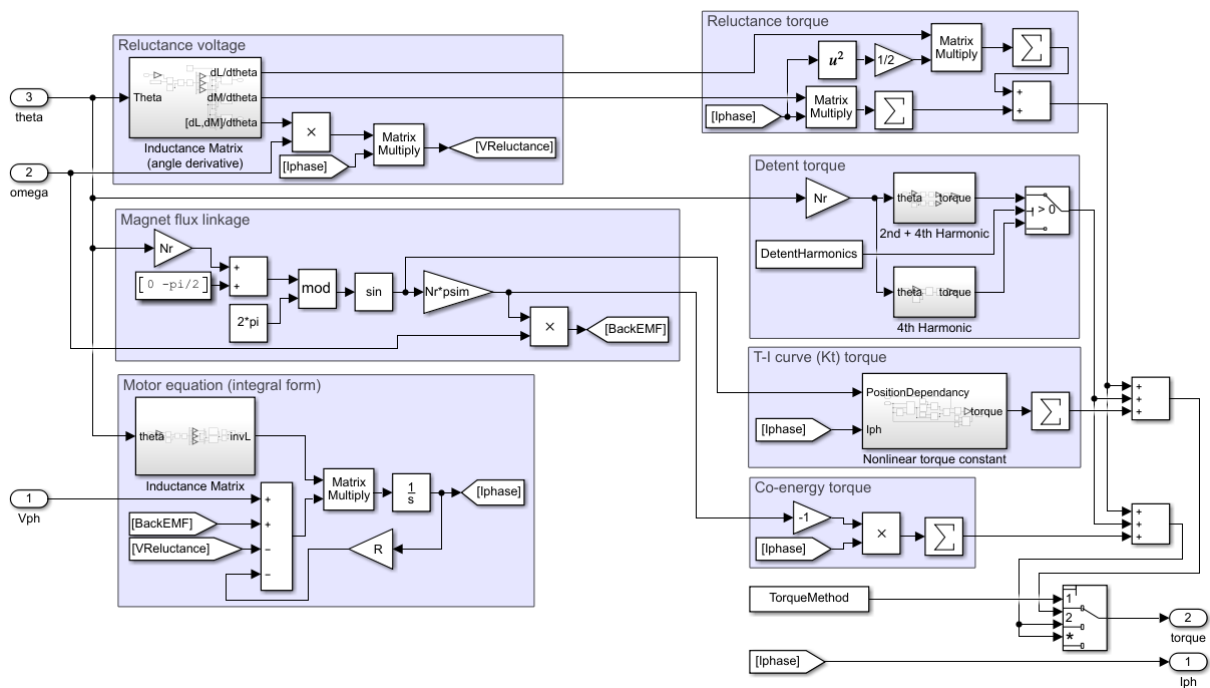
Figure 5.6: Semi-analytical model.

The semi-analytical model consists of seven blocks that are combined to simulate the motor with position dependency, mutual inductance, non-linear torque, and higher torque harmonics. The variables defining such non-linear entities are to be obtained through either the datasheet or FEA dynamic parameters such as pull-in/out torque or oscillation.

The seven blocks can be separated into two main parts of current development and torque generation. The current development consists of blocks of magnet flux linkage, reluctance voltage, and motor equation. Whereas the torque generation consists of blocks detent torque, reluctance torque, T-I curve torque, and co-energy torque.

The current development blocks are implemented as the following.

- Magnet flux linkage:
  Directly implemented from the fundamental electrical model, the same position dependent flux equations shown as the last part of (4.13) and (4.14) are implemented.

- Reluctance voltage:
  Since the ideal model does not take into account the rotor saliency in the hybrid stepper motor, the

reluctance is also ignored [10]. Yet, in reality, the rotor saliency is shown in Section 3.2 is always present in the stepper motor. Such saliency translates to an increase in induced voltage caused by the change in air gap reluctance. Therefore, the reluctance voltage created with position derivative in (4.40) is modeled into the reluctance voltage block. To derive the inductance matrix shown in (4.27), the sinusoidal derivation law is applied and implemented as shown in Fig. 5.7.
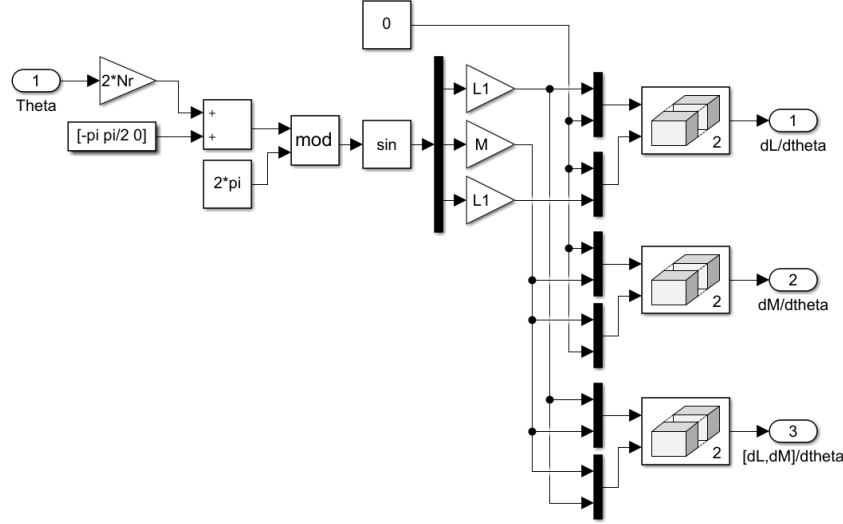
Figure 5.7: Angle derivative of the Inductance matrix.

Here, L_1 is the position derivation of change in inductance and M the position derivation of change in mutual inductance. Combining the matrices, the output "[dL, dM]/dtheta" is then multiplied with the speed and current matrix to output the reluctance voltage that also summates to the total induced voltage.

- Motor equation:
  Similar to the generalized electrical model, the semi-analytical motor equation is also modeled based on (4.1) in an integral form. However, the induced voltage is the combination of back-emf and reluctance voltage. Since mutual inductance and inductance position dependency is taken into account, the inverse inductance $\frac{1}{L}$ shown in Fig. 5.2 has to be extended with a new inductance matrix shown in Fig. 5.8.
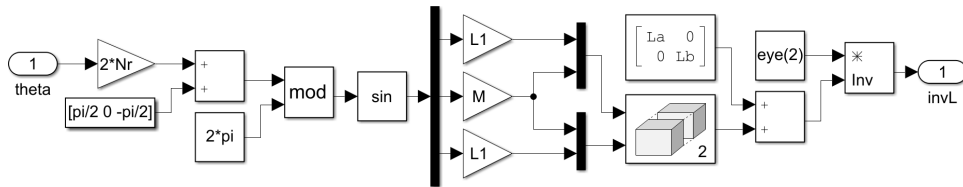
Figure 5.8: Inductance matrix.

The inductance matrix is modeled based on (4.27), where the L_A and L_B are fundamental inductances that are given in the datasheet. The L_1 and M with position dependencies are then combined with the fundamental inductance to form the inductance matrix. The inductance matrix is then inverted for the integral calculation based on (4.40) in the motor equation block. Moreover, the initial current from the integration block is set the same as the generalized electrical model.

The torque generation blocks are implemented as the following.

- Detent torque:
  Unlike the detent torque block in the generalized electrical model shown in Fig. 5.2, the detent torque in the semi-analytical model takes into account the lower harmonics that can be caused by the half model asymmetry shown in Fig. 3.25. Shown in Fig. 3.24, the 2nd harmonic can indeed

be present in a hybrid stepper motor. Therefore additional to the 4th harmonic detent torque, an equation with a fundamental 2nd harmonic detent torque is also implemented. The combined 2nd and 4th harmonics can be induced via the selection variable "DetentHarmonics". The fundamental detent torque with 2nd and 4th harmonics is implemented as shown in Fig. 5.9
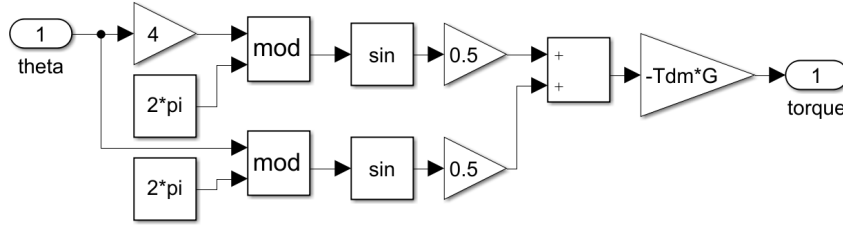
Figure 5.9: Detent with 2nd and 4th harmonics.

The detent torque is modeled with both 2nd and 4th harmonic sinusoidal waves based on the motor position. In order to produce a wave that has the maximum detent torque based on the motor datasheet, a constant "G" is then multiplied to correctly implement the wave with peak detent value of the datasheet. The constant "G" is calculated by

$$G = \frac{1}{\max\left(\frac{\sin(x+\pi)}{2} + \frac{\sin(4(x+\pi))}{2}\right)}. \tag{5.2}$$

By multiplying the T_{dm}, given in the datasheet and shown in (4.60), to "G", the detent torque with 2nd and 4th harmonics can be modeled.

The higher harmonics described in Subsection 4.2.2 are not implemented here because higher harmonics are often caused by structure asymmetry which is not possible to be known without measurement or FEA modeling. Since the semi-analytical model is constructed to reduce the need for physical measurement and motor structure modeling, higher harmonics are therefore not modeled.

With the detent torque harmonics modeled, the detent torque is then subtracted by the total torque in the detent torque block.

- Reluctance torque:
  The reluctance torque is another non-linear entity that is modeled from (4.2.2) where the reluctance torque can be produced because of the motor saliency. Such torque is the main torque source for a VR stepper motor. Since hybrid stepper motors also contain saliency, the reluctant torque is therefore implemented. The input angle derivative based on self-inductance L_A and L_B and mutual inductance M is fed from the angle derivative inductance matrix in the reluctance voltage block. They are then calculated based on (4.2.2) in the reluctance torque block.

- T-I curve (Kt) torque:
  Since the torque rating of a motor can also be defined as the torque constant of the motor, another method to obtain the motor torque is to directly multiply the torque constant with the current and position dependency shown in (4.57). Such a method however assumes the torque constant to be linear. Yet, because of the B-H curve in the motor lamination structure, the maximum torque is also limited with respect to the current shown in Fig. 3.28. Therefore, the T-I curve torque implemented here multiplies the current with a current dependent torque constant defined in the non-linear torque constant block. Such a block is implemented as shown in Fig. 5.10
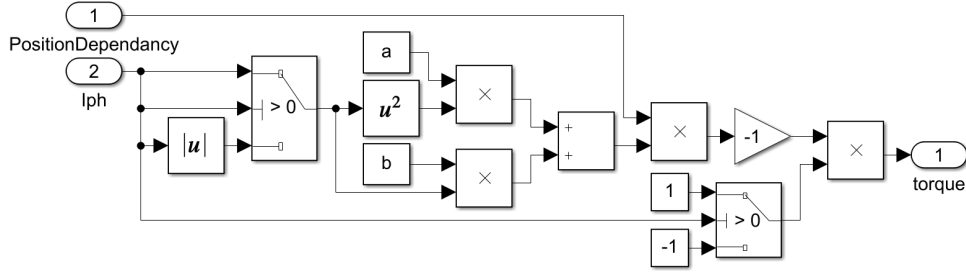
Figure 5.10: Non-linear torque constant implementation.

The current dependent torque constant is implemented with a second-order equation to estimate the torque constant curve. The constants "a" and "b" are the definition variables for the second-order equation. Such an equation can be obtained by curve fitting or estimation. The torque curve from the stepper motor in Chapter 3 can be obtained from torque fitting such curve to a quadratic equation in Fig. 5.11.
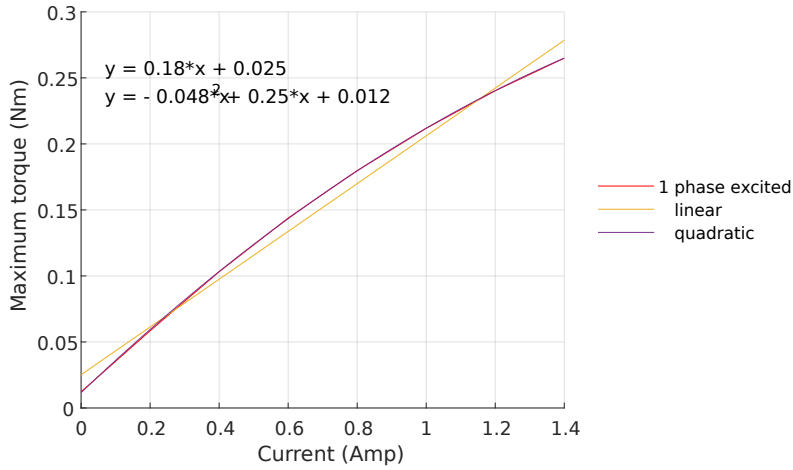
Figure 5.11: Curve fitted function from torque-current curve.

The linear equation can be obtained to see that the torque constant of such a motor is indeed 0.18Nm/A. The quadratic function variable "a" and "b" are -0.048 and 0.25 respectively.

Nonetheless, another method is to mathematically define the curvature of the arc to estimate the torque curve. This is done by defining the "a" variable as the curvature constant and equating "b" to

$$b = \frac{K_t \cdot I_{rated} - a \cdot I_{rated}^2}{I_{rated}}, \qquad (5.3)$$

where K_t is the torque constant. The equation is derived from the fundamental quadratic function of the form

$$y = ax^2 + bx. \qquad (5.4)$$

With different curve constant "a", saturation level toward different current level can be estimated as shown in Fig. 5.12.

58
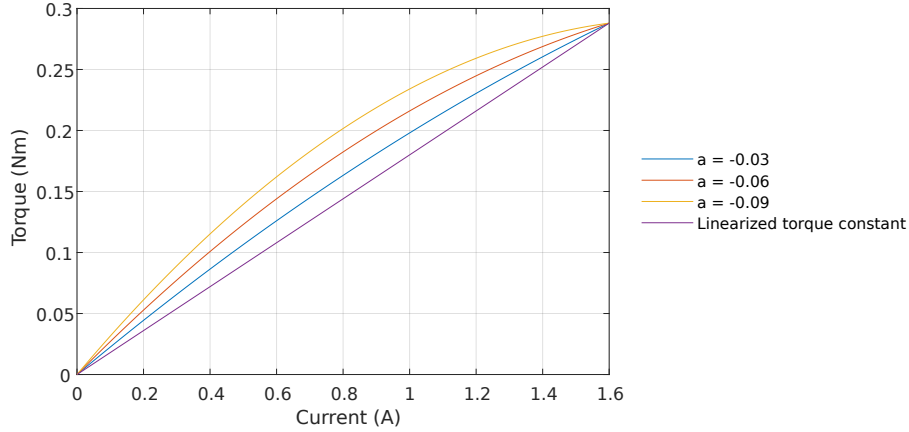
Figure 5.12: Estimated torque-current curve.

The equation (5.3) is then applied to the MATLAB/Simulink model shown in Fig. 5.10 to form the basis of the T-I curve block. The output torque is then obtained by inputting the current through the equation and multiplying the result to the position dependency that oscillates the actual output torque.

• Co-energy torque:
The co-energy torque is also implemented here as a possible implementation when the rated current is far less than the saturation current. In such region saturation has a minimal effect, therefore, co-energy torque can be directly implemented. A switch with a "TorqueMethod" variable is therefore implemented when the co-energy equation is preferred.

5.3   Mechanical module

The torque output from the electrical module is then connected to the mechanical module. The mechanical module is built based on (4.65). The model is shown in Fig. 5.13.
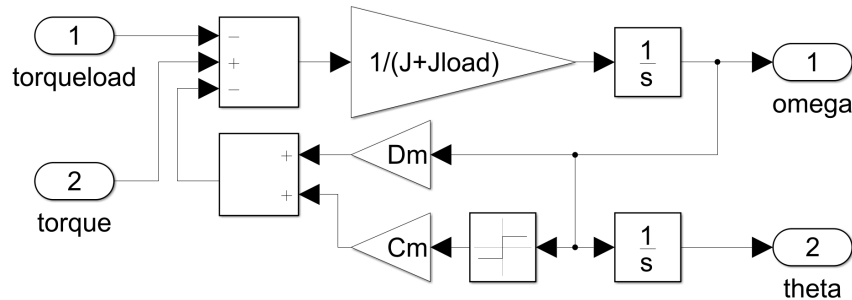
Figure 5.13: Mechanical model.

In the mechanical model, the difference between the load torque and electrical torque output is then translated into the speed and position through integration. Such output speed and angle are then fed back to the electrical model. The J and J_{load} are the motor and load inertia. Nonetheless, D_m and C_m are often not given in the datasheet and are required to be estimated or experimentally measured [37]. In our case, the constants are estimated by comparing the output motor dynamics from the model and datasheet. Here, the initial condition for omega is set to zero for initially standstill simulation and rated speed in radians per second for constant speed simulation. The initial condition for theta is set to the relative stator pole position from the excited coils.

5.4 Full modules

Finally, two full models are applied in this thesis, with and without a mechanical block.

5.4.1 Semi-analytical model with mechanical block

First, the model with a mechanical block is shown in Fig. 5.14. Here another slip block is implemented to detect the slip of the motor under different load torque. This model is used to obtain the pull-in/out curves in Chapter 7. Within the electrical module, three different electrical models are implemented.

Figure 5.14: Full model with mechanical block

The pull-out torque curve is obtained by detecting the unsynchronized rotor. Since stepper motor speed and position are directly linked to the electrical signal, the speed can be translated to the signal switching speed. Rotor slip can be detected when rated speed from the signal is not achieved or the position expected is inexact. The slip detection sub-block showed in Fig. 5.14 is implemented as shown in Fig. 5.15.

Figure 5.15: Slip detection sub-block.

Figure 5.16: Ramp and saturation function for load torque input.

The load torque Tl showed in Fig. 5.14 is replaced by an increasing ramp block and a saturation block shown in Fig. 5.16 to increase the torque from zero to Tl while running the motor. The pull-out curve is obtained by slowly increasing the maximum load torque until the slip is higher than the tolerance throughout the iterations. Once the iteration ends, the peak torque is obtained for that speed. It is then iterated through the manufacturer given curve speed set points. The pull-out torque flow chart with a half-interval search algorithm is shown in Fig. 5.17. Once the peak torque for a specific speed is detected, the next speed is applied until all speeds of the pull-out curve are obtained.

Figure 5.17: Pull-out curve with mechanical block algorithm flow chart.

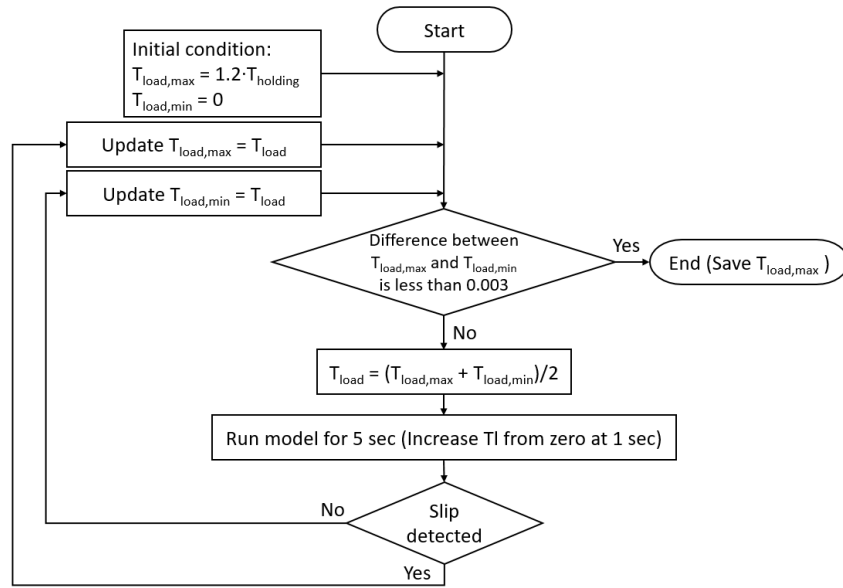Similar to the pull-out torque, pull-in torque can be obtained with a similar algorithm. The model in Fig. 5.14 is directly implemented without applying the ramp and saturation blocks. The pull-out curve flow chart is shown in Fig. 5.18.
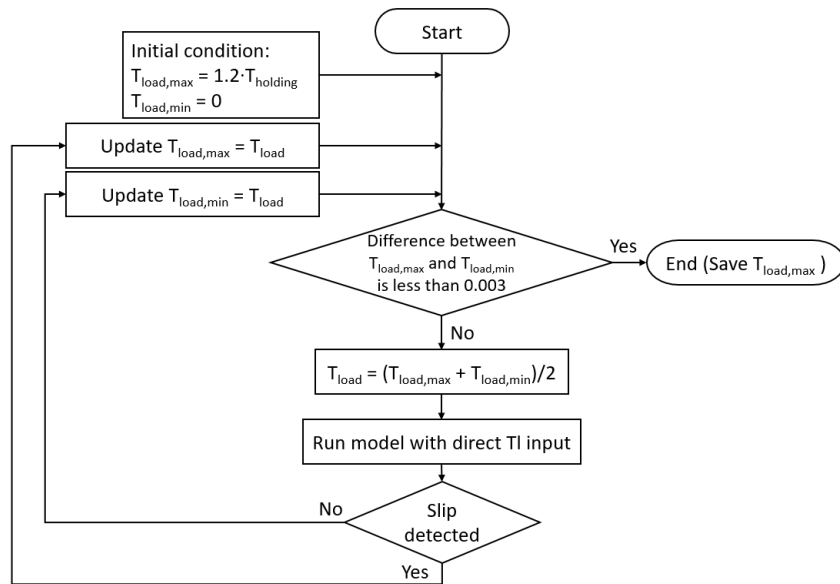
Figure 5.18: Pull-in curve algorithm flow chart.

5.4.2 Semi-analytical model without mechanical block

Second, the model without a mechanical block is shown in Fig. 5.19. An additional continuous speed block is implemented instead of a mechanical block. Such a model is applied to directly average the torque output from the electrical block. The motor torque is produced by the difference between the expected position and driver position. This is done by applying an external speed and position to the electrical block while still driving the motor model with the voltage limited current-controlled driver. With such connection, each step response produces an angle difference between the continuous position increases, fed by external continuous angle signal, and the driver angle, which follows the step increase. Higher the position difference, the higher the motor torque is experienced.
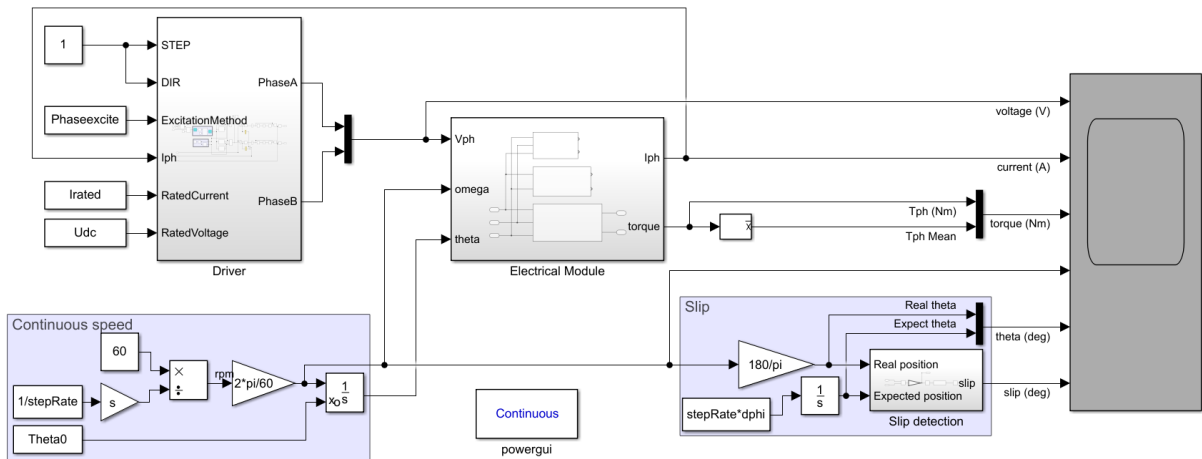
Figure 5.19: Full model without mechanical block.

For example, at 0.003 to 0.005 seconds of Fig. 5.20, the motor current draws the rotor to a mechanical position at 0.9°; however, because of the difference between the continuous increasing position and stable 0.9° step position, the torque slowly increases from -0.1 to -0.44Nm. The torque is created by the position misalignment. The increase slowed down sinusoidally at 0.0045 to 0.005 seconds when the position difference between stator teeth and rotor teeth are at their maximum. At 0.0025 second, the phase current experienced a polarity transition and consequently increases the rotor by one step and decreases the torque. The transition repeats itself under the same speed.
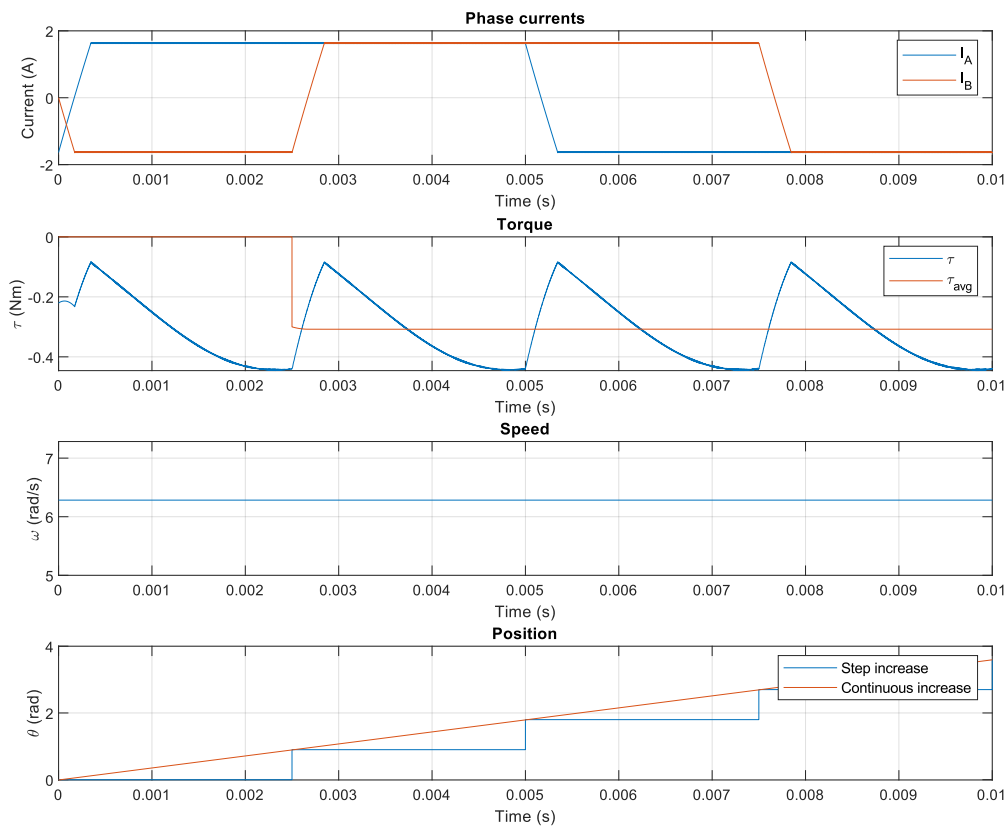
Figure 5.20: Motor dynamics at 60 rpm without mechanical block.

Chapter 6

Experimental validation and verification

6.1 Stepper motor test bench design

A test bench is shown in Fig. 6.1 is designed to obtain dynamics and parameters by running the stepper motor with the driver circuit, running the hysteresis brake and BLDC motor as the load, and measuring the torque with the torque transducer.
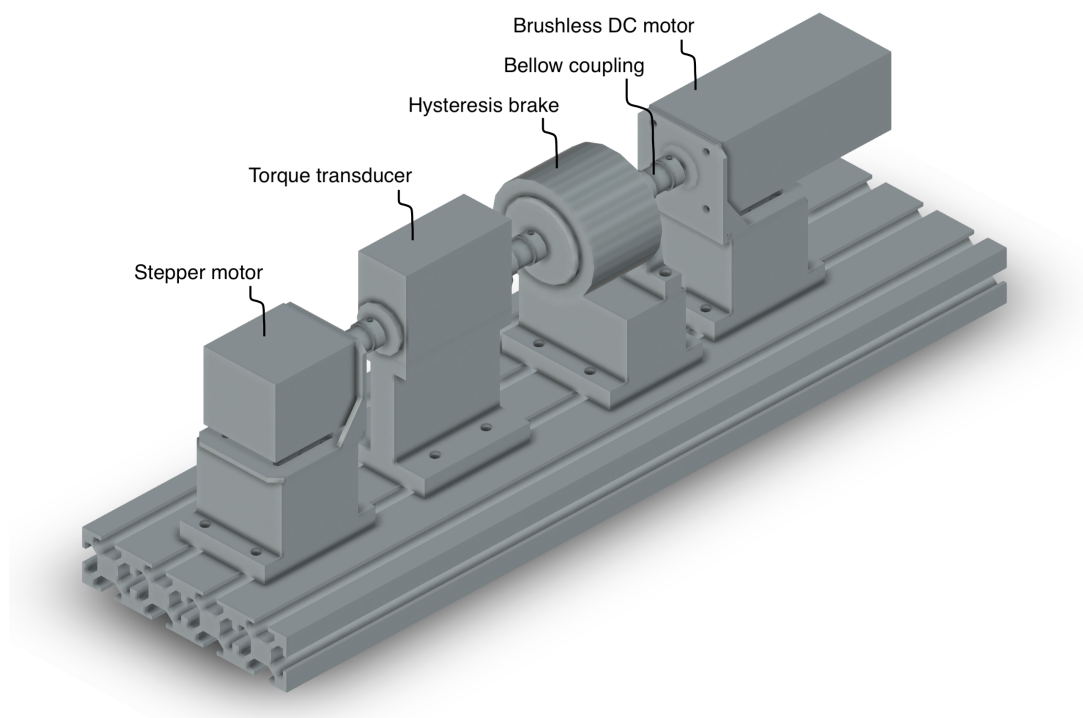
Figure 6.1: Test bench setup three-dimensional view.

The equipment connected on the same shaft shown in Fig. 6.1 are the stepper motor, torque transducer, hysteresis brake, and BLDC motors. They are all connected through the bellow couplings. The parts selected to be used in the test bench are:

Table 6.1: Equipments selection.

Equipment	Model	Manufacturer	I_{rated}	V_{rated}	ω_{rated}	τ_{rated}
Stepper motor	ST4209L1704-A	Nanotec	1.68A	3V	-	0.44Nm
Torque transducer	1701 0.5Nm	Honeywell	<0.2A	12V	37000	0.5Nm
Hysteresis brake	HB-50M-2	Magtrol	<0.96A	24V	15000	0.35Nm
BLDC	DB42C01	Nanotec	4.63A	48V	6000	0.25Nm

The overall torque ratings are selected to be less than that of the stepper motor. This is to obtain the motor dynamics without losing steps. To obtain the step lose dynamics, the BLDC motor can achieve 0.75Nm peak torque. The test bench with an additional oscilloscope and LCR meters are designed used to obtain motor parameters and dynamics listed below.

- Inductance and resistance:
  Since inductance and resistance in the datasheet consist of high tolerances of 15% and 20%, the LCR meter is used to ensure the correct parameter levels with fewer tolerances. The stepper motor inductance and resistance are measured and shown in Table 6.2.

Table 6.2: Measured inductance and resistance.

	Avg
Motor inductance	6mH
Motor resistance	2.1Ω

- Mutual inductance:
  By connecting phases A and B in series, the mutual inductance can be measured. When the circuit is seen from the positive connection, the total inductance is

$$L = L_A + L_B + 2M. \tag{6.1}$$

Similarly, when the circuit is seen from the negative connection, the total inductance is

$$L = L_A + L_B - 2M. \tag{6.2}$$

Subtracting the two equations from one another, the mutual inductance can be calculated to be four-times the difference from positively and negatively measured inductance. By measuring the inductance with an LCR meter two times with opposite polarity, the mutual inductance is measured. Multiple motor positions of the mutual inductance are measured as shown in Table. 6.3.

Table 6.3: Measured mutual inductance.

	Min	Max
Mutual inductance	0.01mH	0.3mH

- Detent torque:
  The detent torque of the stepper motor is measured by running the stepper motor at a constant speed and detect the torque change from the torque transducer. The BLDC is used to feed a constant speed to the connected shaft. The constant speed is achieved by applying a speed control on the driver to the motor. This is done through the Cygnus drive from Prodrive Technologies.

- Position dependency:
  Position dependencies of the stepper motor on both the inductance and torque are measured by fixing the shaft angle with the hysteresis brake. To measure the inductance, the LCR meter is connected to both phases while small angle shifts are applied after each angle measurements. Similarly, the torque position dependency is measured by connecting both phases to a constant current source underrated current. The maximum torque is then measured step by step through the torque transducer.

- Pull-in/out curves under different load conditions:
  The pull-in and pull-out curves are obtained iteratively through the different motor speeds. The pull-in torque is measured by running the motor from standstill to a motor speed with a switching signal. The switching speed is also the motor speed. By applying different static loads with the hysteresis brake on different switching speeds, the maximum torque is measured for the motor to start without losing steps on that specific speed. The different maximum torque at multiple speeds is defined as the pull-in torque. The pull-in speed measured is rated for the combined inertia on the test bench.

  The pull-out torque is measured by running the motor up to a certain speed through a slow start. At the constant speed, then apply an increasing load with the hysteresis brake until the motor losses steps. The maximum torque without it losing a step is then defined as the pull-out torque at that speed.

6.2 Driving and control

The control and drive connections are shown in Fig. 6.2, where the orange line represents the feedback signal from the encoder and torque transducer. The blue, on the other side, represents the output driver signals for both the stepper motor and BLDC motor.
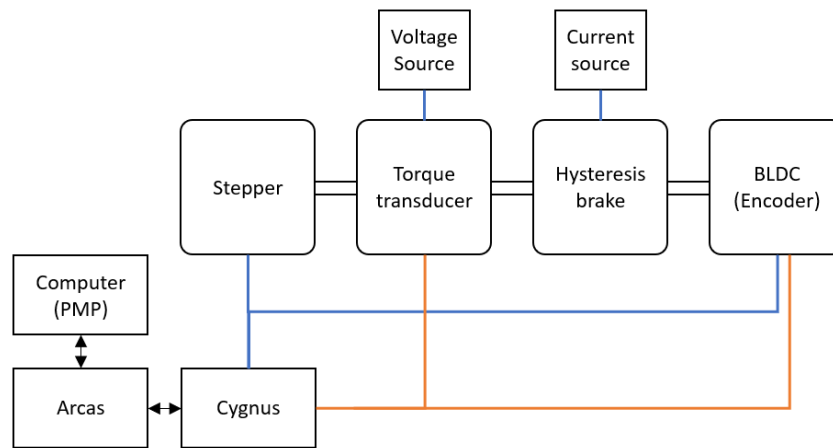
Figure 6.2: Test bench connections.
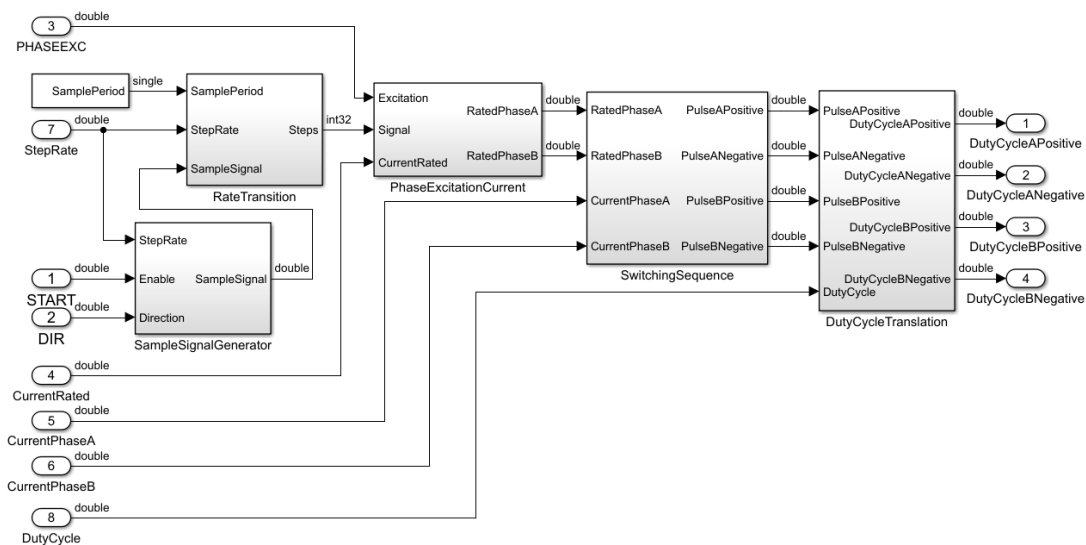
Figure 6.3: Test bench stepper motor driver.

Motor driving voltage for both stepper motor and BLDC motor are created through the Prodrive Cygnus board with pulse width modulation. The control signals are passed from the computer Prodrive Motion Platform (PMP) software to the Arcas sub-controller. Then the Arcas sub-controller passes such signals finally through the Cygnus to the motors. Current feedback is sensed at the Cygnus and fed back through Arcus to the PMP.

The full-step control algorithm is compiled from the MATLAB/Simulink environment and uploaded to the Arcus. The controlling algorithm is shown in Fig. 6.3.

Chapter 7

Results and Discussion

Stepper motors are often defined by their step response and motor curves [9]. Step response represents motor step-changing dynamics and shows the motor oscillation and kinetics. Motor curves represent the motor's physical limitations and characteristics at different operating speeds. Despite the step response and motor curves represent a stepper motor's characteristic, more than often, motor curves are the only characteristic the motor manufacturer provides. Therefore, step responses are compared within the simulated models, while the motor dynamic curves are compared among the model curves and manufacturer given curve.

The semi-analytical model is built with reference to the generalized electrical model. Non-linear parameters are obtained through measurements in Chapter 6 and estimated by the flux-based model curves. Two methods to obtain non-linear parameters are attempted:

- Non-linear parameters optimization without physical measurements,

- Non-linear parameter estimation with inductance and resistance measurements.

With a current-controlled constant-voltage driver applied, motor dynamic curves are obtained by applying different loads and voltages while limiting the current of the motor [38]. Since the mechanical model applied in the thesis does not include damping, the non-linear parameters are determined and optimized using the model without mechanical block shown in Fig. 5.19. The dynamics from NEMA17 motor (ST4209L1704) are first investigated. After the non-linear parameters for the semi-analytical model are determined, the realistic curves with the mechanical model and oscillation are attached again to obtain the resonance effects. Differences in the curve are discussed and validated. Then, three other motors were selected to compare their semi-analytical and generalized model dynamics.

7.1 Pull-out curve without mechanical block

The generalized electrical and flux-based model dynamics simulated without mechanical block are compared. The generalized electrical model is implemented with motor parameters from the datasheet and physical measurements, whereas the flux-based model is implemented with LUT from the FEA model. Both the step response and dynamic curves from the models are compared. Two sets of non-linear parameters for the semi-analytical model are determined based on optimization without physical measurements and estimation with measured inductance and resistance.

The $Theta_0$ in Fig. 5.19 is first set to $-0.45°$ for the ST4209L1704 motor since the relative rotor position from the current at 0 second shown in Fig. 5.20 is at the transition to the $-0.45°$ mechanical position. The average of the torque fluctuation is then calculated as the average torque experienced in the relative speed (in this case 60 rpm). Here, the average is taken continuously per step rate.

7.1.1 Generalized electrical model

The generalized electrical model motor curves are obtained. The motor parameters are mainly obtained from motor datasheet parameters shown in Fig. 3.1. The two values of physically measured 6mH inductance and 2.1Ω resistance from Chapter 6 are included as a comparison to the datasheet values.

By running the speeds from 37.5 to 3600 rpm, the output pull-out curves are shown in Fig. 7.1 and the torque errors are shown in Fig. 7.2.
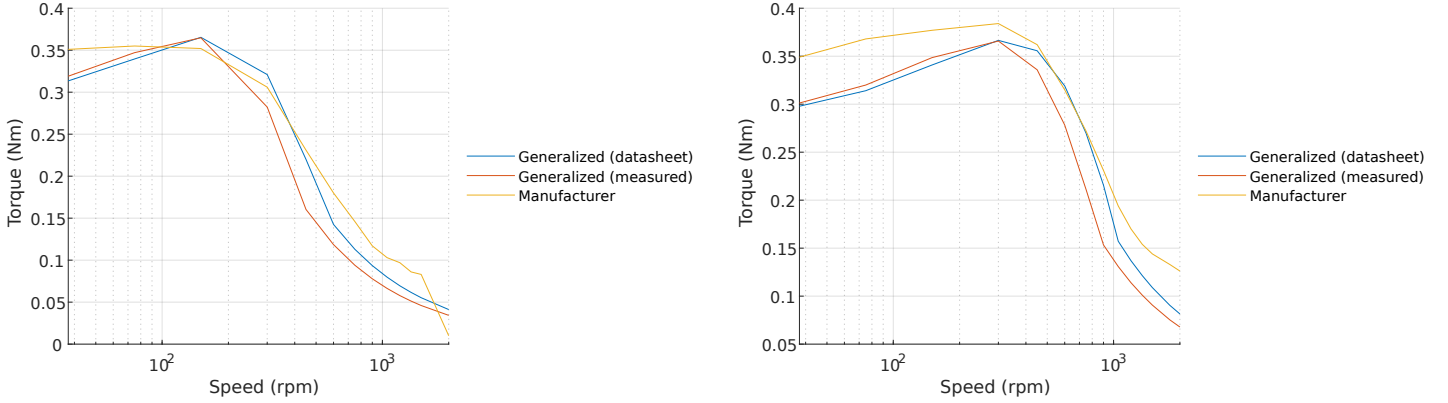

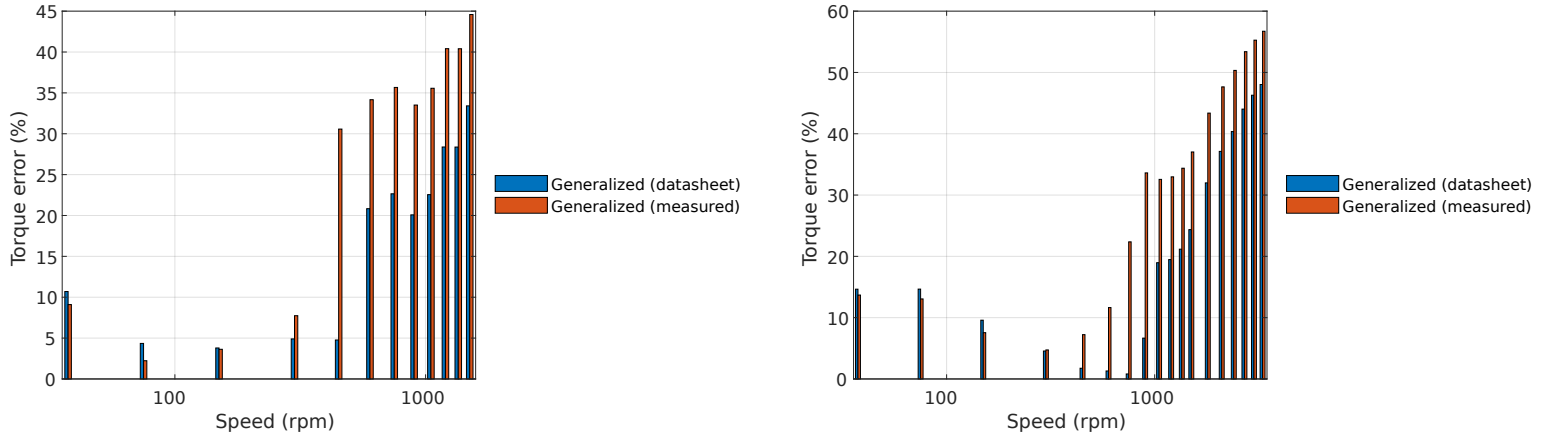Figure 7.1: Generalized model pull-out curves (left) 24V/1.63A (right) 48V/1.63A.

Figure 7.2: Generalized model pull-out errors (left) 24V/1.63A (right) 48V/1.63A..

As the speed increases, the torque error increases in both the 24V and 48V Simulation. As seen in Fig. 7.1, higher the speed, lower the torque production. The lower torque from the generalized electrical model in the constant-torque region is caused by the way torque is calculated. Since, in reality, torque is created based on the stepping changes, the averaging of torque from set continuous speed block does not take into account the real increase of position. The different motor start position $theta_0$ can be set to decrease the difference. However, since such error will slowly decrease as the speed increases and it is universally lower in the constant-torque region, it is ignored.

The decreasing-torque region follows the manufacturer curve with the lowest errors shown in Fig. 7.2. The generalized model curve with measured inductance and resistance has lower maximum torque because of the higher current increasing time from the higher inductance, the same in the high-speed region. Assuming the motor torque constant to be close to reality, the lower torque at the higher speed is then caused by a higher back-emf. Such higher back-emf decreases the motor current and therefore decreases the torque. Oppositely, considering the motor back-emf and inductance to be close to reality, the lower torque can then be caused by the linearized torque constant used in the generalized electrical model.

7.1.2 Flux-based model

The flux-based model pull-out torque is obtained. The output of both 24V and 48V driving voltages are shown in Fig. 7.3 and the errors of the two plots shown in Fig. 7.4.
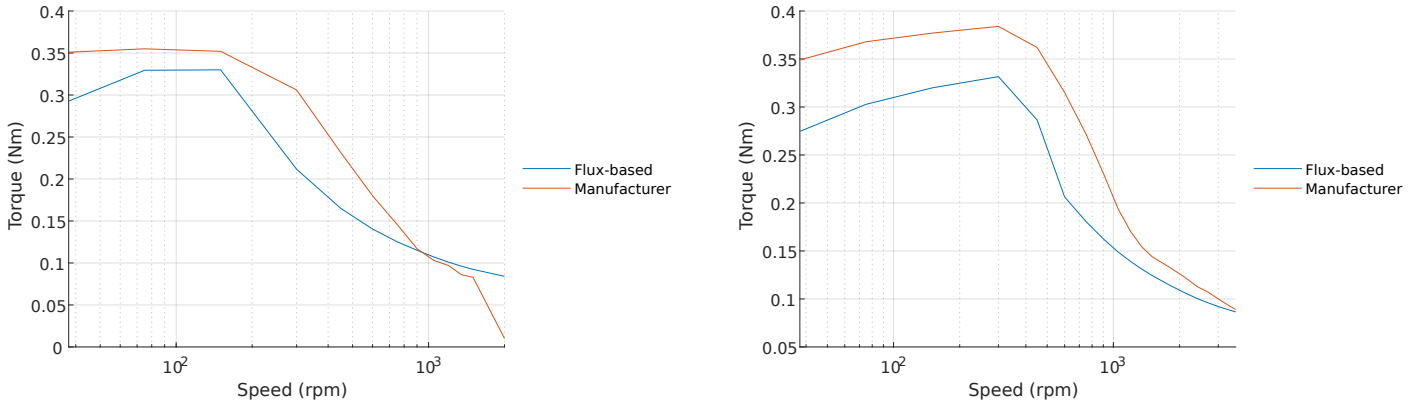
Figure 7.3: Flux-based model pull-out curve (left) 24V/1.63A (right) 48V/1.63A.
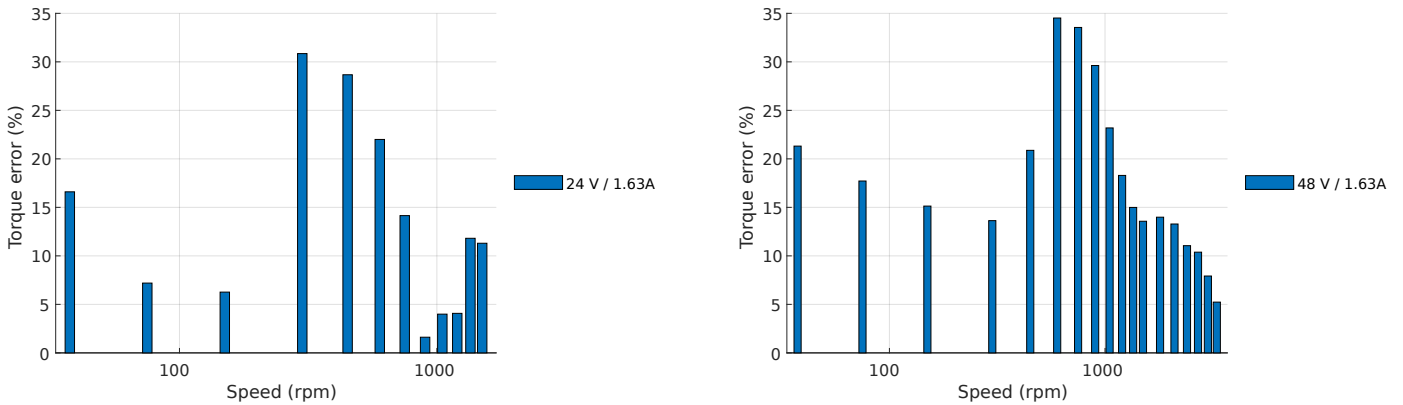
Figure 7.4: Flux-based model pull-out error.

As seen in both 24 and 48V, a higher error is in the decreasing-torque region (200 to 800rpm region in 24V and 400 to 100rpm region in 48V). Similar to the generalized model with measured inductance, since the FEA model has a higher inductance of 7.6mH shown in Fig. 3.30. Even slower current increase causes a lower peak current and lower torque production. An example is shown in Fig. 7.5, where the phase currents are triangular waves instead of square waves. This is due to the switching happening before the current reaches the rated current. As a result, the torque fluctuation increases as the linear current regions are not present anymore. Since the flux-base model intuitively considers the non-linear entities, the flux differences caused by the rotor position, stator pole structure, and current differences are translated into the torque fluctuations seen in Fig. 7.5. Since the torque fluctuation is present throughout all regions, higher average torque from the fluctuation leads to lower torque error in the higher speed region.
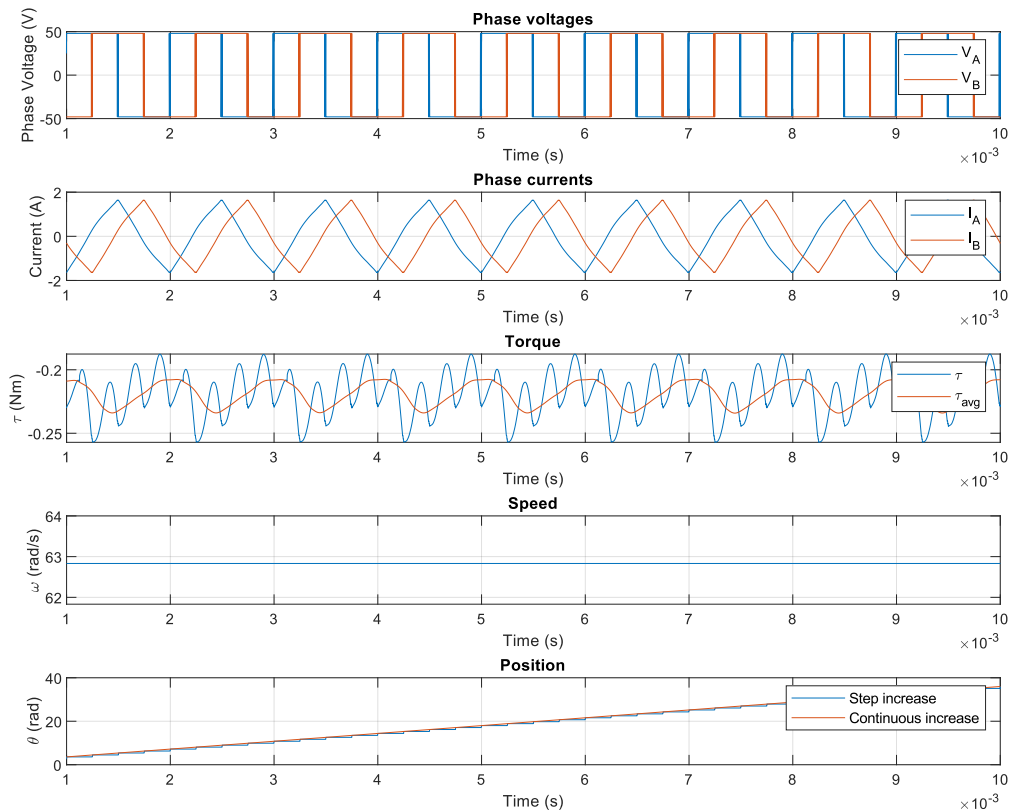
Figure 7.5: 48V flux-based model dynamics at 600rpm.

7.1.3   Model comparison

To estimate the semi-analytical model non-linear parameters: mutual inductance, detent torque inductance position dependency, and non-linear torque constant, the generalized electrical model curves are compared to the flux-based model curves. The three regions and their step responses are discussed. The torque fluctuations of these regions help to optimize the non-linear parameters without physical measurements. Without physical measurements, the inductance and resistance values are set to the datasheet values of 5mH and 1.6Ω.

Constant-torque region

A speed of 150rpm is selected to represent the constant-torque region. The input voltage, switching frequency, speed, and position of both models are the same. The phase currents and torque are compared at 48V and rated current shown in 7.6.
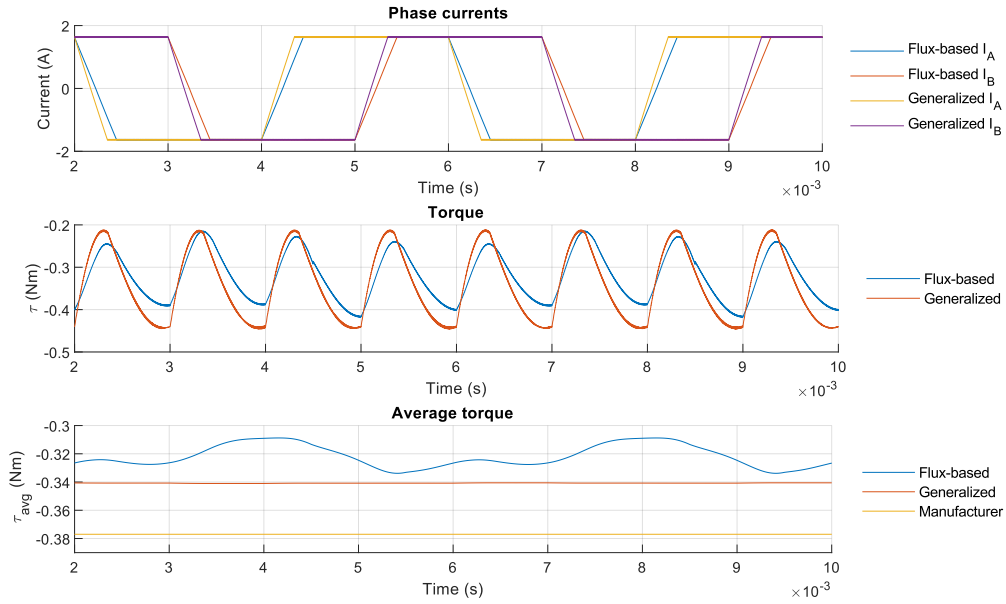
Figure 7.6: Flux-based and general electrical model at 150 rpm.

As seen in the phase currents of the figure, the phase currents increase slower in the flux-based model than the general electrical model. This slower rate is mainly caused by the higher inductance saw in the FEA model. The FEA model has an inductance of 6.7mH instead of 5mH given in the datasheet. While not taking this slower increase into account, another distinct dynamic in the flux-based model is the fluctuation with the position. A maximum fluctuation can be seen between 2.4 milliseconds and 3.3 milliseconds. Such fluctuation can be caused by the position dependence inductance in the FEA model. Therefore, such fluctuation proves that the position dependence is indeed a factor that can cause the pull-out torque to fluctuate. Yet, since the manufacture does not provide the torque-position relation, the comparison can only be done between the flux-based and generalized models. To achieve a higher average torque while taking into account the fluctuation, a mutual inductance and inductance fluctuation has to be taken into account in the semi-analytical model.

Another phenomenon that can be seen in both Fig. 7.6 is the inconsistent sinusoidal increase in torque when both phase currents are stable. With an ideal torque constant, the torque increases sinusoidally with the rotor position. Yet looking at the flux-based models, the increases are not consistent throughout the positions. This can be caused by the non-linear torque constant in the FEA model.

Decreasing-torque region

The decreasing-torque region is represented with 600rpm simulation. With the same 48V driver and rated current, the curves are shown in Fig. 7.7.
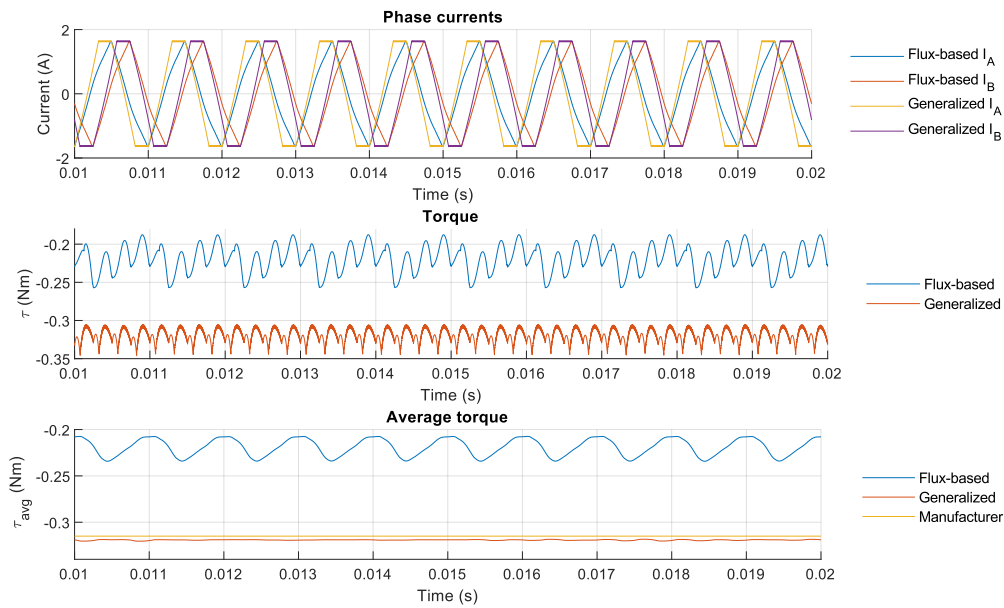
Figure 7.7: Flux-based and general electrical model at 600 rpm.

The effect of the higher inductance in the FEA model can be seen again in the phase currents. An example can be seen at time 0.011 second of the flux-based model, where the phase B current couldn't achieve the rated current before the driver switched off. Another non-ideal property can be seen also in the same curve at 0.013 seconds of phase A current. A slope change can be seen in the figure. Such slope change is mainly caused by the saturation in the FEA simulation motor when the flux at a current level is not achieved because of the material saturation. Since the flux-based model uses the inverted flux LUT, the saturation can, therefore, be seen in the current. Since magnetic flux is equal to the product of current and inductance are shown in Eq. 4.16, the saturation is therefore a part of the inductance matrix.

High-speed region

The high-speed region is simulated to be the region above 1000 rpm in the ST4209L1704 motor. The motor running in such a region could not achieve the rated current because of the fast switching, back-emf, and motor inductance. In such a region the torque is reduced also because of the lower current. The 1500rpm 48V dynamics are shown in Fig. 7.8.

Figure 7.8: Flux-based and general electrical model at 1500 rpm.

At 1500 rpm, the current is about 0.4 Amps lower with the flux-based model. Yet, the output torque in the flux-based model is higher than that of the generalized model. This can be caused by the incorrect material saturation from the generalized electrical model. Lower saturation translates to h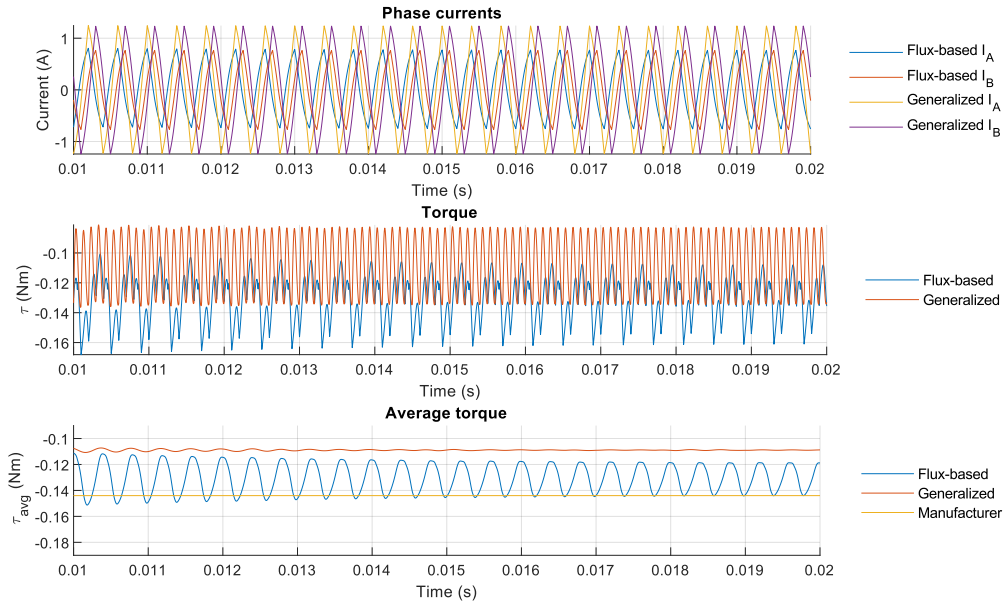igher torque, vice versa. Also, as seen in the current and torque plots, the torque fluctuates base on the position dependencies. Hence, at higher speeds, the non-linear entities that depend on the position and saturation can affect the pull-out torque ratings or motor performance.

7.1.4 Semi-analytical model

To simulate the pull-out curves from the semi-analytical model, mutual inductance M, position-dependent inductance peak L_1, detent torque harmonics, and second-order non-linear torque constant a have to be defined. The two methods with and without measured parameters are obtained.

Estimation with inductance and resistance measurements

The non-linear parameter estimation relies on the physical measured motor parameters. The inductance and resistance measurements in Chapter 6 is applied instead of the datasheet parameters. Nonetheless, the mutual inductance is also directly applied from the LCR meter measurement. Both the mutual inductance and torque-current non-linear constants are estimated from the FEA model simulation. The position-dependent inductance is also set to be less than 5% of the rated inductance [33]. The non-linear parameter values and ranges are shown in Table 7.1.

Table 7.1: Non-linear parameters value and ranges estimated from measurements and FEA.

Parameter	Description	value	Unit
L	Motor inductance	6	[mH]
R	Motor resistance	2.1	[Ω]
M	Mutual inductance	$0.05 \sim 0.3$	[mH]
L_1	Position dependent inductance	< 0.25	[mH]
T_{dm}	Detent torque harmonics	2nd+4th	[-]
a	TI non-linear curve	≈ -0.048	[-]

Optimization without measured parameters

Another method to estimate the non-linear parameters for the semi-analytical model is proposed. The parameters are estimated both by observing the movements of the pull-out torque with various non-linear parameter inputs and considering the flux-based model step responses. Four non-linear parameters are shown in Section 5.2.3 are discussed with various possible ranges. The parameters are determined based on the 48V analysis. Then, the 24V analysis is simulated.
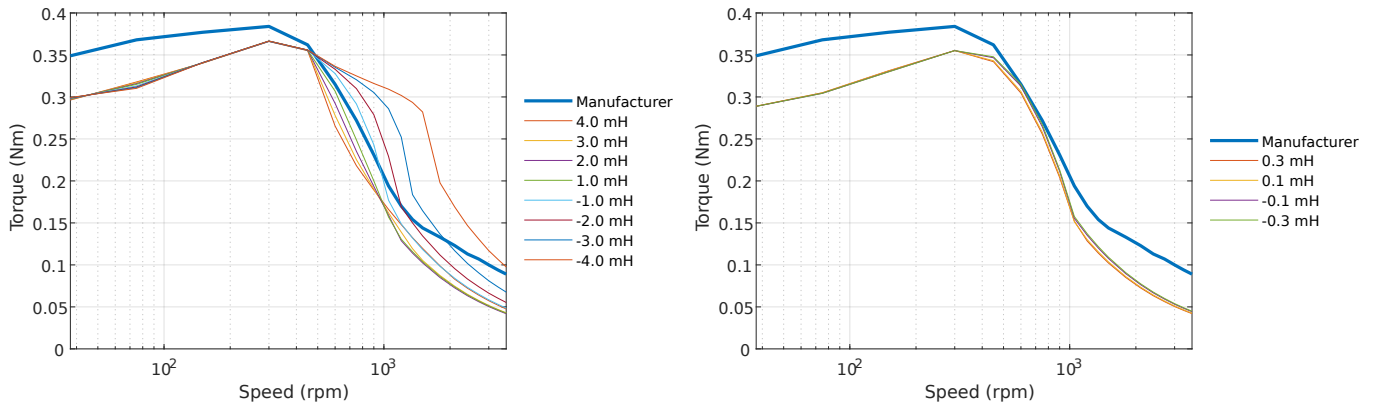

Figure 7.9: Pull-out curves with various parameter values (left) mutual inductance (right) inductance position dependency.
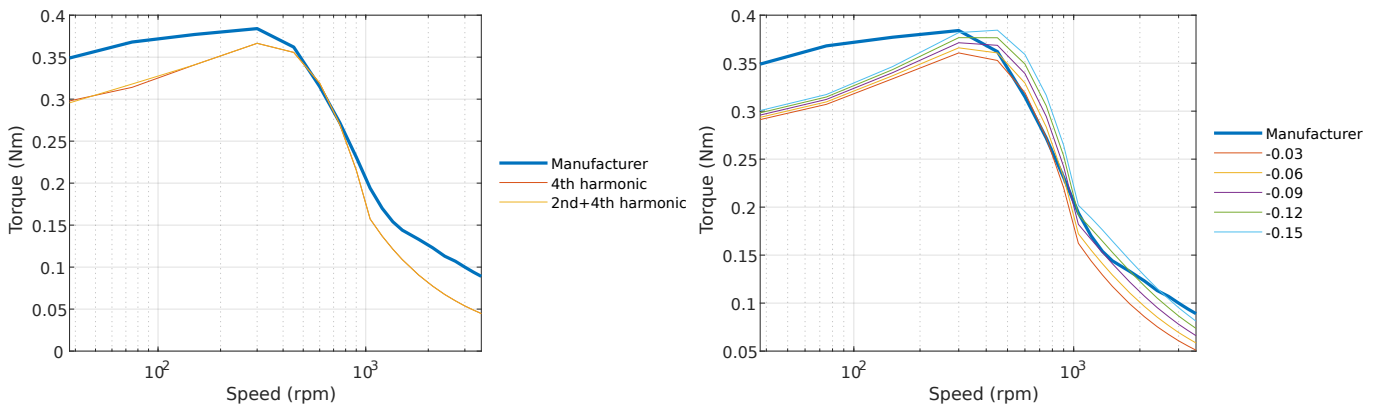
Figure 7.10: Pull-out curves with various parameter values (left) detent torque 2nd harmonic (right) non-linear torque constants.

The mutual inductance is shown in Fig. 7.9 (left) is applied with multiple levels. The pull-out curves are obtained with mutual inductance value from -4mH to 4mH. Here the maximum mutual inductance amplitude 4mH is chosen to be close to the motor inductance because, with different motor teeth designs, the mutual inductance from a stepper motor can be as high as the motor inductance [39]. Since the mutual inductance of the motor is dependent on the two-phase interactions, the direction of the current induced between phases can alter depending on the coil winding direction. Since phase A of a 2-phase hybrid stepper motor is neighbored by two reversing phase B coils, B+ and B-, the total motor mutual inductance are summed up from each phase's positive and negative coils. The mutual inductance can therefore also be negative [39]. An important feature that can be seen in Fig. 7.9 (left) is that the inductance is mainly affecting the decreasing-torque and high-speed regions. A more negative mutual inductance shifts the whole curve toward higher speed regions. This is because the negative inductance reduces the time for the current increase, hence creates a higher average current and torque at certain voltage levels. On the opposite, a higher positive mutual inductance creates a higher and more universal decreasing slope in the decreasing-torque and high-speed regions.

The position-dependent inductance is applied with several position dependency peak value L_1 shown in Fig. 7.9 (right). The position-dependent inductance change can also be in the negative and positive regions depends on the motor setup and motor pole arc geometry [40]. Unlike the mutual inductance, the position-dependent inductance of a hybrid stepper motor is often less than 5% of the rated inductance shown in Fig. 4.5 [33]. As seen in Fig. 7.9 (right), the curve does not alter significantly. Position dependency does not affect the pull-out torque as significantly as the mutual inductance.

The 2nd harmonic in the detent torque is applied in addition to the 4th harmonics shown in Fig. 7.10 (left). Although a small difference can be seen in the constant-torque region, the change is insignificant. For example, a 0.004Nm increase at 75 rpm is only a 1.2% increase from the peak torque. Such pull-out curve output is unlike what is suggested in [38] that torque will decrease more significantly at a higher speed. This can be caused by the significance of detent torque compared to the holding torque. Such that, the detent torque in ST4209L1704 is only 3% of its holding torque, much lower than the stated 5 to 20% in [38].

The TI-curve constant a is tested with several numbers. Since lower saturation in the FEA model can cause a higher torque and lower current shown in Fig. 7.8, the TI-curve is tested from pure linear to fully saturated shown in Fig. 7.11.
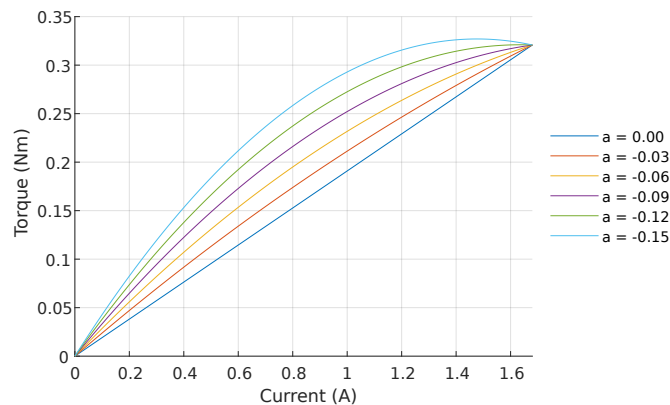

Figure 7.11: Non-linear torque-current curves with different constants.

Shown in Fig. 7.10 (right), a more negative a means a faster motor saturation. With decreasing a constant, peak torques at lower speeds experienced fewer increases than that of the higher speeds because, at lower speeds, motor rated torque is always achieved. This means higher torque-current slope from lower currents is not dominant. Such a phenomenon reduces the torque increase at low speed in Fig. 7.10 (right). Vice versa, at higher speeds, the torque-current curve shown in Fig. 7.11 creates a higher peak torque because of the higher slope that is experienced at lower currents.

Several rules toward parameter optimization are applied. Firstly, the position dependency is set to be positive and lower than 5% of the datasheet inductance. Secondly, the mutual inductance parameter is selected to be in the positive region following the curves shown in Fig. 7.9 (left). Lastly, since position-dependent inductance and detent torque 2nd harmonic produce insignificant changes to the pull-out torque, they are chosen after the mutual inductance and TI-curve are selected.

Results

The results from both methods are compared and validated. Final parameter combination selected is shown in Table 7.2. Non-linear parameters estimated from the measured parameters are selected based on the limitations in Table 7.1. Likewise, a parameter combination from optimization without measured parameters is chosen through both try-and error and from waveform comparisons shown in Section 7.1.3 to better fit the manufacturer given pull-out curve and step responses.

Table 7.2: Semi-analytical model parameters.

Parameter	Description	Optimized	Measured/FEA	Unit
R	Motor resistance	1.8	2.1	[Ω]
L	Motor inductance	5	6	[mH]
M	Mutual inductance	2	0.1	[mH]
L_1	Position-dependent inductance	0.05	0.2	[mH]
T_{dm}	Detent torque harmonics	2nd+4th	2nd+4th	[-]
a	TI non-linear curve	-0.15	-0.048	[-]

The 24V and 48V semi-analytical pull-out curves compared to the manufacturer given curves are shown in Fig. 7.12. In the semi-analytical curves that consist of measured non-linear parameters, the motor dynamic curves are lower than the manufacturer curves. Since it is very hard to know the actual inductance and resistance of the specific motor the manufacturer tested on, lower torque is caused by the realistic motor inductance and resistance that is measured from the physical motor. Also, with a limited amount of change allowed with the measured non-linear parameters, the model has to be further validated with the mechanical model attached. Nonetheless, the non-linear parameters of the semi-analytical model without any measured parameters can be optimized to fit the manufacturer curve very well. However, since it is optimized under a wide range of values, the values can be unrealistic if not further validated.
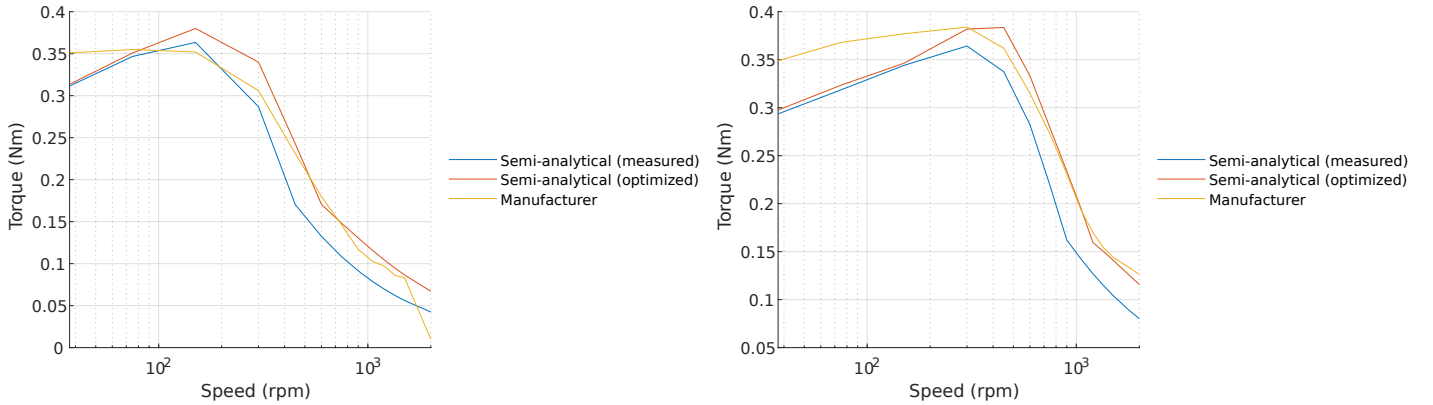
Figure 7.12: Semi-analytical model pull-out curve comparisons from two sets of non-linear parameters (left) 24V (right) 48V.

The maximum and average errors of the 24V and 48V curves are shown in Tables 7.3 and 7.4. The table showed that the motor accuracy with semi-analytical curves indeed increased with both the measured and optimized non-linear parameters. The semi-analytical model with the measured non-linear parameter, motor inductance, and motor resistance increased by a maximum of 12.1% compared to the generalized electrical model with measured inductance and resistance. Similarly, the semi-analytical model accuracy with pure datasheet parameters and optimized non-linear parameters increased by a maximum of 29.9% compared to the generalized electrical model without measured inductance and resistance.

The semi-analytical model with measured parameters has less accuracy compared to the one without. This is caused by the higher physically measured inductance that can already be seen in Fig. 7.2. Furthermore, because the optimization of non-linear parameters has a wider possible range than the measured values, it is possible to achieve higher accuracy when there is a mismatch between measured values and actual motor values. An overall higher error seen in the 48V model is caused by the lower simulated torque in the constant-torque region. Such error is also in the generalized electrical model and is caused by the $theta_0$ applied in the model.

Table 7.3: Models error comparison at 24V.

Model	Average error	Maximum error
Semi-analytical (measured)	19.6%	32.5%
Generalized electrical (measured)	26.5%	44.6%
Semi-analytical (optimized)	7.4%	12.7%
Generalized electrical (datasheet)	17.1%	33.4%
Flux-based	14.9%	30.5%

Table 7.4: Models error comparison at 48V.

Model	Average error	Maximum error
Semi-analytical (measured)	25.7%	47.1%
Generalized electrical (measured)	31.0%	56.7%
Semi-analytical (optimized)	7.7%	18.1%
Generalized electrical (datasheet)	21.4%	48.0%
Flux-based	8.8%	23.9%

The semi-analytical step responses in the constant-torque, decreasing-torque, and high-speed regions are also compared with the flux-based model dynamics. Three speeds of 150, 600, and 1500 rpm are presented. The 48V model is compared. Four motor steps are shown.

- 150 rpm:
  The 150 rpm current and torque dynamics are shown in Fig. 7.13. Here the torque from both semi-analytical models also experienced fluctuations similar to that of the flux-based model. Such fluctuation is indeed caused by mutual inductance. The output average torque, therefore, has a very similar oscillation to the flux-based model. The higher peak of -0.2 Nm in the optimized semi-analytical model is caused by higher mutual inductance.
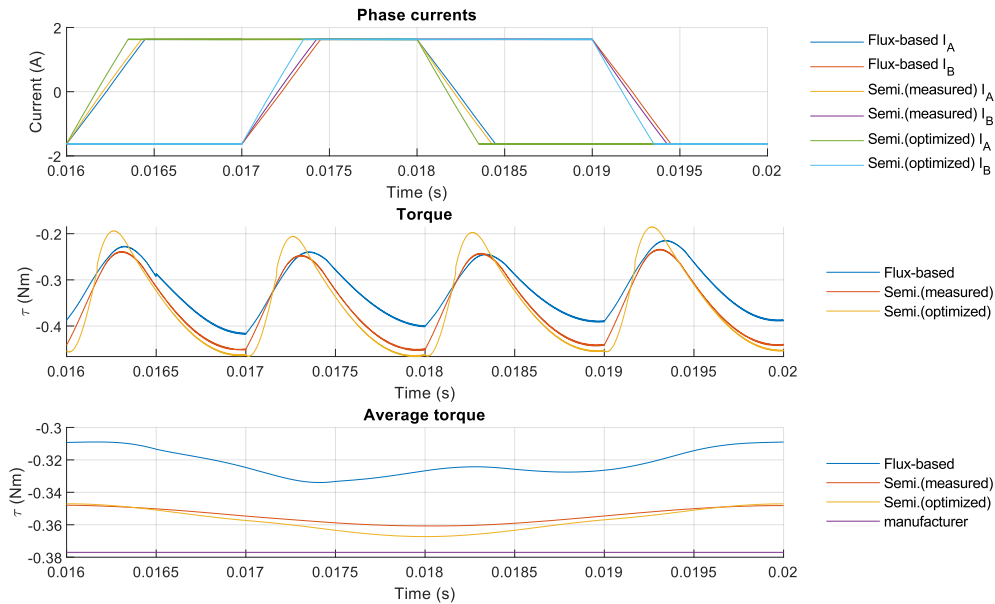
Figure 7.13: Semi-analytical and flux-based model at 150 rpm.

- 600 rpm:
  The 600 rpm current and torque dynamics are shown in Fig. 7.14. Here, the torque oscillation can

still be seen. However, the average torque of both semi-analytical models is much higher than that of the flux-based model. They are closer to the datasheet because of the TI-curve that is applied in the semi-analytical models.
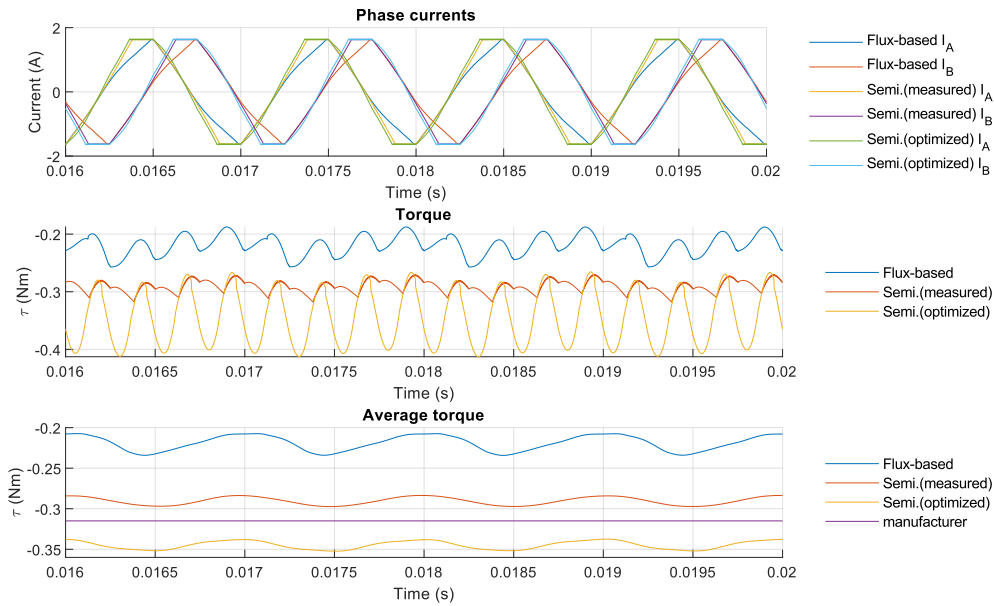
Figure 7.14: Semi-analytical and flux-based model at 600 rpm.

- 1500 rpm:
  The 1500 rpm current and torque dynamics are shown in Fig. 7.15. At higher speed, both semi-analytical torque fluctuations are more visible and exist like the flux-based model. The measured semi-analytical model experienced the lowest average torque because of the more linear torque-current constant and lower maximum current. With a faster saturated torque-current constant and higher mutual inductance, such as in the optimized semi-analytical model, higher torque can be achieved.
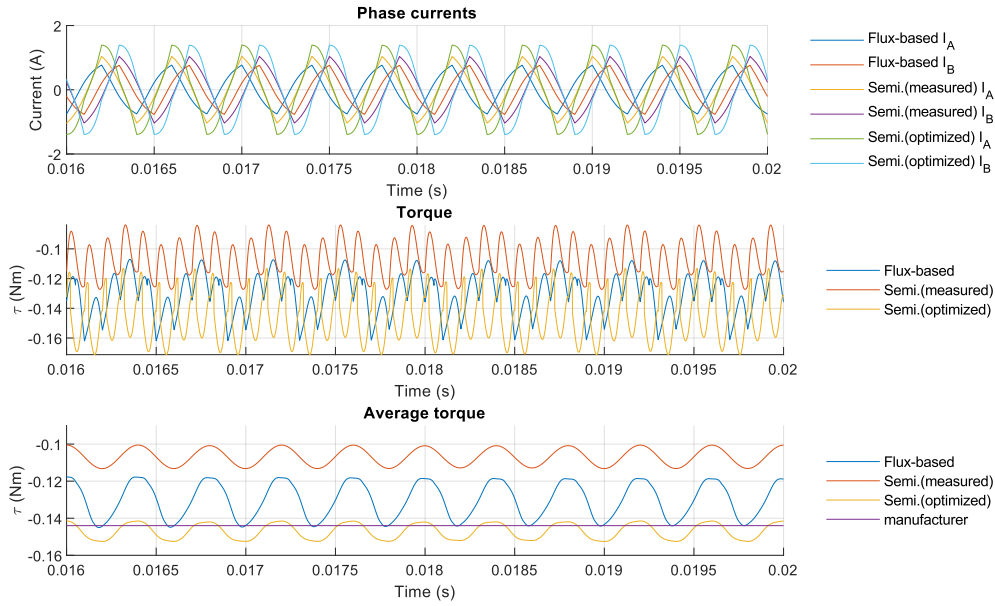
Figure 7.15: Semi-analytical and flux-based model at 1500 rpm.

7.2 Pull-out curve with mechanical block

With the non-linear parameters selected in Table 7.2, the mechanical block is then connected back to include the mechanical phenomenons. The pull-out torque with a mechanical block is simulated and compared between the generalized electrical model and both semi-analytical models. Since the mechanical model is dependent on the mechanical constants such as inertia and damping constant, it is therefore important to estimate such constants. Mechanical constants are shown in Table 7.5.

Table 7.5: mechanical parameters.

Parameter	Description	Unit
D_m	Viscous damping constant	[Nms/rad]
C_m	Coulomb damping constant	[Nm]
J_{load}	Load inertia	$[Kgm^2]$

The D_m and C_m defines the mechanical damping experienced by the motor. Since such coefficients are not given in the motor parameter, they are estimated. The C_m is set to zero since it is comparably smaller than D_m [9]. D_m is calculated based on the following equation that equates the rotor viscous damping to be equal to one to ten percent of the holding torque [37]. The equation is expressed as

$$D_m = \frac{T_{rated} \times (0.01 \sim 0.1)}{StepRate \cdot \Theta \cdot \frac{\pi}{180}}. \tag{7.1}$$

The D_m is chosen to be 1e-4 Nms/rad with such an equation. Moreover, since J_{load} is always dependent on the loading profile and the mechanical setup, it will first be set to zero. Yet, with a physical testbench, it can be set as the sum of all inertia in the mechanical system.

The semi-analytical curve simulated with measured non-linear parameters are compared to the manufacturer given curve and the generalized electrical model curve simulated with measured inductance and resistance. Similarly, the semi-analytical curve optimized without measured parameters are compared to the manufacturer given curve and generalized electrical model curve simulated with datasheet parameters. The accuracy of both models is discussed. The comparisons are shown in Fig. 7.16 and Fig. 7.17.
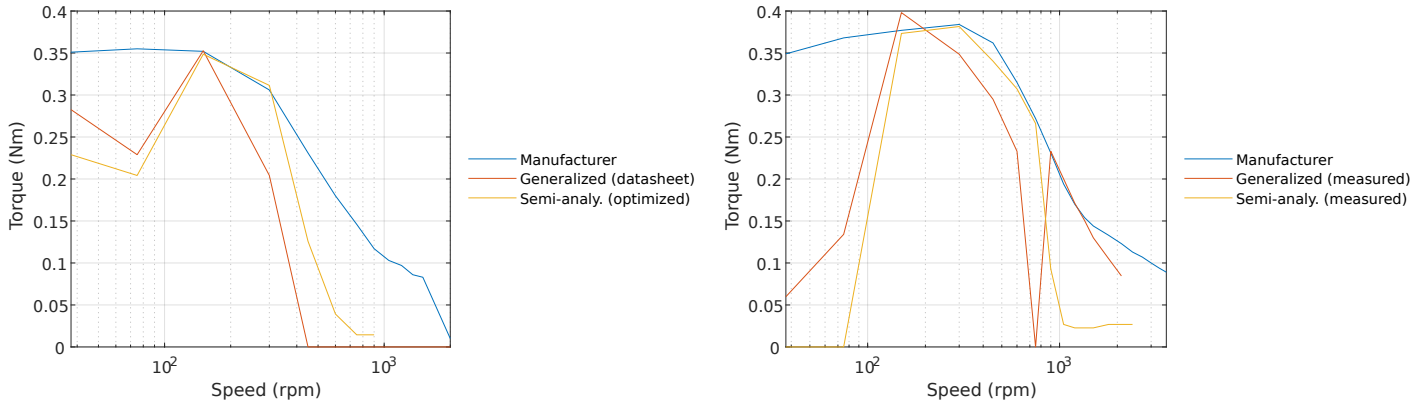
Figure 7.16: Semi-analytical pull-out curve optimized without measured parameters with mechanical block (left) 24V (right) 48V.
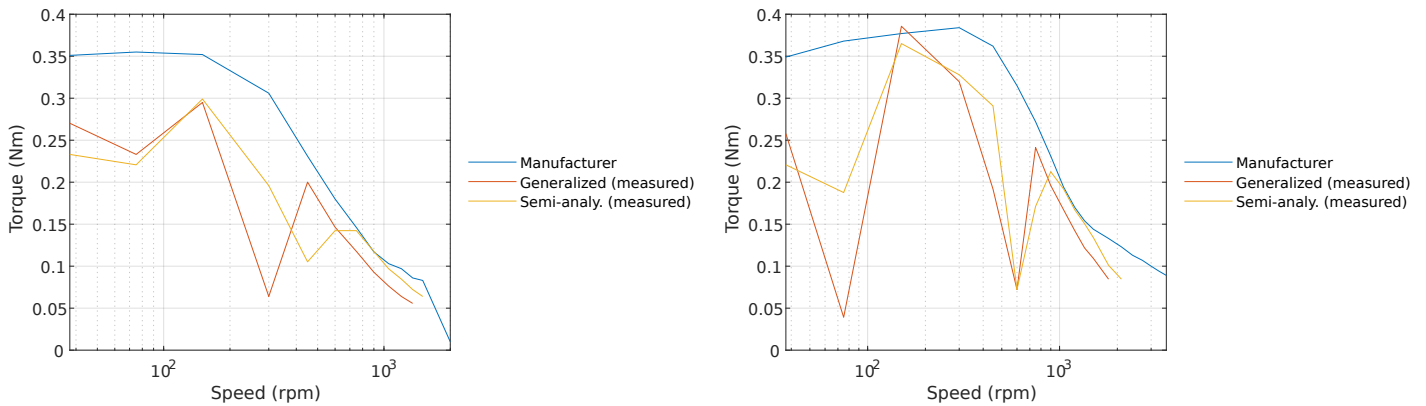

Figure 7.17: Semi-analytical pull-out curve estimated with measured parameters with mechanical block (left) 24V (right) 48V.

As seen in the manufacturer given and both semi-analytical curves, the resonance frequencies shown in Fig. 4.7 can be clearly identified. The mechanical and electrical dips are present.

The optimized semi-analytical pull-out curve shown in Fig. 7.16 fits the manufacturer given curve better in the less-oscillatory regions from 150 to 900 rpm of the 48V models and 150 to 300 rpm of the 24V models. However, there is a clear indication that the electrical dips are shifted and high speeds are not achievable. Such a phenomenon is not expected since the non-linear parameters are mainly the effect of mechanical geometries, which only causes the mechanical dip at lower speeds. With the same electrical drive used in all models, such a shift in electrical dip can be an indication of incorrect optimization.

The measured semi-analytical pull-out curve shown in Fig. 7.17 has a general small torque increase from the generalized electrical model curve. Higher torques are visible at 300rpm of 24V and 450rpm of 48V. Different from the curve simulated with optimized non-linear parameters, the measured model fits the high-speed region better. This can be an indication that, although the curve is not perfectly fitted onto the manufacturer given curve, the semi-analytical model is more accurate at all speeds. The overall lower torques compared to that of the manufacturer given curves because of a possible lower inductance the manufacturer tested motor has.

7.3 Pull-in curve

Pull-in torque, where the maximum torque to start the motor from a standstill, is also an essential characteristic that defines a stepper motor. Therefore, the pull-in curve of the ST4209L1704 motor is

also simulated. However, since the pull-in curve is seldom provided by the manufacturer, the obtained pull-in torque is presented with the relative pull-out torque from the semi-analytical model.

With D_m being set to 1e-4 Nms/rad, C_m to zero, and J_{load} to zero (no load), the pull-in curves are obtained as shown in Fig. 7.18 and Fig. 7.19. The pull-out curve from the manufacturer is being added as a reference.
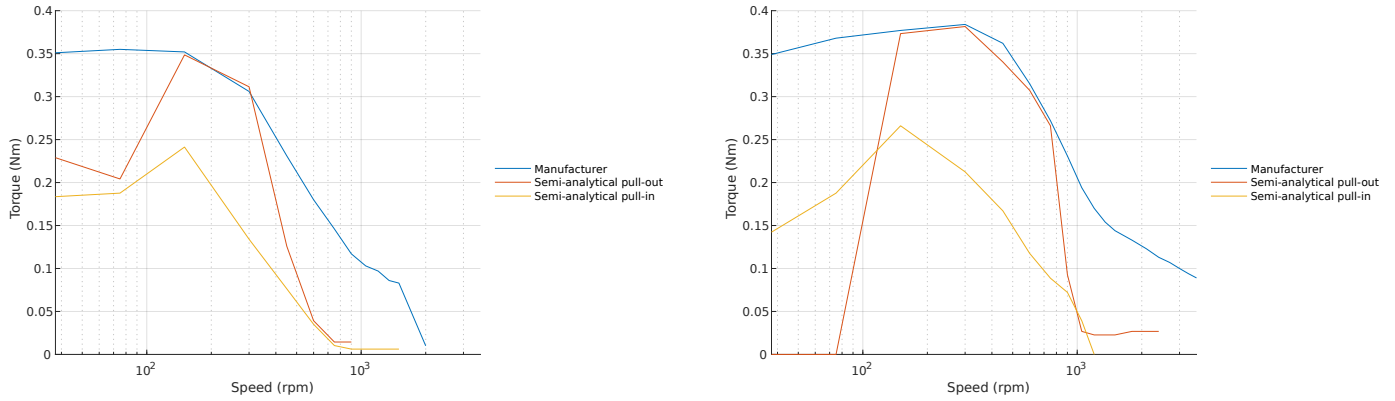
Figure 7.18: Semi-analytical pull-in curve optimized without measured parameters with mechanical block (left) 24V (right) 48V.
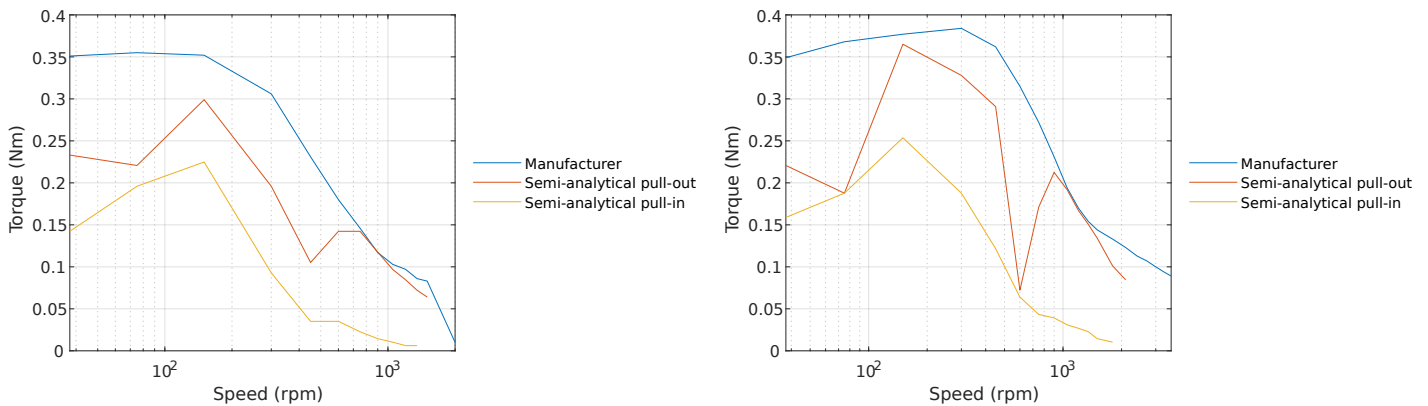
Figure 7.19: Semi-analytical pull-in curve estimated with measured parameters with mechanical block (left) 24V (right) 48V.

As seen in both Fig. 7.18 and 7.19, the peak torques in the pull-in curves are indeed lower than that of the pull-out curves. This validated that stepper motors are indeed not able to start after certain speeds. The max self-start frequency defines the maximum frequency the motor can start. Nonetheless, the dips showed in Fig. 4.7 are also present in the pull-in curves. These phenomenons can be seen in both 24V and 48V.

An unusual phenomenon can be seen in the low-speed region of Fig. 7.18 48V graph. When a pull-in curve can achieve non-zero peak torque at a lower speed, the motor should have a pull-out torque higher than that of the pull-in curve. However, the graph shows that the motor pull-out curve is lower than that of the pull-in curve. Such a phenomenon is caused by the pull-in unable to start region shown in Fig. 4.7 and the algorithm for pull-out torque. Since the pull-out torque always starts the motor from zero speed, it won't be able to pass the pull-in unable to start region although the motor is indeed able to run at a higher torque at that speed. The pull-in algorithm can detect such higher torque because the algorithm starts at the midpoint of rated torque and zero. This directly passes the pull-in unable to start region.

7.4   Other motors

To validate whether the semi-analytical model can also be applied to other bipolar 2-phase hybrid stepper motors, three motors of ST5909M2008-A, ST4118M1206-A, and MS17HD2P4150 are simulated for the pull-out curve without mechanical blocks. The mechanical block is disconnected to simplify the optimizing of non-linear parameters in the semi-analytical model. The generalized model, semi-analytical, and manufacturer given curves are compared. The three motors with each of their model parameters are shown in Table 7.6. The manufacturer given curves from these motors are all ran under a two-phase excited driver shown in Fig. 2.14 (b).

Table 7.6: Test motors.

Parameters	ST5909M2008-A	ST4118M1206-A	MS17HD2P4150	unit
Step angle	0.9	1.8	1.8	[°]
Rated voltage	3.6	5.27	2.97	[V]
Rated current	1.41	0.85	1.5	[A]
Phase resistance	3.6	6.2	1.98	[Ω]
Phase inductance	18	11.6	4.3	[mH]
Holding torque	1.05	0.396	0.5	[Nm]
Inertia	3e-5	5.7e-6	5.7e-6	$[Kgm^2]$
Detent torque	0.04	0.0098	0.015	[Nm]
Back-emf (at 300rpm)	23	N/A	N/A	[V]

An important aspect while applying parameters from different motors is that many of them do not provide the back-emf measurement. This means that the back-emf has to be estimated. Since single-phase, voltage constant can be estimated to be the same as single-phase torque constant under ideal condition [41]. The torque constant is directly calculated from rated torque and applied instead of from back-emf measurement.

Moreover, the higher errors at lower speed in ST4209L1704 motor shown in Fig. 7.1 is caused by the difference between the estimated step increase from $Theta_0$ and the real motor step increase from manufacturer physical pull-out curve tests. Such a stepping difference translates to the difference between manufacturer curves and MATLAB/Simulink simulated curves at lower speeds. Such a difference does not cause a big difference at the higher speeds because the switching became much faster than the constant current region is not possible anymore. Therefore, to test the different motors, $Theta_0$ applied in Section 7.1 should be applied with different variables that produce the highest average torque from the misalignment. However, since more numbers of $Theta_0$ means more simulation when the simulations are running in discrete simulations, only three $Theta_0$ of StepAngle/2, StepAngle/4, and 0 is applied. Then the highest torque is selected after the simulations.

7.4.1   ST5909M2008-A

The motor is simulated with the non-linear parameters shown in Table. 7.7. The parameters are obtained through trial-and-error on the 48V model and then applied to the 24V model for validation. The errors of the semi-analytical model are shown in Table. 7.8 and the curves are shown in Fig. 7.20.

Table 7.7: ST5909M2008-A semi-analytical model parameters.

Parameter	Description	value	Unit
M	Mutual inductance	8	[mH]
L_1	Position dependent inductance	0.5	[mH]
T_{dm}	Detent torque harmonics	2nd+4th	[Nm]
a	TI non-linear curve	0	[-]

Table 7.8: ST5909M2008-A model error comparison.

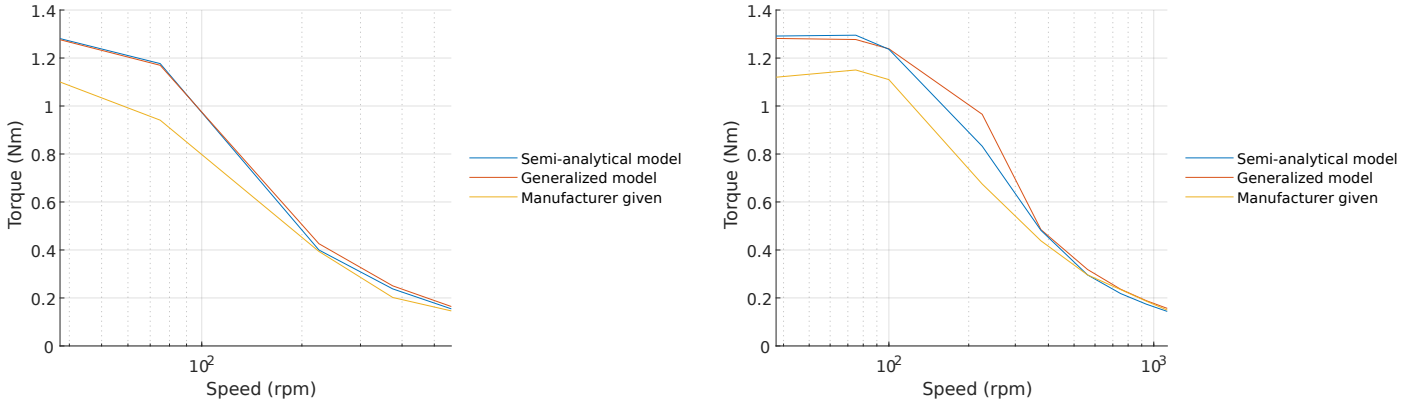| Model	average error	maximum error
48V semi-analytical	10.8%	23.4%
48V generalized electrical	12.4%	42.9%
24V semi-analytical	15.2%	25.1%
24V generalized electrical	18.1%	24.3%

Figure 7.20: ST5909M2008-A pull-out curves without mechanical block (left) 24V (right) 48V.

Both the 24V and 48V semi-analytical model accuracy increased by a small amount of 1.6% and 2.8%. Most likely, this motor has a high mutual inductance. With the mutual inductance parameter, the model has a higher similarity to the manufacturer pull-out curve. Yet, a higher error in the constant-torque and decreasing-torque regions can be an indication of an inaccurate datasheet inductance is used. With the optimization, setting the TI-curve parameter to zero indicates that, since the torque-current curve is set to linear, the saturation of the motor is most likely not saturated at the rated current. Additionally, the higher errors in the constant-torque region can be affected by the method manufacturers obtain the motor pull-out torque.

7.4.2 ST4118M1206-A

The ST4118M1206-A parameters are chosen and shown in Table 7.9. Nonetheless, errors and curves are shown in Fig. 7.21.

Table 7.9: ST4118M1206-A semi-analytical model parameters.

Parameter	Description	value	Unit
M	Mutual inductance	8	[mH]
L_1	Position dependent inductance	0.7	[mH]
T_{dm}	Detent torque harmonics	4th	[Nm]
a	TI non-linear curve	0	[-]

Table 7.10: ST4118M1206-A model error comparison.

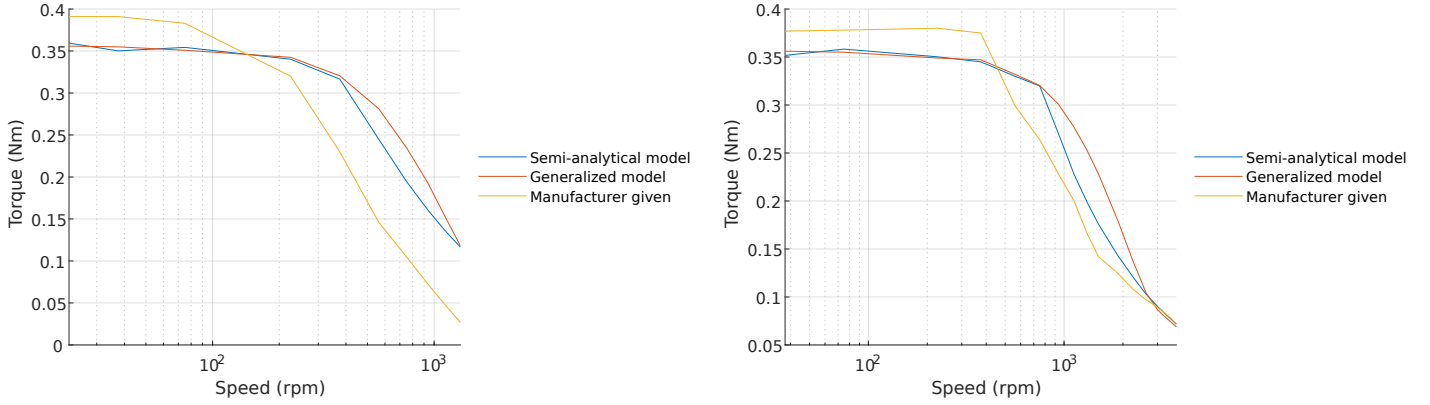| Model	average error	maximum error
48V semi-analytical	11.3%	23.8%
48V generalized electrical	22.0%	60.6%
24V semi-analytical	59.1%	187.1%
24V generalized electrical	75.3%	221.8%

Figure 7.21: ST4118M1206-A pull-out curves without mechanical block (left) 24V (right) 48V.

Both the 24V and 48V motor have average accuracy increases of 10.7% and 16.2%. The maximum possible optimization is achieved since the low-speed region is considerably stable and not changing with the non-linear parameters on the 48V model. However, the error in 24V is much higher than that of the 48V model. Since the parameters are optimized on the 48V model, an incorrect optimization in certain parameters can cause such high error in the 24V model. Additionally, errors can be seen to be much higher than before. This can be caused by the estimation of torque and voltage constants. Since the motor is not ideal, the two constants are not the same. While the manufacturer did not provide the back-emf measurements, both the voltage constant Kv and torque constant Kt are replaced with Kt.

7.4.3 MS17HD2P4150

The MS17HD2P4150 parameters are chosen and shown in Table 7.11. This motor has a bifilar motor structure but is ran with a bipolar setup. Nonetheless, errors and curves are shown in Fig. 7.22. Here, an additional change that had been made was the correction in torque constant. Since the voltage constant is not provided, the torque constant applied for both voltage and torque constant shown in Fig. 7.22 is too high. Therefore, the constant is first reduced before the optimization for non-linear parameters.

Table 7.11: MS17HD2P4150 semi-analytical model parameters.

Parameter	Description	value	Unit
Preset Kt	curve fit Kt	0.2	[Nm/A]
M	Mutual inductance	3	[mH]
L_1	Position dependent inductance	0.1	[mH]
T_{dm}	Detent torque harmonics	4th	[Nm]
a	TI non-linear curve	-0.1	[-]

Table 7.12: MS17HD2P4150 model error comparison.

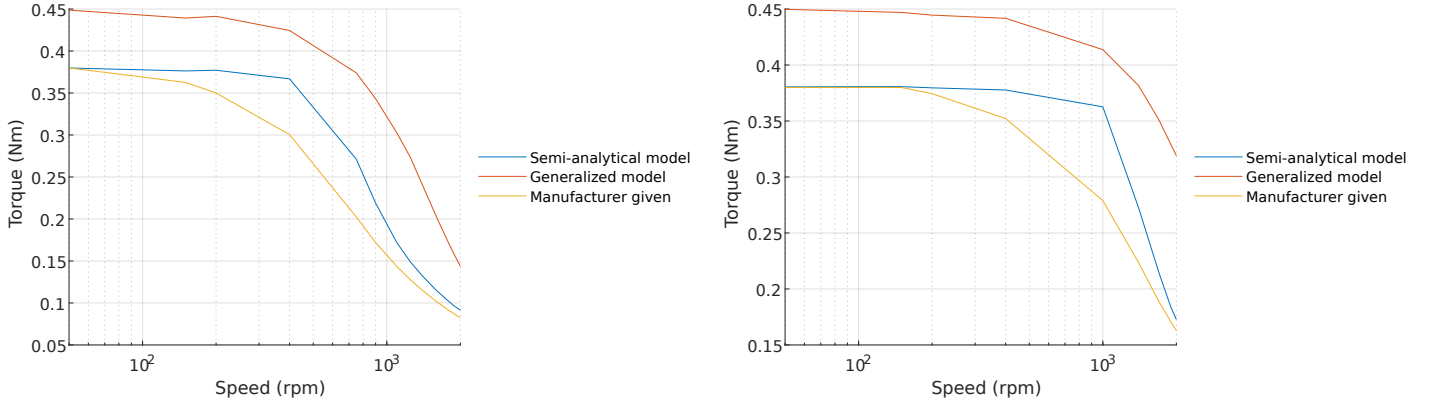| Model	average error	maximum error
48V semi-analytical	10.3%	30.0%
48V generalized electrical	24.5%	61.3%
24V semi-analytical	15.1%	34.0%
24V generalized electrical	43.8%	75.7%

Figure 7.22: MS17HD2P4150 generalized electrical model without mechanical block pull-out curves (left) 24V (right) 48V.

The 24V and 48V models have average accuracy increases of 14.2% and 28.7%. As seen in both the curves, the correction in Kt can shift the curves downward to fit the manufacturer given curves. Yet, although the constant-torque and high-speed regions show high similarities to the manufacturer given curve in Fig. 7.22, the optimized decreasing-torque region has a much higher error. Similar to motor ST5909M2008-A, when Kt are not set to the preset value proposed, a higher error in the constant-torque and decreasing-torque regions can be an indication of an inaccurate datasheet inductance used.

7.5 Results and discussions

From the two methods to obtain the non-linear parameters with and without motor measurements, the method with direct optimization without measured parameter values shows 9.7% and 13.7% decrease in overall average error. Such a number is higher than 6.9% and 5.3% of the method with measured parameters. However, with the validation from the semi-analytical model with a mechanical block, the method with direct optimization shows a less convincing curve at the high-speed region. The motor is not able to work in those regions. Oppositely, although the accuracy has a smaller increase, the method with measured parameters shows a more convincing outcome throughout the motor functional speeds. Such demonstrates the importance of physical measurements to not only verify datasheet parameters but also obtain the non-linear parameters. Nonetheless, if optimization is applied, the ranges have to be set to reasonable numbers based on datasheet parameters.

With three different motors being tested with the semi-analytical model, several limitations can be seen. First, since the back-emf is measured for the voltage constant, it is an important parameter that is essential to calculate ψ. Although the torque constant can be easily calculated and substitute for the voltage constant, it however only works in ideal condition, which is not true in the motor simulation. Such inaccurate voltage constant can be seen in motors ST4118M1206-A and MS17HD2P415048. Second, since the TI-curve is based on the torque constant, it is best to measure the single-phase torque constant than simply dividing the two-phase torque constant, calculated by holding torque, by $\sqrt{2}$. Third, the manufacturer may obtain the pull-out torque differently causing slight high-speed and low-speed differences. Such differences cannot be estimated by the semi-analytical model. Forth, the difference between the manufacturer given curve and generalized electrical model curves can be caused by the high tolerances in the motor inductance and resistance parameters. Such inductance and resistance are therefore important to be verified initially.

Chapter 8

Conclusions and future work

The research aims to extend the generalized motor equations into a semi-analytical model by including non-linear entities of the motor electromagnetic phenomenons. This is done with an approach to first identify the motor dynamics via FEA and motor analytical equations, then apply several estimated sinusoidal and second-order non-linear entities on top of the generalized electrical equations.

The NEMA 17 motor, model ST4209L1704, is constructed into a 3D FEA model with the physically measured dimensions and geometry. Step dynamics of the numerically solved FEA model are translated into lookup tables. The simulated motor dynamics are obtained with an analytical modeling method coupled with lookup tables and analytical equations. Based on the quantitative and qualitative analysis of the motor torque-speed dynamics simulated from the generalized electrical and flux-based models, two methods to obtain the non-linear parameters with and without physical motor measurements are tested.

- The non-linear parameters without motor measurements are optimized to best fit the motor curves. Although this method can achieve good fits of 7.7% average error compare to the 21.4% error at 48V from the generalized electrical model, it however can be optimized to incorrect parameters when the range is not limited. Such can highly reduce the significance of the semi-analytical model.

- The non-linear parameters with motor measurements are estimated within the physical measured parameter values. The semi-analytical model with such non-linear parameters can better fit the curve with 25.7% error instead of 31.0% at 48V from the generalized electrical model with measured inductance and resistance. However, the increase in accuracy is limited when its compared to the generalized electrical model. This is because of the relatively small values of non-linear parameters.

With comparisons of the two methods, the semi-analytical model will work best when datasheet parameter is verified and some non-linear parameters are measured. Without the measured non-linear parameters, the generalized electrical model may be the best with less uncertainty. However, in both models, the datasheet parameters are needed to be verified. Additional motor parameters from different manufacturers are then applied afterwards to obtain their relative semi-analytical model dynamic accuracy. The limit of the semi-analytical model is shown more clearly with such tests. Additional to the high tolerances of these datasheet parameters, several motor constants such as back-emf are simply not given. Since they had to be estimated, the simulated model can be imprecise.

It is possible to include the non-linear entities of mutual inductance, position-dependent inductance, detent torque harmonics, and non-linear torque constant into the semi-analytical model proposed. However, such a model provides limited improvements over the generalized electrical model. For these improvements, datasheet parameters have to be verified and non-linear parameters have to be obtained. Additionally, the proposed semi-analytical model holds several limitations that made it less robust than the generalized electrical model. Firstly, the model accuracy is highly affected by the non-linear parameters. Secondly, since the semi-analytical model proposed does not include new mechanical non-linearities compare to the generalized electrical model, it does not provide extra accuracy in simulating the motor mechanical oscillation. Thirdly, to optimize the non-linear parameters realistically, a well-defined range is required. Lastly, without the physical measurements, it is also important to obtain the correct datasheet versions for the given motor.

Some future works are proposed to further improve the semi-analytical model. A higher order non-linear

torque constant function can be further investigated to better fit torque saturation. The physical test bench measurements proposed in this thesis should be implemented to further validate the semi-analytical model. Likewise, since the mechanical parameters in the thesis are applied based on conventions and motor coupling practices, to obtain a more realistic motor oscillation dynamics, the test bench measurement is needed for more accurate parameters. Other dynamics, such as step response, can also be further validated with the test bench. The semi-analytical model could also be further improved by an optimization algorithm that can obtain the non-linear parameters under constraints based on the physical motor measurements and manufacturer given dynamics.

Bibliography

[1] K. L. Conrad, P. S. Shiakolas, and T. Yih, "Robotic calibration issues: Accuracy, repeatability and calibration," in *Proceedings of the 8th Mediterranean Conference on Control and Automation (MED2000), Rio, Patras, Greece*, vol. 1719, 2000.

[2] D. Deaconu, A. Chirila, V. Navrapescu, M. Albu, C. Ghita, and C. Popescu, "Two hybrid stepper motor models," in *Proceedings of the 9th WSEAS International Conference on International Conference on Automation and Information*, ser. ICAI'08. Stevens Point, Wisconsin, USA: World Scientific and Engineering Academy and Society (WSEAS), 2008, p. 129–134.

[3] D. Collins, "Servo motor: What type of motor is it? ac or dc, brushed or brushless...." Feb 2019. [Online]. Available: https://www.linearmotiontips.com/what-type-of-motor-is-a-servo-motor/

[4] "Advantages and disadvantages of dc servo motors, ac servo motors and stepper motors." [Online]. Available: http://www.tw-motor.com/info/advantages-and-disadvantages-of-dc-servo-motor-31122893.html

[5] B. Henke, O. Sawodny, S. Schmidt, and R. Neumann, "Modeling of hybrid stepper motors for closed loop operation," *IFAC Proceedings Volumes*, vol. 46, no. 5, pp. 177–183, 2013.

[6] L. Zhang, L. Liu, J. Shen, J. Lai, K. Wu, Z. Zhang, and J. Liu, "Research on stepper motor motion control based on mcu," in *2017 Chinese Automation Congress (CAC)*, 2017, pp. 3122–3125.

[7] P. P. Acarnley, *Stepping motors: a guide to theory and practice*. The Institution of Engineering and Technology, 2007.

[8] T. Kenjo and A. Sugawara, *Stepping motors and their microprocessor controls*. Clarendon Press, 2003.

[9] R. Vierbergen, "Predicting and improving the behaviour of stepping motors," in *TU/e technische universiteit Master's Thesis*, 2005.

[10] Hoang Le-Huy, P. Brunelle, and G. Sybille, "Design and implementation of a versatile stepper motor model for simulink's simpowersystems," in *2008 IEEE International Symposium on Industrial Electronics*, 2008, pp. 437–442.

[11] Y. Oner, I. Senol, N. Bekiroglu, and E. Aycicek, "Magnetic equivalent circuit model of surface type fractional-slot permanent magnet synchronous generator," *Journal of Vibroengineering*, vol. 15, no. 1, pp. 223–232, 2013.

[12] Chang-Sung Jin, Youn-Hyun Kim, Ju Lee, Tae-Bin Im, and Yun-Hyun Cho, "Nonlinear analysis of 2 phase hybrid stepping motor using 3d equivalent magnetic circuit network method," in *2002 IEEE International Magnetics Conference (INTERMAG)*, 2002, pp. FT10–.

[13] B. Nedjar, S. Hlioui, L. Vido, Y. Amara, and M. Gabsi, "Flux focusing permanent magnet synchronous machine modeling by 2d magnetic equivalent circuit," in *2012 15th International Power Electronics and Motion Control Conference (EPE/PEMC)*, 2012, pp. LS3a–1.3–1–LS3a–1.3–6.

[14] S. Hlioui, B. Nedjar, L. Vido, Y. Amara, and M. Gabsi, "2d–3d magnetic equivalent circuit of the flux focusing permanent magnets synchronous machine," in *2014 International Conference on Electrical Sciences and Technologies in Maghreb (CISTEM)*, 2014, pp. 1–7.

[15] Z. Ferkova, "Comparison between 2d and 3d modelling of induction machine using finite element method," *Advances in Electrical and Electronic Engineering*, vol. 13, no. 2, 2015.

[16] L. Chang, A. R. Eastham, and G. E. Dawson, "Permanent magnet synchronous motor: finite element torque calculations," in *Conference Record of the IEEE Industry Applications Society Annual Meeting,*, 1989, pp. 69–73 vol.1.

[17] R. Kieburtz, "The step motor–the next advance in control systems," *IEEE Transactions on Automatic Control*, vol. 9, no. 1, pp. 98–104, 1964.

[18] E. A. Snowdon and W. E. Madsen, "Characteristics of a synchronous inductor motor," *Transactions of the American Institute of Electrical Engineers, Part II: Applications and Industry*, vol. 81, no. 1, pp. 1–5, 1962.

[19] A. Goldman, *Modern ferrite technology.* Springer Science & Business Media, 2006.

[20] A. Hughes and B. Drury, *Electric motors and drives: fundamentals, types and applications.* Newnes, 2019.

[21] V. Athani, *Stepper motors: fundamentals, applications and design.* New Age International, 1997.

[22] "Stepper motor types and working," May 2018. [Online]. Available: https://electricalacademia.com/synchronous-machines/stepper-motor-types-working/

[23] C. W. De Silva, "Design equations for the tooth distribution of stepping motors," *IEEE Transactions on Industrial Electronics*, vol. 37, no. 2, pp. 184–186, April 1990.

[24] H. Mozetic, U. Boff, W. Luna, M. Pfingstag, R. Martins, M. Dias, and L. Schaeffer, "Development of cores for mini motors from laminated sheets of electric steel abnt (brazilian association of technical standards) 35f 420m with thermal treatment," *Journal of Electrical Systems*, vol. 12, pp. 357–372, 06 2016.

[25] M. Laughton and D. Warne, "Electrical engineer's reference book, newnes, 2003."

[26] S. Banerjee and J. Mellema, "A new method for the determination of paleointensity from the a.r.m. properties of rocks," *Earth and Planetary Science Letters*, vol. 23, no. 2, p. 177–184, 1974.

[27] Ki-Bong Jang, Seong-Yeop Lim, Tae-Bin Lim, Chang-Sung Jin, Yun-Hyeon Cho, Young-Tae Kim, and Ju Lee, "2-d fe analysis of hybrid stepping motor using virtual magnetic barrier," *IEEE Transactions on Magnetics*, vol. 39, no. 5, pp. 3268–3270, Sep. 2003.

[28] K. Rajagopal and B. Singh, "Detent torque from the soft magnetic stator stack of a hybrid stepper motor," *Journal of Applied Physics - J APPL PHYS*, vol. 93, pp. 8784–8786, 05 2003.

[29] P. Bober and Z. Ferková, "Dynamic analysis of permanent magnet stepper motor with asymetric stator," in *2015 International Conference on Electrical Drives and Power Electronics (EDPE)*, 2015, pp. 324–327.

[30] P. Zaskalicky and M. Zaskalicka, "Analytical method of calculation of the current and torque of a reluctance stepper motor using fourier complex series," in *2008 13th International Power Electronics and Motion Control Conference*, 2008, pp. 899–902.

[31] J. Jansson and C. Rådahl, "Torque estimation algorithms for stepper motor," Master's thesis, Chalmers University of Technology, 2018.

[32] R. Antonello, A. Cenedese, and R. Oboe, "Torque ripple minimization in hybrid stepper motors using acceleration measurements," *IFAC Proceedings Volumes*, vol. 44, no. 1, pp. 10 349–10 354, 2011.

[33] M. Butcher, A. Masi, R. Picatoste, and A. Giustiniani, "Hybrid stepper motor electrical model extensions for use in intelligent drives," *IEEE Transactions on Industrial Electronics*, vol. 61, no. 2, pp. 917–929, 2013.

[34] Y.-K. Lin, Y.-N. Hu, T.-K. Lin, H.-N. Lin, Y.-H. Chang, C.-Y. Chen, S.-J. Wang, and T.-F. Ying, "A method to reduce the cogging torque of spindle motors," *Journal of magnetism and magnetic materials*, vol. 209, no. 1-3, pp. 180–182, 2000.

[35] N. Johantgen, "Speed - torque curves for stepper motors," 2018. [Online]. Available: https://www.orientalmotor.com/stepper-motors/technology/speed-torque-curves-for-stepper-motors.html

[36] J. Dong, B. Howey, B. Danen, J. Lin, J. W. Jiang, B. Bilgin, and A. Emadi, "Advanced dynamic modeling of three-phase mutually coupled switched reluctance machine," *IEEE Transactions on Energy Conversion*, vol. 33, no. 1, pp. 146–154, 2018.

[37] MATLAB, *ee_motor_stepper_pullin_characteristics function (R2019a)*. Natick, Massachusetts: The MathWorks Inc., 2010.

[38] D. Collins, "Detent torque and holding torque: What's the difference?" 2016. [Online]. Available: https://www.motioncontroltips.com/faq-whats-the-difference-between-detent-torque-and-holding-torque/

[39] E. S. Rao and P. Prasad, "Dynamic performance analysis of permanent magnet hybrid stepper motor by transfer function model for different design topologies," *International Journal of Electrical and Computer Engineering*, vol. 2, no. 2, p. 191, 2012.

[40] P. Bogusz, M. Korkosz, and J. Prokop, "Control method of high-speed switched reluctance motor with an asymmetric rotor magnetic circuit," *Archives of Electrical Engineering*, vol. 65, no. 4, 2016.

[41] J. S. (https://electronics.stackexchange.com/users/330/jason s), "Understanding motor constants kt and kemf for comparing brushless dc motors," Stackexchange, uRL:https://electronics.stackexchange.com/questions/33315/understanding-motor-constants-kt-and-kemf-for-comparing-brushless-dc-motors (version: 2015-11-11). [Online]. Available: https://electronics.stackexchange.com/questions/33315/understanding-motor-constants-kt-and-kemf-for-comparing-brushless-dc-motors